Università degli Studi di Palermo
Dipartimento di Ingegneria
Doctoral in Advances In Modeling, Health-monitoring, Infrastructures, Geomatics, Geotechnics, Hazards, Engineering Structures, Transportation
(AIM HIGHEST)

NOVEL MATERIALS AND TECHNOLOGIES FOR THE DESIGN AND DEVELOPMENT OF 3D SCAFFOLDS FOR BONE REGENERATION

ICAR/08

THESIS OF
ENG. FABIANA AMIRI

COORDINATOR
PROF. GIUSEPPE CAMPIONE

TUTORS
PROF. MASSIMILIANO ZINGALES
PROF. LORENZO MORONI
ENG. MATTEO MANTOVANI

XXXVI CYCLE - ACADEMIC YEAR 2023/2024

Novel Materials and Technologies for the Design and Development of 3D scaffolds for Bone Regeneration

ENG. FABIANA AMIRI

July 2024

For myself,
my beloved family,
my wonderful friends and
for my darling grandpa Gaspare

Dissemination of Results

This Doctoral Thesis is formed by 1 scientific article published in international journals, and 1 under revision for patent before publication.

- Amiri F., Bologna E., Nuzzo G., Moroni L., Zingales M. *Fractional-order poromechanics for a fully saturated biological tissue: Biomechanics of the meniscus.* International Journal for Numerical Methods in Biomedical Engineering, **2023**
- Nuzzo G., Amiri F., Russotto S., Bologna E., Zingales M. *A fractional-order theory of phase transformation in anomalous heat transfer.* Materials Research Proceedings, **2023**, 26, pp. 77–82
- Amiri F., Fucile P., Nuzzo G., Zingales M., Moroni L.*Encapsulation phenomena of PLA-PCL blending.* ACS Applied Materials & Interfaces, **under submission**

National and International Conferences

- Amiri F., Nuzzo G., Zingales M., *Diffusion problem in a meniscus with fractional calculus.* 7th International Conference on Computational & Mathematical Biomedical Engineering, **2022**.
- Amiri F., Nuzzo G., Bologna E., Zingales M., *A novel approach to poromechanics for fractional hereditary materials.* XXV Congresso Nazionale AIMETA, **2022**.
- Amiri F., Fucile P., Nuzzo G., Zingales M., Moroni L., *Influencing parameters of additive manufacturing on the viscous encapsulation phenomena of PLA-PCL blending.* International Conferences of Engineering Mechanics Institute, **2023**.
- Amiri F., Bologna E., Nuzzo G., Moroni L., Zingales. *Cyclic stress effect on the fractional poroviscoelastic model.* International Conferences of Engineering Mechanics Institute, **2023**.
- Amiri F., Fucile P., Nuzzo G., Zingales M., Moroni L., *Encapsulation phenomena of PLA-PCL blending.* 33rd Annual Conference of the European Society for Biomaterials, **2023**.

Dissertation Outline

The main objective of this Doctoral Thesis is to design and implement a scaffold for bone tissue regeneration. This topic is of great relevance to the field of tissue engineering and has significant implications for regenerative medicine. By studying scaffolds for bone regeneration, it is possible to achieve a deeper understanding of how to exploit the principles of tissue engineering and regenerative medicine to improve human health and well-being.

This Doctoral Thesis is structured in three main sections: Introduction, Chapters, and Appendix. The Introduction section provides a general overview of the topic, defining key terms and presenting key issues, reviewing the existing literature on the topic, highlighting the main theories and research that have contributed to our current understanding; the general and specific objectives of the thesis are also reported. The Chapters section is organized into four main chapters, presenting the mechanical behavior of biological tissue as a linear hereditariness material, but also the poroelasticity of a bi-phasic material in the second and third chapters respectively. The fourth chapter presents the research methodology used for this thesis, explaining in detail what tests were conducted, how data were collected and analyzed, and what results were obtained. A general discussion of the most relevant results obtained and the most important conclusions are included in the final section of each chapter, as well as the reference bibliography. Meanwhile, Chapter Five summarizes the main findings of the research and suggests possible directions for future research. Finally, an Appendix concerning the general concept of Fractional Calculus is also reported.

Contents

Acronyms and Symbols

β-TCP	β-Tricalcium Phosphate
1D	One-dimensional
2-Bu	Two-butoxy ethanol
2D	Two-dimensional
2PP	Two-Photon Polymerization
3D	Three-dimensional
AM	Additive Manufacturing
BCP	Bi-phasic Calcium Phosphate
b-FGFs	Basic fibroblast growth factors
BMP-2	Bone Morphogenetic Protein-2
BMPs	Bone Morphogenetic Proteins
BD	Boundary Conditions
Ca	Calcium
CA	Citric Acid
CAD	Computer-Aided Design
Cl	Chlorine
COLI	Collagen type I
CS	Calcium Sulfate
CPC	Calcium Phosphate Cement
CRU	Constitutional Repeating Unit
CSD	Critical-sized Defect
DEX	Dexamethasone
DLP	Digital Light Projection
DSC	Differential Scanning Calorimetry
DW	Direct Writing
ECM	Extracellular Matrix
EDS	Energy Dispersive X-ray Spectroscopy
ESP	Solution Electrospinning
EtOH	Ethanol
FDM	Fused Deposition Modeling
FE	Finite Element
FEM	Finite Element Method
FOH	Fractional-Order Hereditariness
FGF	Fused Granulate Fabrication
FGPs	Functionally Graded Porous structures
FHM	Fractional Hereditary Materials
FPF	Fused Pellet Fabrication
FTIR	Fourier transform infrared spectroscopy
GAG	Glycosaminoglycan
HA	Hyaluronic Acid
hADS	Human adipose-derived stem cell
Hap	Hydroxyapatite
HB	Hyperelastic Bone
Hh	Hedgehog
HUVECs	Human Umbilical Vein Endothelial cells
HUVSMCs	Human Umbilical Vein Smooth Muscle cells
IC	Initial Conditions
IGFs	Insulin-derived growth factors
K	Potassium
LV	Lentiviral
LVT	Laguerre-Voronoi tessellation
MA	Methacrylic Anhydride
Mg	Magnesium
MSCs	Mesenchymal Stem Cells
Na	Sodium
OCT	Optimal Cutting Temperature
ODE	Homogeneous Differential Equation
OPCs	Osteoblast precursor cell
P	Phosphorus
PBS	Phosphate-buffered Saline
PCL	Poly-ϵ-caprolactone
PDE	Partial Differential Equation
PDGF	Platelet-derived growth factor
PDLA	Poly(D, L-lactic acid)
PDLGA	Poly(D, L-lactic-co-glycolic acid)
PEG	Poly(ethylene glycol)
PEGDA	Poly(ethylene glycol diacrylate)
PGA	Poly(glycolic acid)
PLA	Poly(L-lactide)
PLCL	Poly(L-lactide–co-caprolactone)
PLGA	Poly(L-lactide-glycolic acid)
PLLA	Poly(L-lactic acid)
PLM	Polarized Light Microscopy
rhBMP-2	Recombinant human Bone Morphogenetic Protein-2
RVE	Representative Volume Elements
SBF	Simulated Body Fluid
SC	Starch-Citric Acid
SCPL	Solvent Casting and Particulate Leaching
SEM	Scanning Electron Microscopy
SF	Silk fibroin
SGC	Starch-Glycerol-Citric Acid
SLA	Stereolithography
SLS	Selective Laser Sintering
SMC	Smooth Muscle Cells
TE	Tissue Engineering
TEM	Transmission Electron Microscopy
TGA	Thermogravimetric Analysis
THF	Tetrahydrofuran
Ti	Titanium
TPMS	Triply Periodic Minimal Surfaces
UV	Ultraviolet
VD3	Vitamin D3
XRD	X-Ray Diffraction

Chapter. 1

Introduction

Bone tissue, also called *osseous tissue*, is a mineralized and viscous-elastic connective tissue, which exerts crucial functions in our body such as support, and protection of other tissues and mineral storage. It consists of a flexible matrix (about 30%) and bound minerals (about 70%) which are intricately and endlessly reshaped by a group of specialized bone cells. Particularly, *osteoblasts* and *osteocytes* are cells involved in the formation and mineralization of bone, while *osteoclasts* are involved in the resorption of bone tissue. Modified osteoblasts, i.e. flat-shaped osteoblasts, on the other hand, become bone lining cells that form a protective layer covering bone surfaces, too. Their unique composition and design allow bones to be relatively hard and strong while remaining lightweight. Bone tissue is mineralized tissue of two types, *cortical bone* and *cancellous bone*. Other types of tissue found in bones include bone marrow, endosteum, periosteum, nerves, blood vessels, and cartilage[1]. The mineralized matrix or Extracellular Matrix (ECM) of bone tissue is composed of inorganic salts and organic matrix. The organic matrix consists of 90 to 95% of elastic collagen fibers (predominantly type I collagen), and noncollagenous proteins including osteocalcin, osteonectin, osteopontin, fibronectin, and bone sialoprotein II, Bone Morphogenetic Proteins (BMPs), also known as *ossein*, and the remainder is ground factors. The elasticity of collagen improves fracture resistance. Meanwhile, the matrix is hardened by the binding of the inorganic mineral salt, calcium phosphate, into a chemical arrangement known as bone mineral, a form of calcium apatite. The inorganic material in bone consists mainly of phosphate and calcium ions, but significant amounts of bicarbonate, sodium, potassium, citrate, magnesium, carbonate, fluorite, zinc, barium, and strontium are also present [2]. In addition, the bone matrix can release various molecules that interfere with bone cell activity and, consequently, participate in bone remodeling. The bone matrix thus consists of a complex and organized structure that provides mechanical support and exerts an essential role in bone homeostasis. *Bone homeostasis* refers to the balance between bone formation and bone resorption, which is crucial for maintaining the integrity of the skeletal system. This process involves a precise spatiotemporal sequence in which packets of old bone are removed and replaced with new bone. In physiological and healthy conditions, osseous tissues usually have the potential to regenerate to a state that is biologically and biomechanically indistinguishable from the original one. However, when there are particular diseases or pathological conditions (like diseases, developmental deformities, revision surgery, and tumor resection or osteomyelitis) or the fracture is greater than the critical-sized defect (CSD), it is unlikely to regenerate[3]. Anyway, before going on, it is necessary to define and distinguish the term repair from regeneration because *repair* is the restoration of the continuity of tissues at the injury site, but not necessarily by the same cells and tissues that existed before the injury; while *regeneration* is a series of biologically and biomechanically inspired events that produce restoration of form and function of the injured tissues to a state that is biologically and functionally indistinguishable from the pre-injury wound site.

Bone regeneration is a complex, well-orchestrated physiological process of bone formation, which can be seen during normal fracture healing and is involved in continuous remodeling throughout adult life. This process is part of the repair response to injury, as well as during skeletal development. The process of bone regeneration involves many cell types and intracellular and extracellular molecular-signaling pathways, with a definable temporal and spatial sequence. The most common form of bone regeneration in the clinical setting is fracture healing, during which the pathway of normal fetal skeletogenesis, including intramembranous and endochondral ossification, is recapitulated. However, there are complex clinical conditions in which bone regeneration is required in large quantity, such as for skeletal reconstruction of large bone defects created by trauma, infection, tumor resection, and skeletal abnormalities, or cases in which the regenerative process is compromised, including avascular necrosis, atrophic non-unions, and osteoporosis.

To augment the impaired or 'insufficient' bone-regeneration process, different strategies are used. A key component of many of these strategies is the use of a structure that provides a three-dimensional structure for the growth of new bone tissue, including the 'gold standard' autologous bone graft, free fibula vascularized graft, and allograft implantation. Bone regeneration scaffolds are designed to mimic the natural environment of bone tissue, providing the necessary mechanical support and promoting the proliferation and differentiation of bone cells. They are often made of biocompatible and biodegradable materials, such as natural or synthetic polymers, ceramics, or bioactive compounds. Furthermore, these scaffolds can be combined with other tissue engineering techniques, such as the use of stem cells or growth factors, to promote bone regeneration. They can also be designed to deliver drugs or other bioactive molecules to stimulate healing and regeneration.

The goal of this thesis is the design and development of an innovative scaffold for bone regeneration. Firstly, the basic principles of scaffold design, as well as techniques, materials, and contemporary approaches used for bone regeneration, discuss recent advances and examine future challenges and opportunities will be explored in *Chapter 1*. Anyway, the realization and development of scaffolds for biological tissues need to be preceded by a theoretical study of mathematical models used in the literature to describe the mechanical behavior of biological tissues. These models will be presented and described in detail into *Chapter 2*. The key directional concepts that need to be recognized for the rational design and development of regenerative therapy are also presented. These concepts will include biomechanical characteristics for supporting and sustaining function, regenerative therapies for bone, and the importance of a three-dimensional (3D) porous environmental matrix in which cells must attach and proliferate. Rigorous benefit criteria with objective data will be offered to provide a framework for the rational design and deployment of a comprehensive instrument kit for bone regenerative therapy. Whereas in *Chapter 3*, the development of a new mathematical model including the use of fractional

calculus, as well as numerical simulations on Wolfram Mathematica will be reported, too.
Chapter 4 will explain and further discuss the process of scaffold design and implementation as well as materials, methods, designs, and characterization tests adopted. Finally, *Chapter 5* offers a general conclusion, summarizing the main findings of the research and suggesting possible directions for future research. This thesis hopes to contribute to the existing literature for modeling and fabrication of scaffolds for bone tissue regeneration, providing new insights that can guide further studies in this field.

1.1 Problem description

Osteotomy, or "bone cutting”, is a surgical procedure that involves cutting and reshaping bones. This technique is often used to correct bone and joint defects, such as those caused by trauma or degenerative diseases such as arthritis. It can also be used to lengthen or shorten bones in cases of limb length discrepancy. Although an invasive procedure, osteotomy can offer a significant improvement in function and pain for patients with certain orthopedic conditions. In addition, it can delay the need for more invasive surgeries, such as total joint replacement. However, osteotomy does not restore the full functionality of the bone, and as with any surgical procedure, it also carries several risks, such as blood clots, infections, bleeding, joint stiffness, nerve damage, scar tissue, etc. It also has a high rate of long-term complications like severe articular destruction, under-correction, overcorrection, noticeably decreased range of motion, joint instability, and bone healing problems[4].
In open wedge osteotomy, the most reliable fixation and augmentation techniques are still controversial, but gold standards seem to be locked plates and autologous bone grafts. In general, a *graft* is a piece of healthy skin or bone, or a healthy organ, that is attached to a damaged part of your body by a medical operation to replace it. Consequently, bone grafts are used to replace or stimulate new bone formation in cases such as healing of skeletal fractures, for bone loss due to trauma, infection, or disease, or to improve bone healing response and regeneration around surgically implanted devices. There are three types of bone grafts: autografts, allografts, and bone graft substitutes.
Bone *autografts* are taken from a donor site in a patient and subsequently implanted in the same patient, mitigating the risk of immunological sequelae. In clinical practice, the gold standard is an iliac bone graft[5]. This procedure involves the collection of an iliac bone flap with arteries and veins from the patient, then this is appropriately treated and adjusted to the size of the defect during surgery. The autograft is intrinsically vascularized and may be co-harvested with a vascular pedicle. So, it provides an ideal combination of biological signals for the integration of the new bone to the recipient site. However, there are drawbacks associated with the use of autografts: they are limited in quantity, shape restrictions often require extensive intra-operative modifications, and double surgery operation on the same patient. As with any surgery, surgical complications may include chronic pain, inflammation, scarring, blood loss, infection, and donor site morbidity[6]. On the other hand, bone *allograft* is taken from a cadaver or living donor and then treated and im-

planted in the patient. The advantages of allografts include the issue of donor site morbidity and limited availability problems. However, allogeneic bone is not necessarily immune-preventive and involves the risk of infectious agents. Furthermore, during tissue bank processing, allografts are subjected to a series of techniques that reduce the risk of disease transmission and immunological responses but also reduce the osteogenic potential of the graft[7]. Alternatives to autografts and allografts are *xenografts*: bone from non-human species. Although xenografts are treated to ensure sterility and biocompatibility, the risks of disease transmission (even if minimal) and ethical issues have limited their clinical attractiveness and therefore have not been used.

Among these, autografts and allografts are two of the common treatments for large bone injuries. However, their limitations have prompted the search for other alternatives, referred to as *bone graft substitutes*. These grafts create a platform for the cells to migrate to the site of action and form new tissue [8].In detail, the field of biomedical engineering which use the combination of cells, engineering, material methods and appropriate biochemical and physical-chemical factors to repair, maintain, enhance, or replace different types of biological tissue, is referred to as *Tissue Engineering* (TE), as a branch of *Regenerative Medicine* (RM). Meanwhile, the external and/or artificial supports are usually called *scaffolds*.

The scaffolds' tissue regeneration capacity is measured in terms of their biocompatibility, biodegradability, bioresorbability, porosity, mechanical properties, similarity to original tissue, safety, and ease of use[6, 8]. Additionally, the biocompatibility of degradation products is of further importance, as materials such as metals, ceramics, and polymers can degrade in the body. It is therefore essential that therapeutic bone grafts degrade in such a way that bone regeneration activities are not obstructed. It means that if a bone graft material degrades rapidly, i.e. before bone infiltration begins (about four weeks after the injury), it will not be able to provide the necessary support. Conversely, if the material remains at the site for too long (more than four weeks), it may slow down regeneration. A sufficiently high degradation rate after tissue regeneration will be preferred in TE because foreign materials carry a risk of inflammation [9].

In terms of bone regeneration, it's necessary to consider the osteogenic, osteoconductive, and osteoinductive potential, too. *Osteogenesis* is the process by which osteoblasts at the defect site express osteoid that subsequently mineralizes, yielding new bone. Therefore, the osteogenic potential of a bone graft is given by cells involved in bone formation, such as mesenchymal stem cells (MSCs), osteoblasts, and osteocytes. The term *osteoconductive* refers to the scaffold or matrix that stimulates bone cells to grow on its surface [10]. Meanwhile, the *osteoinductive* capacity of a bone graft is perhaps the most important property in bone healing as it refers to the stimulation of MSCs to differentiate into preosteoclasts to begin the bone-forming process[11]. An ideal bone graft is characterized by all these phenomena and clinically will promote regeneration of bone that is physiologically and functionally indistinguishable from the pre-injury defect site, providing an interconnected system through which new cells migrate and blood vessels are formed (i.e. *angiogenesis*), too [12].

The challenge for regenerative medicine is to deconstruct the regenerative process of fracture healing and then stitch together those components to produce osteo-regenerative therapies for applications in bone defects that exceed the CSD. There are many approaches to bone tissue regeneration but, due to the enormous complexity, it is not possible to assume a single approach that fits all clinical needs or provides solutions in all circumstances. In particular, contemporary efforts to promote bone regeneration focus on cells, biological factors, materials, and structure. Cells and biological factors will not be discussed in this research. Nevertheless, in this chapter a general overview of materials used (*Section 1.2*), as well as techniques and methods (*Section 1.3*) implemented for scaffolds realization in bone regeneration research have been reported.

1.2 Materials

Designing bone biomimetic scaffolds involves building a proper representation of bone, that can be seen as an open-cell composite material composed of osteogenic cells, ECM, proteins, growth factors, mineral calcium in the form of calcium hydroxyapatite, and a complex vascular system. An ideal bone graft or scaffold should be made of biomaterials that imitate the structure and properties of natural bone ECM, include osteoprogenitor cells, and create living tissue constructs that are structurally, functionally, and mechanically comparable to the natural bone. Therefore, the physical and chemical composition of scaffolds is critical for cell viability and proliferation.

The most common types of materials for artificial bone grafts are bioceramics, polymers, metals, hydrogel, and composite materials, further discussed in the following paragraphs.

1.2.1 Metals

Metals are a class of substances characterized by high electrical and thermal conductivity, malleability, ductility, and high reflectivity of light. They are usually solid, shiny, and have good conductivity in terms of electrical and thermal. Clinically widely used metallic materials include Magnesium (*Mg*)-alloys, Stainless Steel, Titanium (*Ti*), Ti-alloys, and Cobalt-Chrome alloys. Metallic materials can sustain high mechanical loads, so they are generally used as implants for subchondral bone, i.e. permanent implants. However, stainless steel, cobalt-chrome, Ti, and its alloys are not degradable and wear particles can therefore form. In addition, traditional metal fixation devices often cause osteopenia and weaken surrounding healthy tissue because the elastic modulus of metals is much higher than the surrounding tissue so the main load forces are mainly supported by the metals. Therefore, metals are suitable for application in load-bearing bone defects, but they present a high risk of stress shielding, too.

1.2.2 Polymers

Polymers are macromolecules,i.e. molecules with a high molecular weight, consisting of a large number of the same or different molecular groups joined "in a chain" by

repetition of the same type of bond. According to the international IUPAC definition, the structural unit is referred to as a "*constitutional repeating unit*" (CRU). According to their origin, polymers can be classified into natural, synthetic and man-made polymers.
Natural-derived polymer are well-known candidates for tissue-engineered bone, owing to the merits of cytocompatibility, biocompatibility, nonantigenicity, biofunctionality, and biodegradability. They include gelatin, glycosaminoglycan, collagen type I (COLI), chitosan, alginate, hyaluronic acid (HA), starch, and bacterial-sourced polymers (i.e. hydroxyalkanoates)[14]. HA and collagen are the main components of natural bone. Thus, an ideal scaffold for bone tissue engineering should incorporate the same biological characteristics of these components to promote bone formation. Unfortunately, their mechanical properties are generally weak and insufficient. Compared with natural polymers, the mechanical properties (e.g. stiffness and strength) and degradation speed of *synthetic polymers* have been flexibly regulated. Commonly used biodegradable synthetic polymers include polycaprolactone (PCL), poly(lactic acid) (PLA), poly(glycolic acid) (PGA)[15], poly(ethylene glycol) (PEG), and their variants and copolymers such as poly(L-lactic acid) (PLLA), poly(L-lactide-glycolic acid) (PLGA)[16, 17], poly(D, L-lactic-co-glycolic acid) (PDLGA), Poly(L-lactide–co-caprolactone)(PLCL)[18, 19] and poly(ethylene glycol diacrylate) (PEGDA). Generally, synthetic polymers still possess disadvantages of bioactivity, since they usually possess a hydrophobic surface which can affect cell adhesion and proliferation. Besides, by incorporating growth factors or bioactive materials into polymer matrices, these polymers exhibit bioactive hybrid composites that can greatly enhance biocompatibility, mechanical strength, and hydrophilicity, and also show a certain role in supporting cell proliferation and differentiation, thus augmenting the repair and regeneration process. Generally, growth factors include insulin-derived growth factors (IGFs), BMPs[21], platelet-derived growth factor (PDGF), basic fibroblast growth factors (b-FGFs), hedgehogs (Hh)[22], and transforming growth factors (TGFs). Bioactive factors include a series of factors i.e.: mineral ions such as Mg^{2+}, biological growth factors, intracellular signaling molecules such as receptors, kinases, and transcription factors, and signaling mimetics derived from synthetic or natural compounds.

1.2.3 Ceramics

Ceramics are a class of materials that are characterized by their hardness, brittleness, heat resistance, and corrosion resistance. They are made by shaping and then firing an inorganic, nonmetallic material, such as clay, at a high temperature. Common examples of ceramics include earthenware, porcelain, and brick. Ceramics are produced from either synthetic or deeply transformed natural raw materials. They have a wide range of applications, from domestic and industrial products to advanced ceramic engineering, such as semiconductors. In detail, ceramics that are specifically developed for use in medical and dental applications are called *Bioceramics*. Bioceramics are used in a wide range of clinical applications, including orthopedics, otolaryngology, maxillo-facial and plastic surgery, oral surgery, periodontology, and tumor therapy. They are chosen for these applications due to their excellent biocompatibility, ability to stimulate tissue regeneration, and their mechanical properties. In the world of bone tissue regeneration, bioceramics play a key role due to their chemical mimicking of the bone's inorganic component, helping in the restoration and reconstruction of injured parts of the musculoskeletal system. Generally, they have been used in RM in the form of:

- *Solid* (non-porous) scaffolds used for reconstruction of ear ossicles (hammer, anvil and stirrup);
- *Powders* used as bone fillers;
- *Porous scaffolds* allowing regeneration of larger bones.

Based on their activity, bioceramics can be subdivided into:

- *Inert bioceramics*: such as Alumina and Zirconia, are often used in surgical implants due to their excellent mechanical properties;
- *Bioactive Glasses*: can bond to bone and stimulate the body's natural healing processes;
- *Glass-Ceramics*: have both glassy and crystalline phases, which can provide a combination of properties not achievable in purely glass or ceramic materials;
- *Coatings* and *Composites*: are used to enhance the performance of other materials, for example by improving their biocompatibility or mechanical properties;
- *Hydroxyapatite* (HAp) and *Resorbable Calcium Phosphates* (Ca-P): can be resorbed by the body over time, and are often used in applications where temporary support is needed during healing;
- *Radiotherapy Glasses*: contain radioactive elements and are used in the treatment of certain types of cancer.

Inert bioceramics are not usually adopted for regenerative medicine because they promote the formation of a fibrous capsule instead of tissue regeneration[23]. Whereas, Ceramic biomaterials like β-tricalcium phosphate (β-TCP)[12], HAp, bi-phasic calcium phosphate (BCP—a mixture of β-TCP and HAp), calcium sulfate (CS), calcium phosphate cement (CPC)[13], and bioactive glasses (i.e. bioglass)[24] were widely used due to their excellent osteoconductivity and osteoinductivity [25]. In detail, these materials improved the formation of bone-like tissue, as well as the integration of the scaffold to the host tissue. The most representative bioactive ceramics are Ca-P ceramics, including HAp $[Ca_{10}(PO_4)_6(OH)_2]$ and β-TCP $[Ca_3(PO_4)_2]$, which are crystalline ceramics with a structure and chemical composition similar to bone minerals. As biocompatible and bioactive materials, HA and β-TCP, once implanted in vivo, provide appropriate local conditions for cell attachment, proliferation and differentiation through multiple material-host interactions. For this reason, they have attracted the interest of researchers in this field [26]. Despite their excellent biocompatibility characteristics, their brittleness and low toughness have significantly limited their application [57]. To overcome their limitations, they are usually used as fillers in natural or synthetic polymeric materials[27]. As an example of polymer–ceramic synergy, *Marra et al.* found that the addition of HAp to a PCL/PLGA polymer–polymer blend scaffold led to a statistically significant increase in Young's modulus of the samples while also supporting cellular proliferation and collagen deposition [28].*Fiedler et al.* demonstrated that the addition of bioglass to PCL was able to slightly decrease the initial elastic gradient and plateau stress of biomaterial scaffolds[29].*Park et al.* produced composite scaffolds with 50% β-TCP and 50% PCL, and 70% β-TCP with 30% PCL. In detail, the scaffold containing the highest β-TCP content exhibited rougher morphologies and more porosity than the other scaffolds, while in vitro studies revealed that cell proliferation and alkaline phosphate activity were improved on the β-TCP-based composite scaffolds, especially on 70% β-TCP because the β-TCP bioceramic encouraged osteogenic differentiation of cells in the composite scaffolds [30].

1.2.4 Hydrogels

Hydrogels are 3D networks formed by the cross-linkage of hydrophilic polymers held together via covalent bonding or physical attractions that can swell in water and hold a large amount of water while maintaining the structure due to chemical or physical cross-linking of individual polymer chains. Due to their capability to absorb water and swell up, they are more porous and permeable for cell migration and effective transportation of oxygen and nutrient molecules. Once swollen the hydrogel provides sufficient space for the multiplication and growth of cells within their matrix conveniently. PEG, PEGDA, gelatin, HA, methacrylic anhydride (MA), glycosaminoglycan (GAG), methacrylate pullulan, and silk fibroin (SF) are often used to prepare hydrogels. However, components with different biological properties are usually added to hydrogels to improve their properties and solve some problems as the fast degradation rate and poor mechanical strength [31].

1.3 Tissue-engineered Strategies

Bone is a highly hierarchical and specialized tissue with specific pore structures, cellular organization, and material composition that direct its function. So, another materials-based approach for bone regeneration uses structural engineering [32]. A typical example of this approach is pore structure. Macroporosity (pore size $> 50\ \mu m$) has been shown to promote cell growth and support angiogenesis. In contrast, microporosity (pore size $< 10\ \mu m$) plays a role in cell signaling through the transport of biologically active marker agents. A combination of macro- and microporosity can support osteogenesis and angiogenesis throughout the material, assuming these pores are interconnected.

So, the physical characteristics of scaffolds, such as porosity, pore geometry, pore distribution, interconnectivity, and surface topography, offer the passage of nutrients and adhesion of cells that play a crucial role in tissue regeneration to design a product that matches the expected clinical use [33]. However, the design of a porous structure for bone regeneration is a delicate matter, since the volume of the voids is inversely proportional to the overall strength of the material; in fact, Young's modulus decreases as the porosity increases. Therefore, the design of a vascularized bone scaffold requires the consideration of several aspects simultaneously [34]. Many different strategies based on the progress of regenerative medicine and tissue engineering have been proposed and implemented for bone repair and regeneration:

- *scaffold-free strategies*, including tissue-specific cells, genetically modified cells (e.g., induced pluripotent stem cells-iPSCs), and progenitor cells (e.g., bone marrow-derived mesenchymal stem cells (MSCs)[35], decellularized extracellular matrix (dECM)[36], BMSCs [37], adipose-derived mesenchymal stem cells-ADSCs, tendon-derived mesenchymal stem cells-TDSCs),
- *scaffold-based strategies*, such as monophasic scaffolds, biphasic [38, 39] and multi-phasic scaffolds [40, 41], and gradient-designed scaffolds [42],
- *incorporation* with and controlled release of various types of bioactive factors and drugs using different delivery systems.

Among these methods, conventional monophasic scaffolds are not able to repair the deficient cartilage-bone interfacial tissue with anisotropic functional and structural characteristics. For this reason, biphasic two-layer scaffolds, which separately mimic the upper articular cartilage and the underlying subchondral bone, have become popular. Biphasic scaffolds use up to two different types of materials or two respective architectural arrangements with structural disparity, despite being made of only one material [43]. These designs could contribute to forming two opposing regions with distinct structural and mechanical properties. For example, *Wang et al.* fabricated a bilayered tubular nanofibrous scaffold composed of PLA/PLCL microporous inner layer and PLA/PCL macroporous outer layer, matching simultaneously the functional growth of endothelial cells (ECs) and smooth muscle cells (SMCs), and showing the favorable performance for potential small diameter blood vessel application[44]. While, the research group of *Prakobkarn et al.* fabricated a biphasic nanofibrous scaffold, based on COLI and PLC, using the electrospinning technique to establish the controlled release of the antimicrobial peptide LL-37[45]. As well as *Su et al.* that fabricate core–shell PLCL–collagen nanofibers blended with bone morphogenetic protein 2 (BMP2) and dexamethasone (DEX) for controlled release during bone tissue regeneration [46]. However, many studies regarding these bi-layered scaffolds reveal that they are sometimes unstable and incapable of providing sufficient integration with the host tissues.

The natural osteochondral unit displays gradient properties of biochemistry, biomechanics, structure, bioelectricity, and metastasis. Following these features and, also, with the advancement of biotechnology and biomaterial engineering, many researchers tried to simulate the complicated gradient architecture more appropriately by designing gradient scaffolds. Gradient-designed scaffolds mainly focused on the gradual variations of physical structure, and composition, as well as the doses of numerous growth factors. The gradient doses of one single or a cluster of growth factors could be an effective strategy, which could directly guide cell behavior. However, the actual challenges relevant to this strategy lie in the fact that it is quite difficult to fabricate scaffolds with one continuously and uniformly distributed pattern of growth factors. This strategy needs more advanced manufacturing technologies for precisely controlling these fabrication procedures. In the case of scaffold strategies that include several bioactive factors, the organic factors' dose spectrum and release profile must be methodologically optimized and rigorously validated.

In terms of technologies for biomedical applications, over the years interesting advances have been made in developing scaffolds using advanced techniques. In detail, it can be classified into additive and subtractive techniques. *Additive Manufacturing* (AM) is a state-of-the-art technique involving layer-by-layer deposition of materials to obtain structures with desired geometry. In contrast, *Subtractive Manufacturing* is a technique in which a solid mass is reduced to the desired structure/shape by cutting, drilling, or milling. However, due to the bone complex geometry, subtractive techniques are not suitable, so only additive techniques are treated here. Generally, AM techniques are classified into seven categories, namely, binder jetting, direct energy deposition, mask-image projection-based stereolithography, material extrusion, material jetting, photopolymerization, powder bed fusion, and sheet lamination. Most of them require a user-defined computer-aided design (CAD) model or a digital 3D model to design constructs as per requirement.

Anyway, this section has been dedicated to discussing some of the additive manufacturing techniques relevant to bone scaffold development.

1.3.1 Electrospinning

Electrospinning (ESP), also known as electrostatic spinning, is an efficient electrodynamic manufacturing process used both industrially and at the laboratory research level for the production of fibers with extremely small diameters, typically less than a micron, until few nanometers, too. This process allows the fabrication of fibers continuously from polymeric materials that can be brought to a high-viscosity fluid state through a melting process (using heat) or a dissolution in appropriate solvents. This technique is based on the application of a high electric potential between two electrodes of opposite polarities. This high voltage can overcome the surface tension inside a polymeric solution, or melt, allowing the complete evaporation of the solvent and the formation of fibrous structure. In addition, other species such as ceramic particles, metal nanoparticles or functionalized molecules can also be added to the starting solution in order to impart special properties to the final fiber that are useful in highly specialized applications.

Thanks to the small fiber diameters, electrospun structures are generally characterized by high surface-to-volume ratio and high porosity, showing morphological similarities to the fibrillar structures of ECM, offering large surface areas, ease of functionalization, and controllable mechanical properties [47, 48]. So, achieving control of solution electrospinning fiber deposition would enable ESP in direct writing (DW) mode, which would combine the advantages of the topography of electrospun mats with the reproducibility and design potential of AM techniques. Consequently, there has been a significant interest in the development of DW-ESP by various approaches, including beam focusing using additional devices, reducing the working distance, and melting ESP[49]. It is one of the most popular methods because it is easy to use, relatively inexpensive and versatile in terms of material selection, but

ESP is also considered to be a complex hydrodynamic process governed by many technological conditions, such as spinning solution, ambient conditions, and processing parameters.

1.3.2 Solvent Casting and Particulate Leaching

In *Solvent Casting* and *Particulate Leaching* (SCPL), a polymer is dissolved in an organic solvent. Particles, mainly salts, with specific dimensions are then added to the solution. The mixture is shaped into its final geometry. For example, it can be cast onto a glass plate to produce a membrane or in a three-dimensional mold to produce a scaffold. When the solvent evaporates, it creates a structure of composite material consisting of the particles together with the polymer. The composite material is then placed in a bath which dissolves the particles, leaving behind a porous structure. An advantage to this technique is that the pore size and overall porosity can be tuned by changing the particle size, which is fairly reproducible. So, highly porous scaffolds can be produced, which is important for mass transport requirements for cell nutrition, porous channels for cell migration, and surface features for cell attachment. However, an increased porosity can compromise the structural stability. Another drawback of this method is that new tissue formation of often limited to the surface of the construct with minimum cell growth near the centre of necrotic zones in the centre of the construct. Furthermore, in this case, solvent residues from the porogen or solvent could be harmful and/or toxic to cells.

1.3.3 3D Printing

The emerging 3D printing techniques could achieve structural complexity of scaffolds for precise and personalized therapy of osteochondral defect, which employ layer-by-layer deposition and CAD for scaffold production. The most common methods are selective laser sintering, fused deposition modelling, inkjet 3D printing and extrusion-based 3D printing[50]. *Selective Laser Sintering* (SLS) is a technique where a laser source is focused on a powder sample spread over the build platform to develop 3D structures as per design. The laser movement is controlled through laser, and laser fused the powder material forming the layer of 2D structure. Then the sample stage is lowered to spread the second layer of material, and the steps are repeated until the desired structures are obtained. Meanwhile, *Fused Deposition Modeling* (FDM) is a technique where the desired material is heated to melt, extruded through a nozzle, and deposited on a built platform to obtain the desired structures. The nozzle moves in X and Y directions to form the 3D structures; the layer thickness can be controlled by varying nozzle size and process parameters, too [51, 52, 53]. FDM is a reported technique most suitable for thermoplastic polymers. In some cases, bioceramic and metallic powders combined with polymers have been employed in bio-scaffold fabrication using FDM. Fused Granulate Fabrication (FGF) or Fused Pellet Fabrication (FPF) is a technique that is similar to FDM but eliminates the need for filament preparation, using granulates or pellets. It consists of a liquefier when the material is melted with the help of heating bands and extruded through the nozzle [54]. Extrusion-based printing is a very common technique in the field of 3D printing that involves extruding, or forcing, a continuous stream of molten solid material or viscous liquid through an orifice, often a nozzle or syringe. As far as extrusion-based bioprinting is concerned, there are four main types of extrusion. These are pneumatic extrusion, piston extrusion, screw extrusion, and eccentric screw extrusion (also known as progressing cavity pump); let's look at them briefly. in pneumatic extrusion, pressurized air is used to force the liquid through a deposition agent, while in piston extrusion, a piston is connected to a guide screw; the linear movement of the piston squeezes the material out of the nozzle. Screw extrusion uses an auger screw to extrude the material using a rotary motion. Screw devices allow the use of higher-viscosity materials and provide greater volumetric control. While, eccentric screw systems allow for more precise deposition of low- or high-viscosity materials due to the extruder's self-sealing chambers.

Anyway, after printing, many materials require a cross-linking step to achieve the desired mechanical properties for the construct, and these can be realised, for example, through the treatment of chemical or photo-crosslinking agents.

1.3.4 Photopolymerization

Photopolymerization is a technique in which a photocurable liquid material is irradiated with Ultraviolet (UV) or visible light to form 3D structures after cross-linking. The starting material is coated with a metal surface and when the laser beam is aimed at the surface, the material is transferred to the receiving substrate. The design of the scaffolds depends on the type of laser, spot diameter, etc.. Using a similar technique, human umbilical vein endothelial cells (HUVECs) and human umbilical vein smooth muscle cells (HUVSMCs) were printed in branch or stem patterns on the hydrogel layers, without being influenced by the laser.

For thermosetting plastic, a light-emitting device (laser or digital light processing) illuminates and cures a liquid photopolymer resin, layer-by-layer, creating 3D objects; this technique is also known as vat polymerization technique or *Stereolithography* (SLA). It is also possible to print objects "bottom up" by using a vat with a transparent bottom and focusing the UV or deep-blue polymerization laser upward through the bottom of the vat. Meanwhile, the *Digital Light Projection* (DLP) process projects an entire layer of a 3D model all at once, not layer-by-layer as the previous one, curing each point at the same time. Of course, digital projection reduces the resolution of the part, but in the end, it reduces the build time. In contrast to UV lithography and 3D printing via stereolithography, in *Two-Photon Polymerization* (2PP) the resin is not treated with UV light, but with femtosecond or picosecond laser pulses in the visible to near-infrared spectral range. For this reason, It has become one of the leading modern methods for producing customized polymeric devices and surfaces, as equivalent to 3D printing on the microscopic scale.

1.3.5 3D Bioprinting

3D Bioprinting is an additive manufacturing process that uses bio-inks, and/or biomaterials to print living cells developing structures layer-by-layer that imitate the behavior and structures of natural tissues. Bioinks, which are used as a material in bioprinting, are made of natural or synthetic biomaterials that can be mixed and combined with living cells, growth factors, and biomolecules, too. The material choice for 3D bioprinting is reported to use hydrogels with high water content containing cells in most cases because they favor high cell viability, surface tension, and printability[55].

Bioprinting approaches use different techniques such as those discussed previously in the 3D printing section. For example, *direct extrusion* is one of the most common extrusion-based bioprinting techniques, in which the pressure force directs the bioink to flow out of the nozzle and directly print the scaffold without any need for melting[56]. In this case, the bioink can be a mixture of polymeric hydrogels, materials of natural origin such as collagen, and live cells suspended in the solution; in this way, the scaffolds can be grown after printing and without the need for further cell seeding treatments. Some direct-printing techniques rely on the use of coaxial nozzles as they allow the simultaneous extrusion of several bio-inked materials, producing multilayer scaffolds in a single extrusion step. By doing so, tubular structures with radially variable properties can be printed. *Indirect extrusion* techniques for bioprinting, on the other hand, require the printing of a sacrificial hydrogel that can be trivially removed after printing by thermal or chemical extraction. The remaining resin solidifies and becomes the desired 3D-printed construct.

There are several other less commonly used bioprinting techniques; for example, *droplet-based bioprinting* is a technique in which the bio-ink mixture of cells and/or hydrogels is placed at specific locations in the form of droplets. The most common of these approaches are thermal and piezoelectric drop-on-demand techniques. However, extruding cell-laden droplets through a nozzle with an extremely small orifice diameter requires a very high level of pressure, which is sometimes damaging to the cells. In fact, in the field of droplet-based approaches to bioprinting, the study of the mechanical and thermal stresses that cells are forced to undergo within the bioink near the nozzle tip during extrusion has been of significant interest.

1.4 State of the art

For centuries, people have tried to find a way of replacing missing bones. Signs of orthopedic treatment have been found in pre-Columbian and Egyptian culture, but only in the 17^{th} century, the Dutch surgeon *Job Van Meekeren* reported the first successful bone graft, transplanting a piece of dog bone into a soldier's damaged skull. Nevertheless, it was in the 19^{th} century that the first successful autologous transplant was reported [57]. In 2001, bone grafting represented more than 2 million procedures per year in the world, with autograft, which is considered the gold standard technique, being widely used. Meanwhile, commercially available tissue-engineered grafts, such as *Chondrotissue* (BioTissue, Switzerland), *Hyalofast* (Fidia Advanced Biopolymers, Italy), *Chondro-Mimetic* (TiGenix N.V., Belgium), *TruFit®BGS Plugs* (Smith &Nephew, United Kingdom), *MaioRegen* (Finceramica spa, Italy),[58] have used for the treatment of small cartilage and osteochondral defects. Unfortunately, none of these until now has demonstrated the appropriate biomechanical properties necessary to promote satisfactory and durable regeneration of large bone defects, besides the problem of poor bone filling and fibrocartilage formation. Therefore, the demand for new therapeutic options for complete bone healing becomes increasingly intense.

The tailored multiple shapes and size with desirable porosity according to cell migration speed or tissue in-growth makes synthetic polymers attractive. Additionally, the huge technical progress in 3D printing has enabled the fabrication of scaffolds faster. Among synthetic polymers, PLA and PCL are the most widely used polymers in TE. In detail, PLLA and PCL are linear aliphatic polyesters with similar chemical structures. As compared to PCL, PLA has more ester groups per chain, hence it degrades more readily by hydrolysis and shows faster biodegradability. With a crystallinity of $\simeq 37\%$, PLA has superior mechanical properties such as high stiffness and high strength. Moreover, it shows lower elasticity and flexibility. However, PLA is brittle at a body temperature of $37°C$ due to its high glass transition temperature ($T_g \simeq 65°C$). Therefore, it is not suitable to be used in some biomedical applications. In TE, citrate esters, PEG, glucose monoesters, partial fatty acids, oligomeric lactic acid, and glycerol were used as plasticizers for PLA, increasing its elongation at break and impact resistance [59]. For example, *Tachibana et al.* found that myo-inositol, a sugar present in the human body and involved in cell signal transduction, had a stabilization effect on PLLA during processing [60]. Similarly, *Calore et al.* used cholecalciferol, the metabolically inactive form of vitamin D3 (VD3), as the plasticization of poly(D, L-lactic acid) (PDLLA) [61]. Otherwise, PCL is a biodegradable polymer and has been widely used to fabricate tissue scaffolds because of its good biocompatibility, excellent mechanical properties, exceptional melt flow properties, and good resistance to water, oil, solvent, and chlorine [62]. Because PCL has more alkyl units between the ester links than PLA, it has high flexibility with an elongation at break of about 600% at room temperature, and a low melting point ($60°C$), thus it behaves as a tough polymer at $37°C$, like a semi-crystalline polymer with rubbery properties [59, 63, 64]. However, neat PCL has low surface energy which results in a lack of attachment signals and consequently decreases cell adhesion on the surface, and osteoinduction. Moreover, PCL has a long degradation time and lacks elasticity. Therefore, blending PLA and PCL is the most versatile and cheapest method in industrial settings to improve PLA toughness, crystallization, and biodegradability [65, 66]. Blends of PLA with PCL have been extensively studied, as PCL could improve the toughness of PLA and retain its biodegradability [67, 68, 69]. However, there isn't a favorable interactions between these two polymers and, consequently, many studies focused on improving PLA/PCL miscibility, using different strategies, such as the introduction of a new polymer [70, 71], nanoparticles [72, 73], and co-polymers [74, 75, 76].

A more eco-friendly alternative is to blend PCL with naturally derived polymers, such as CA, an organic compound that has shown advanced properties in vitro and in vivo, making it suitable for various biomedical applications [78, 79, 80]. Biopolymers of CA were used to increase the long degradation time and low elasticity of PCL [81, 82, 83, 84, 85]. Most importantly, a combination of Starch and CA has shown biocompatibility, heterogeneous nucleation of Hap crystals, appropriate pores for increasing oxygen permeability and nutrient supply to deeper regions [86], and enhancement of barrier property [87]. Similarly, Starch, a low-cost polysaccharide, tasteless and odorless, produced by most green plants for energy storage and widely present as a common carbohydrate in human diets [88], has been used as an alternative to petroleum derivatives due to its ability to increase the rate of biodegradation [89]. Pure starch consists of two types of molecules: the linear and helical amylose and the branched amylopectin. Depending on the plant, starch generally contains from 20 to 25% amylose and from 75 to 80% amylopectin by weight. However, due to the limitations of native starch, such as insolubility in cold water or alcohol, and limitations of breaking down when reheated or treated in acidic environments, various physical, chemical, and enzymatic modifications have been explored to improve its functional properties and facilitate its application for different purposes. Glycerol, also called glycerine or glycerin, a clear, colorless, viscous, sweet-tasting, and non-toxic liquid belonging to the alcohol family of organic compounds ($C_3H_8O_3$), is the most used to increase starch plasticity, filler-matrix interaction, as well as thermal and mechanical behavior [90, 91, 92]. For its properties, It has varied uses in the pharmaceutical and toilet goods fields including skin lotions, mouthwashes, cough medicines, drug solvents, serums, vaccines, and suppositories. Another significant use is as a protective medium for freezing red blood cells, sperm cells, eye corneas, and other living tissues.

1.5 Results

Bone regeneration is a rapidly evolving field of research that aims to develop new strategies to repair and regenerate damaged or lost bone tissue. Although many studies have focused on developing “the perfect biomaterial” with a combination of suitable physicochemical, mechanical, and biological properties, the complete regeneration of critical bone defects remains a great challenge in medicine. So, the aim of this study, as reflected in the ongoing doctoral thesis, is to study and implement a scaffold, as well as a biomechanical model, for the regeneration of bone tissue.

The development process of scaffolds, grafts or implants requires a biomechanical model capable of describing the mechanical response of these artificial tissues. So, firstly there will be an overview of biomechanics and, consequently, of the most widely mechanical model used and adopted for biological tissue characterization in *Chapter 2*. Meanwhile, a new biomechanical model will be introduced in *Chapter 3*. Here, the use of Fractional Calculus demonstrated how it is possible to overcome the limitations of classical models that consider biological tissues as solid materials (e.g. metals) or liquid materials (e.g. water). Thus, the fundamentals of fractional calculus will first be introduced, followed by the governing equations. Each term, as well as the mathematical steps, will be explained and defined step-by-step, up to the "in silico" virtual simulation of mechanics behavior. Once the foundations of the biomechanics of the problem are established, it is then possible to move on to the actual production of the scaffolds.

According to materials properties and basic requirements such as biocompatibility, mechanical stability, and biodegradation rate, natural polymeric materials were selected for the design and development of an innovative 3D scaffold for bone regeneration. In detail, PLA/PCL blends have shown great interest in regenerative medicine because of their excellent properties, easy availability, versatility, and low cost. Consequently, the research will start with preparing, analysing, and characterizing of PLA/PCL blends in different ratios in *Chapter 4*. In this contest, these blends will be used to study and investigate the potential of producing a gradient structure by exploiting the materials' immiscibility.

After that, a new eco-friendly blend will be introduced. In detail, a mixture of Starch, CA, PCL, and Glycerol in different ratios will be blended and further analyzed. Anyway, considering the importance of using a technique that must be easy to adopt for industrial application, versatile, low cost, and does not require toxic agents, and/or a post-processing step, 3D printing was selected as the AM technique for the current research project. This technique reduces production time, limiting costs and waste but also ensuring commercial viability and workability compared to other techniques such as electrospinning or particulate leaching. In this context, it is also important to consider the parameters that can be controlled and modified to optimize the final properties of printed scaffolds. So, the obtained scaffolds will be subjected to characterization tests to investigate their mechanics and thermal, physical, and morphological properties.

These analyses, and the model presented and discussed here, are fundamental to the development and realization of a new scaffold for bone regeneration that can be applied in tissue engineering. Indeed, we attempted to combine different aspects of engineering, from design engineering to modeling, but also tissue and product engineering, giving a complete and unified view of this research project. Moreover, in biomedical engineering, scaffold structures are vital in tissue engineering and regenerative medicine since they provide a three-dimensional framework that facilitates cell attachment, proliferation, and differentiation, ultimately leading to the formation of functional tissues. For this reason, various structures were also considered and analyzed by simulation software to compare their mechanical and structural results.

Bibliography

[1] Rinaldo Florencio-Silva, Gisela Rodrigues da Silva Sasso, Estela Sasso-Cerri, Manuel Jesus Simões, P. S. C. Physiology of bone tissue.*Immuno-analyse & Biologie Spécialisée* 7, 17–24 **2015**.

[2] Mikael, P. E. et al. Functionalized carbon nanotube reinforced scaffolds for bone regenerative engineering: Fabrication, in vitro and in vivo evaluation. *Biomedical Material.* 9, **2014**.

[3] Winn, S. R. et al. Tissue-engineered bone biomimetic to regenerate calvarial critical-sized defects in athymic rats. *Journal of Biomedical Materials Research* 45, 414–421 **1999**.

[4] Amendola, A. & Bonasia, D. E. Results of high tibial osteotomy: Review of the literature. *International Orthopaedics*vol. 34, 155–160 **2010**.

[5] Yin, S., Zhang, W., Zhang, Z. & Jiang, X. Recent Advances in Scaffold Design and Material for Vascularized Tissue-Engineered Bone Regeneration. *Advanced Healthcare Materials* 8, 1801433, **2019**.

[6] Atala, A., Lanza, R., Thomson, J. A. & Nerem, R. M. Principles of Regenerative Medicine. **2008**. doi:10.1016/B978-0-12-369410-2.X5001-3.

[7] Lanza, R., Langer, R. & Vacanti, J. P. Principles of Tissue Engineering: Fourth Edition. **2013**. doi:10.1016/C2011-0-07193-4.

[8] Francois, E., Dorcemus, D. & Nukavarapu, S. Biomaterials and scaffolds for musculoskeletal tissue engineering. Regenerative Engineering of Musculoskeletal Tissues and Interfaces *Elsevier Ltd*, **2015**. doi:10.1016/B978-1-78242-301-0.00001-X.

[9] Tan, Y. J. et al. Characterization, mechanical behavior, and in vitro evaluation of a melt-drawn scaffold for esophageal tissue engineering. *Journal of the Mechanical Behavior of Biomedical Materials* 57, 246–259 **2016**.

[10] Chauhan, A. & Bhatt, A. D. A review on design of scaffold for osteoinduction: Toward the unification of independent design variables. *Biomechanics and Modeling in Mechanobiology*, 22, 1–21 **2023**.

[11] Polo-Corrales, L., Latorre-Esteves, M. & Ramirez-Vick, J. E. Scaffold design for bone regeneration. *Journal of Nanoscience and Nanotechnology* 14, 15–56, **2014**.

[12] Deng, Y. et al. 3D printed scaffolds of calcium silicate-doped β-TCP synergize with co-cultured endothelial and stromal cells to promote vascularization and bone formation. *Scientific Reports* 7, 1–14, **2017**.

[13] Wu G, Liu Y, Iizuka T, Hunziker EB. Biomimetic coating of organic polymers with a protein-functionalized layer of calcium phosphate: the surface properties of the carrier influence neither the coating characteristics nor the incorporation mechanism or release kinetics of the protein. *Tissue Engineering Part C: Methods* .16(6):1255-65,**2010**. doi: 10.1089/ten.TEC.2009.0588.

[14] Jammalamadaka, U. & Tappa, K. Recent advances in biomaterials for 3D printing and tissue engineering. *Journal of Functional Biomaterials* 9, **2018**.

[15] Yokoya, S., Mochizuki, Y., Nagata, Y., Deie, M. & Ochi, M. Tendon-bone insertion repair and regeneration using polyglycolic acid sheet in the rabbit rotator cuff injury model. *The American Journal of Sports Medicine* 36, 1298–1309,**2008**.

[16] Walejewska, E. et al. The effect of introduction of filament shift on degradation behaviour of PLGA- and PLCL-based scaffolds fabricated via additive manufacturing. *Polymer Degradation and Stability* 171, 109030, **2020**.

[17] Alluri, R. et al. 3D Printed Hyperelastic “Bone” Scaffolds and Regional Gene Therapy: A Novel Approach to Bone Healing. 1–15 **2018**.

[18] Jegal, S. H. et al. Functional composite nanofibers of poly(lactide-co-caprolactone) containing gelatin-apatite bone mimetic precipitate for bone regeneration.*Acta Biomaterial.* 7, 1609–1617, **2011**.

[19] Liu, X. et al. Thermal, mechanical and degradation properties of flexible poly (1,3-trimethylene carbonate)/poly (L-lactide-co-ϵ-caprolactone) blends. *Journal of Polymer Research* 28, **2021**.

[20] Sriyai, M. et al. Development of an Antimicrobial-Coated Absorbable Monofilament Suture from a Medical-Grade Poly(l -lactide- co-ϵ-caprolactone) Copolymer. *ACS Omega* 6, 28788–28803, **2021**.

[21] Song, X. et al. Bioinspired Protein/Peptide Loaded 3D Printed PLGA Scaffold Promotes Bone Regeneration. *Frontiers in Bioengineering and Biotechnology.* 10, 1–12 **2022**.

[22] Tebon, P. J. et al. A 3D bioprinted complex structure for engineering the muscle – tendon unit. *Biofabrication* 7, 35003, **2015**.

[23] Taboas, J. M., Maddox, R. D., Krebsbach, P. H. & Hollister, S. J. Indirect solid free form fabrication of local and global porous, biomimetic and composite 3D polymer-ceramic scaffolds. *Biomaterials* 24, 181–194, **2003**.

[24] Fiedler, T. et al. On the mechanical properties of PLC-bioactive glass scaffolds fabricated via BioExtrusion. *Materials Science and Engineering: C* 57, 288–293 **2015**.

[25] Vaiani, L. et al. Ceramic Materials for Biomedical Applications: An Overview on Properties and Fabrication Processes. *Journal of Functional Biomaterials.* 14, **2023**.

[26] Panseri, S. et al. Bone-like ceramic scaffolds designed with bioinspired porosity induce a different stem cell response. *Journal of Materials Science: Materials in Medicine* vol. 32, ;**2021**.

[27] Hassanajili, S., Karami-Pour, A., Oryan, A. & Talaei-Khozani, T. Preparation and characterization of PLA/PCL/HA composite scaffolds using indirect 3D printing for bone tissue engineering. *Materials Science and Engineering: C* 104, 109960 **2019**.

[28] Marra, K. G., Szem, J. W., Kumta, P. N., Dimilla, P. A., & Weiss, L. E. In vitro analysis of biodegradable polymer blend/hydroxyapatite composites for bone tissue engineering. *Journal of Biomedical Materials Research*, 47, 324–335.**1999**.

[29] Fiedler, T. et al. On the mechanical properties of PLC-bioactive glass scaffolds fabricated via BioExtrusion. *Materials Science and Engineering: C* 57, 288–293, **2015**.

[30] Park, J. S. et al. Fabrication and characterization of 3D-printed bone-like β-tricalcium phosphate/polycaprolactone scaffolds for dental tissue engineering. *Journal of Industrial and Engineering Chemistry* 46, 175–181 **2017**.

[31] Guo, X. et al. Regeneration of articular cartilage defects: Therapeutic strategies and perspectives. *Journal of Tissue Engineering* 14, **2023**.

[32] Wegst, U. G. K., Bai, H., Saiz, E., Tomsia, A. P. & Ritchie, R. O. Bioinspired structural materials. *Nature Materials* vol.14, 23–36, **2015**.

[33] Moroni, L., De Wijn, J. R. & Van Blitterswijk, C. A. 3D fiber-deposited scaffolds for tissue engineering: Influence of pores geometry and architecture on dynamic mechanical properties. *Biomaterials* 27, 974–985, **2006**.

[34] Hollister, S. J., Maddox, R. D. & Taboas, J. M. Optimal design and fabrication of scaffolds to mimic tissue properties. *Biomaterials* 23, 4095–4103, **2002**.

[35] Hokugo, A. et al. Prefabrication of vascularized bone graft using guided bone regeneration. *Tissue Engineering.* 10, 978–986 ,**2004**.

[36] Lee, S. et al. Enhanced regeneration of vascularized adipose tissue with dual 3D-printed elastic polymer/dECM hydrogel complex. *International Journal of Molecular Sciences* 22, 1–22 **2021**.

[37] Shim, J. H. et al. Three-dimensional printing of rhBMP-2-loaded scaffolds with long-term delivery for enhanced bone regeneration in a rabbit diaphyseal defect.*Tissue Engineering- Part A* 20, 1980–1992 **2014**.

[38] Hwang, K. S. et al. Comparative efficacies of collagen-based 3D printed PCL/PLGA/β-TCP composite block bone grafts and biphasic calcium phosphate bone substitute for bone regeneration. *Materials (Basel).* 10, **2017**.

[39] Jegal, S. H. et al. Functional composite nanofibers of poly(lactide-co-caprolactone) containing gelatin-apatite bone mimetic precipitate for bone regeneration. *Acta Biomaterial.* 7, 1609–1617 **2011**.

[40] Kellomäki, M. et al. Bioabsorbable scaffolds for guided bone regeneration and generation.*Biomaterials* 21, 2495–2505 , **2000**.

[41] Nandakumar A, Fernandes H, de Boer J, Moroni L, Habibovic P, van Blitterswijk CA. Fabrication of bioactive composite scaffolds by electrospinning for bone regeneration. *Macromolecular Bioscience* 10(11):1365-73.**2010**. doi: 10.1002/mabi.201000145.

[42] Qiu, J., Ahn, J., Qin, D., Thomopoulos, S. & Xia, Y. Biomimetic Scaffolds with a Mineral Gradient and Funnel-Shaped Channels for Spatially Controllable Osteogenesis. *Advanced Healthcare Materials* . vol. 11, 1–8 ,**2022**.

[43] He, Y. et al. A 3D-Printed PLCL Scaffold Coated with Collagen Type i and Its Biocompatibility. *BioMed Research International* , **2018**.

[44] Wang, W. et al. Fabrication of heterogeneous porous bilayered nanofibrous vascular grafts by two-step phase separation technique. *Acta Biomaterialia.* 79, 168–181, **2018**.

[45] Prakobkarn, J. et al. Biphasic nanofibrous scaffolds based on collagen and PLC for controlled release LL-37 in guided bone regeneration. *Journal of Applied Polymer Science* 139, 1–10, **2022**.

[46] Su, Y. et al. Controlled release of bone morphogenetic protein 2 and dexamethasone loaded in core-shell PLLACL-collagen fibers for use in bone tissue engineering. *Acta Biomaterialia* 8, 763–771, **2012**.

[47] Chen, Y. et al. Three-dimensional porous gas-foamed electrospun nanofiber scaffold for cartilage regeneration. *Journal of Colloid and Interface Science* 603, 94–109, **2021**.

[48] Li, T. et al. Fabrication, mechanical property and in vitro evaluation of poly (L-lactic acid-co-ε-caprolactone) core-shell nanofiber scaffold for tissue engineering. *Journal of the Mechanical Behavior of Biomedical Materials* 98, 48–57, **2019**.

[49] Chen H, Malheiro ABFB, van Blitterswijk C, Mota C, Wieringa PA, Moroni L. Direct Writing Electrospinning of Scaffolds with Multidimensional Fiber Architecture for Hierarchical Tissue Engineering.*ACS Applied Materials & Interfaces* ;9(44):38187-38200. doi: 10.1021/acsami.7b07151. **2017**.

[50] Niu, X., Li, N., Du, Z. & Li, X. Integrated gradient tissue-engineered osteochondral scaffolds: Challenges, current efforts and future perspectives. *Bioactive Materials* 20, 574–597 **2023**.

[51] Yu, K., Gao, Q., Lu, L. & Zhang, P. A Process Parameter Design Method for Improving the Filament Diameter Accuracy of Extrusion 3D Printing. *Materials (Basel).* 15, **2022**.

[52] Jain, S., Fuoco, T., Yassin, M. A., Mustafa, K. & Finne-Wistrand, A. Printability and Critical Insight into Polymer Properties during Direct-Extrusion Based 3D Printing of Medical Grade Polylactide and Copolyesters. *Biomacromolecules* 21, 388–396, **2020**.

[53] L. Moroni, G. Poort, F. Van Keulen, J.R. de Wijn, C. A. van B. Dynamic mechanical properties of 3D fiber-deposited PEOT PBT scaffolds An. *Journal of Biomedical Materials Research*, **2006**.

[54] Tan, Y. J., Tan, X., Yeong, W. Y. & Tor, S. B. Additive manufacturing of patient-customizable scaffolds for tubular tissues using the Melt-Drawing Method. *Materials (Basel).* 9, **2016**.

[55] Kang, H. et al. A 3D bioprinting system to produce human-scale tissue constructs with structural integrity. *Nature Biotechnology* 34, **2016**.

[56] Datta P., Ayan B., Ozbolat I. T. Bioprinting for vascular and vascularized tissue biofabrication. *Acta Biomaterialia.* 51: 1–20. doi:10.1016/j.actbio.2017.01.035.**2017**

[57] Fernandez de Grado, G. et al. Bone substitutes: a review of their characteristics, clinical use, and perspectives for large bone defects management.*Journal of Tissue Engineering* 9, **2018**.

[58] Zhou, L. et al. Innovative Tissue-Engineered Strategies for Osteochondral Defect Repair and Regeneration: Current Progress and Challenges. *Advanced Healthcare Materials* vol. 9, 2001008 , **2020**.

[59] Martin, O. & Avérous, L. Poly(lactic acid): Plasticization and properties of biodegradable multiphase systems. *Polymer (Guildf)*. 42, 6209–6219, **2001**.

[60] Tachibana, Y., Maeda, T., Ito, O., Maeda, Y. & Kunioka, M. Biobased myo-inositol as nucleator and stabilizer for poly(lactic acid). *Polymer Degradation and Stability* vol. 95, 1321–1329, **2010**.

[61] Calore, A. R. et al. Cholecalciferol as Bioactive Plasticizer of High Molecular Weight Poly(D,L-Lactic Acid) Scaffolds for Bone Regeneration. *Tissue Engineering Part C: Methods* vol. 28, 335–350 **2022**.

[62] Williams, J. M. et al. Bone tissue engineering using polycaprolactone scaffolds fabricated via selective laser sintering. *Biomaterials* 26, 4817–4827 ,**2005**.

[63] Elnaggar, M. A., El-Fawal, H. A. N. & Allam, N. K. Biocompatible PCL-nanofibers scaffold with immobilized fibronectin and laminin for neuronal tissue regeneration. *Materials Science and Engineering: C* 119, 111550 **2021**.

[64] Tan, Y. J. et al. Characterization, mechanical behavior and in vitro evaluation of a melt-drawn scaffold for esophageal tissue engineering. *Journal of the Mechanical Behavior of Biomedical Materials* vol. 57, 246–259, **2016**.

[65] Zhang, C. et al. Melt crystallization behavior and crystalline morphology of Polylactide/Poly(ϵ-caprolactone) blends compatibilized by lactide-caprolactone copolymer. *Polymers (Basel).* 10; **2018**.

[66] Camarero-espinosa, S. & Moroni, L. Janus 3D printed dynamic scaffolds for nanovibration-driven bone regeneration. *Nature Communications* 1–12, doi:10.1038/s41467-021-21325-x.

[67] Oliveira, C. S., Leeuwenburgh, S. & Mano, J. F. New insights into the biomimetic design and biomedical applications of bioengineered bone microenvironments.*APL Bioengineering* 5, **2021**.

[68] Castañeda-Rodríguez, S. et al. Recent advances in modified poly (lactic acid) as tissue engineering materials.*Journal of Biological Engineering* 17, 1–20 ,**2023**.

[69] Polo-Corrales, L., Latorre-Esteves, M. & Ramirez-Vick, J. E. Scaffold design for bone regeneration. *Journal of Nanoscience and Nanotechnology* 14, 15–56 ,**2014**.

[70] Zhou, Y. et al. Polymerized Ionic Liquid for the Regulation of Phase Structure of PLA/PCL Blends.*Macromolecular Research* 30, 631–637 ,**2022**.

[71] Hassanajili, S., Karami-Pour, A., Oryan, A. & Talaei-Khozani, T. Preparation and characterization of PLA/PCL/HA composite scaffolds using indirect 3D printing for bone tissue engineering.*Material Science and Engineering: C* 104, 109960 ,**2019**.

[72] Lim, J. I. Fabrication of 3D Self-Assembled Porous Microbead-Type Poly(l-Lactide-co-ε-Caprolactone) Scaffolds for Tissue Engineering. 3D Print. Addit. Manuf. 6, 204–209 (2019).

[73] Salerno, A., Guarino, V., Oliviero, O., Ambrosio, L. & Domingo, C. Bio-safe processing of polylactic-co-caprolactone and polylactic acid blends to fabricate fibrous porous scaffolds for in vitro mesenchymal stem cells adhesion and proliferation.*Material Science and Engineering: C* vol. 63, 512–521, **2016**.

[74] Omar, E., Cary, V. & Gall, K. Structure-property relationships in 3D-printed poly (L -lactide- co - ϵ -caprolactone) degradable polymer. *Journal of the Mechanical Behavior of Biomedical Materials* vol. 121, **2021**.

[75] Sanchez Diaz, R. et al. Highly Elastic Scaffolds Produced by Melt Electrowriting of Poly(L-lactide-co-ϵ-caprolactone). *Advanced Materials Technologies* 7, 1–10 ,**2022**.

[76] Liu, X. et al. Biodegradable cross-linked poly(L-lactide-co-ϵ-caprolactone) networks for ureteral stent formed by gamma irradiation under vacuum. *Journal of Industrial and Engineering Chemistry* 104, 73–84, **2021**.

[77] Kim, J. H. et al. Performance of novel nanofibrous biopolymer membrane for guided bone regeneration within rat mandibular defect. *In Vivo (Brooklyn).* 25, 589–595 **2011**.

[78] Yu, M., Du, Y., Han, Y. & Lei, B. Biomimetic Elastomeric Bioactive Siloxane-Based Hybrid Nanofibrous Scaffolds with miRNA Activation: A Joint Physico-Chemical-Biological Strategy for Promoting Bone Regeneration. *Advanced Functional Materials* vol. 30, 1–12v**2020**.

[79] Salihu, R. et al. Citric acid: A green cross-linker of biomaterials for biomedical applications. *European Polymer Journal* vol. 146, 110271 ;**2021**.

[80] Potter, E. &. The Important Role of Osteoblasts and Citrate Production in Bone Formation: "Osteoblast Citration" as a New Concept for an Old Relationship. Bone 23, 1–7; **2008**.

[81] Wang, M. et al. Photoluminescent and biodegradable polycitrate-polyethylene glycol-polyethyleneimine polymers as highly biocompatible and efficient vectors for bioimaging-guided siRNA and miRNA delivery. *Acta Biomaterialia* vol. 54, 69–80; **2017**.

[82] Yuzhang Du , Yumeng Xue , Peter X. Ma , Xiaofeng Chen, and B. L. Biodegradable Elastomeric and Intrinsically Photoluminescent Poly Silicon-Citrates. doi:10.1002/adhm.201500643.

[83] Du, Y. et al. Development of a Multifunctional Platform Based on Strong, Intrinsically Photoluminescent and Antimicrobial Silica-Poly(citrates)-Based Hybrid Biodegradable Elastomers for Bone Regeneration. *Advanced Functional Materials* vol. 25, 5016–5029 ;**2015**.

[84] Averous, L., Moro, L., Dole, P. & Fringant, C. Properties of thermoplastic blends: Starch-polycaprolactone. *Polymer (Guildf).* 41, 4157–4167; **2000**.

[85] Sun, Y. et al. Preparation and properties of thermoplastic poly(caprolactone) composites containing high amount of esterified starch without plasticizer. *Carbohydrate Polymers* vol. 139, 28–34 ;**2016**.

[86] Saliu, O. D. et al. Barrier property enhancement of starch citrate bioplastic film by an ammonium-thiourea complex modification.*Journal of Saudi Chemical Society* vol. 23, 141–149, **2019**.

[87] Nourmohammadi, J., Shahriarpanah, S., Asadzadehzanjani, N., Khaleghpanah, S. & Heidari, S. Biomimetic apatite layer formation on a novel citrate starch scaffold suitable for bone tissue engineering applications. Starch/Staerke 68, 1275–1281 ;**2016**.

[88] Gunawardene, O. H. P. et al. Compatibilization of starch/synthetic biodegradable polymer blends for packaging applications: A review. *Journal of Composites Science* vol. 5, 1–33; **2021**.

[89] Sarder, R. et al. Copolymers of starch, a sustainable template for biomedical applications: A review. *Carbohydrate Polymers* vol. 278, 118973;**2022**.

[90] He, X. et al. A combined extrusion, retrogradation, and cross-linking strategy for preparing starch-based straws with desirable mechanical properties. *International Journal of Biological Macromolecules* vol. 227, 1089–1097 ;**2023**.

[91] Ortega-Toro, R., Muñoz, A., Talens, P. & Chiralt, A. Improvement of properties of glycerol plasticized starch films by blending with a low ratio of polycaprolactone and/or polyethylene glycol.*Food Hydrocolloids* vol. 56, 9–19;**2016**.

[92] Averous, L. & Boquillon, N. Biocomposites based on plasticized starch: Thermal and mechanical behaviours. *Carbohydrate Polymers* vol. 56, 111–122; **2004**.

Chapter. 2

Biomaterial Hereditariness

Biomechanics applies the principles and techniques of mechanics to biology, particularly the study of the mechanical responses of biological tissues and, consequently, the behavior of the human body. This research work focuses on the biomechanics of porous biphasic tissues, a fundamental field of study for understanding the structure and function of the skeletal system.

Bones are complex structures that perform multiple functions in the human body. They provide structural support, protect vital organs, facilitate movement through interaction with muscles, and serve as a reservoir of essential minerals. From a mechanical point of view, bones are usually classified as viscoelastic hereditariness materials. Viscoelastic materials are unique substances that exhibit both viscous and elastic characteristics when undergoing deformation. This behavior is typical of polymers[1], biological tissue such as ligaments[2], tendons[3], skeletal muscles[4], and bones[5, 6], but also various mortars, and resins used in the construction[7], some families of rocks[8], and other materials. These materials have properties that depend on the rate of deformation.

Viscous materials, like honey, resist shear flow and strain linearly with time when stress is applied. On the other hand, *Elastic materials*, such as rubber bands and springs, store and recover energy. Viscoelastic materials have elements of both; this means they exhibit a strain rate dependent on time and also can bounce back to their original state after the removal of stress. The behavior of viscoelastic materials is often displayed through a phenomenon known as creep, where the material continues to deform over time under a constant applied force, and stress relaxation, where under a constant strain, the stress in the material decreases over time.

Understanding the properties of viscoelastic materials is crucial in various fields, including materials science, mechanical engineering, and biomedical applications. For example, in biomedical engineering, the viscoelastic properties of biological tissues can impact the design and function of implants or prosthetics. It is axiomatic that a repaired or replaced tissue must possess the same hereditary characteristics as a healthy tissue to provide the same function. It is also interesting to know the difference in performance between healthy and damaged tissue. For these reasons, it is important to understand hereditary behavior throughout its functional range.

From a mechanical point of view, the universal tensile machine is standard in classical engineering for characterizing the material behavior (i.e., metals). This test can be performed with force control or displacement control, based on which parameter is given as input to the machine: if a force is impressed on the specimen, it is a force control test, while if a displacement is applied, it is a displacement control test. In any case, the test result will be a stress-strain curve that will fully characterize the mechanical response of the material. However, due to the special properties, a simple tensile test is not sufficient to fully characterize a biological tissue. So, any biological material can be subjected to two different types of mechanical tests, which are essential for the characterization of hereditary materials: Creep testing consists of the application of a stress history to the sample; the engineering stress (σ) is described as a force (F) per unit area (A).

$$\sigma[Pa] = \frac{F}{A} \tag{2.1}$$

Stress Relaxation testing consists of the application of a strain history to the sample; the engineering strain (ε) is described as the change in length (Δl) of the sample relative to its initial length (l_o).

$$\varepsilon[\%] = \frac{\Delta l}{l_0} \cdot 100\% \tag{2.2}$$

In the field of biomedical engineering, the viscoelastic properties of materials play an important role, especially due to their influence on the long-term behavior of biological tissues. Therefore, for the viscoelastic characterization of materials, it is necessary to introduce the time variable. For this reason, tension history and deformation history will be used. In the context of linear viscoelasticity, the response (in terms of tension or deformation) at the generic time considered will be a consequence of all previous events that have affected the material, as the principle of superposition of effects is still valid.

The concept of linear viscoelasticity, as well as that of material hereditariness, the basic principles and mathematical models used will be further described in *Section 2.1.* Meanwhile, the basic equation of *Fractional Hereditary Materials* (FHM) in the uniaxial case will be introduced in *Section 2.2*, as well as in the three-axial case in *Section 2.3.*

2.1 Viscoelasticity

The term viscoelasticity indicates the intermediate behavior of a material between elastic solid and viscous liquid. For elastic solids, deformation occurs when subjected to external loads, but as soon as the action of external forces stops, they return to their initial shape. For Newtonian fluids, on the contrary, the internal forces do not depend on the deformation but linearly depend on the rate at which this deformation is impressed. A perfectly elastic solid is characterized by a linear relationship between stress and strain over time, and is described by *Hooke's law* as follows:

$$\sigma(t) = E\varepsilon(t) \tag{2.3}$$

Where E $[Pa]$ is the *Young Modulus*[9, 10], is characteristic of the specific material but also depends on temperature. Generally, this mechanical response is represented by a spring with stiffness E. The energy spent is stored by the solid, which in fact returns to its initial configuration when the effect of the external stress stops, just like a spring. A viscous fluid is described by *Netwon-Petroff's law* as follows:

$$\sigma(t) = \eta\dot{\varepsilon}(t) \tag{2.4}$$

Where η $[Pa \cdot s]$ is the *fluid viscosity*, which depends on the material and generally decreases with increasing temperature. Here there is a linear dependence between stress and strain rate, i.e. to the strain time derivative. The energy spent is not stored by the fluid it does not return to its initial configuration, and is therefore fully transformed into heat dissipation. In other words, a viscous fluid flows irreversibly under the effect of external stress. In this case, the mechanical response is represented by a viscous dashpot with a viscosity coefficient η. This is only applicable to Newtonian fluids, but it is important to specify that there are also other types of fluids, which will not be discussed here.

2.1.1 Viscoeslastic Models

Viscoelastic materials are so-called because they exhibit an intermediate behavior between the elastic solid and viscous fluid. Consequently, Hooke and Newton's models represent the limiting cases of viscoelastic bodies. All materials are viscoelastic, i.e., if a constant load is applied to a solid, it is observed that the deformation increases over time, i.e. it flows (*Creep*), on the contrary, if a constant deformation is applied, the tension decays over time (*Relaxation*). Naturally, these phenomena are more pronounced for certain materials such as rubbers or polymers, and less pronounced for others, such as steels. Historically, this intermediate behavior has been schematized with springs and dashpots combined in various ways, i.e. series or parallel.

The *Maxwell Model* is a type of simplest and basic mathematical model to describe the mechanics characteristic of viscoelastic solid material. It can be represented and described by a material with a linear Hookean spring connected in series with a Newtonian dashpot. The total stress and strain of the Maxwell model can be determined as indicated in Eq.2.5:

$$\dot{\sigma}(t) + \nu\sigma(t) = E\dot{\varepsilon}(t) \tag{2.5}$$

Where: ν=E/η $[s^{-1}]$.

Another classical model used to describe viscoelastic behavior is the of *Kelvin-Voigt Model*, obtained by coupling in parallel a spring of stiffness E and a dashpot of viscosity η. In this case, the spring stress and the plunger stress are different, but the deformation of the two elements is equal, so the total stress will be:

$$\sigma(t) = E\varepsilon(t) + \eta\dot{\varepsilon}(t) \tag{2.6}$$

By increasing the number of simple elements in the Kelvin-Voigt model, other more accurate models are obtained in the simulation of viscoelastic behavior. These models are called *Standard Linear Solid* or *Zener*. The simplest viscoelastic model is obtained by adding a spring either in series to a Voigt model or in parallel to a Maxwell model, respectively. They are qualitatively satisfactory but, as they also require more parameters in the optimization procedure to approximate the experimental data (best fitting), they also require a higher computational workload. In addition to complicating resolution, increasing the number of elements often also leads to a violation of the physical meaning of the model, such as negative viscosity.

2.1.2 Creep and Relaxation Function

The *Creep Function* is the deformation response to a unit stress. In the context of linear viscoelasticity, this function denoted $J(t)$, is an increasing monotonous function since, as the tension increases, the deformation increases proportionally. Let a specimen be subjected to a step stress history as reported in *Figure 2.1*. The stress is instantaneously increased to some value σ_0 at $t = 0$ and then held fixed. The strain response consists of an instantaneous increase in strain at $t = 0$ followed by continued straining in time at a non-constant rate and an asymptotic approach to some limit value at time increases. The jump in strain at t=0 indicates instantaneous springiness or elasticity. Meanwhile, the fact that the material reaches a non-zero limit value of strain indicates solid behavior. Vice versa, if the strain were to increase without bound, it would indicate a fluid behavior (which is not considered here). Anyway, when there is linearity, the strain response to the step stress σ_0 is:

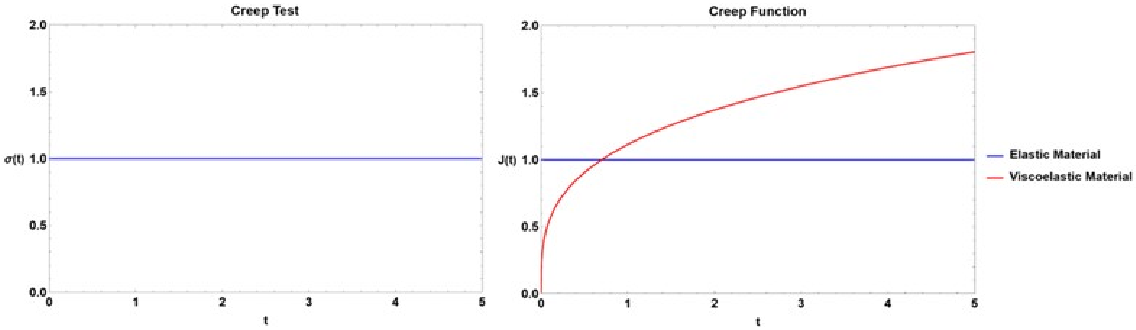

Figure 2.1: *Mechanical response during a Creep Test, comparing an elastic material (blue-line) with a viscoelastic material (red-line).*

$$\varepsilon(t) = J(t)\sigma_0 \tag{2.7}$$

Where $J(t)$ is called *Creep Compliance*. $J_0 = J(0)$ and $J_\infty = J(\infty)$ denote respectively the instantaneous elastic response and the long-time elastic response (for the limit of J(t) as $t \to \infty$).

The *Stress Relaxation Function* is the counterpart of the creep function that describes the stress response to a unit strain.

Here, let a specimen be subjected to a step strain history (as reported in *Figure 2.2*), in which the strain is instantaneously increased to some value ε_0 at $t = 0$ and then held fixed. The typical stress history consists of an instantaneous increase in stress at $t = 0$ followed by a gradual monotonic decrease of stress at a non-constant rate and an asymptotic approach to some non-zero limit value as time increases. The stress response to the step strain ε_0 is:

$$\sigma(t) = G(t)\varepsilon_0 \tag{2.8}$$

So, $G(t)$ is called the *Stress Relaxation Modulus*. It is appropriate to introduce the notation $G(0) = G_0$ and G_∞ for the limit of $G(t)$ as $t \to \infty$, because G_0 and G_∞ describe instantaneous elastic response and the long-time or equilibrium elastic response, respectively.

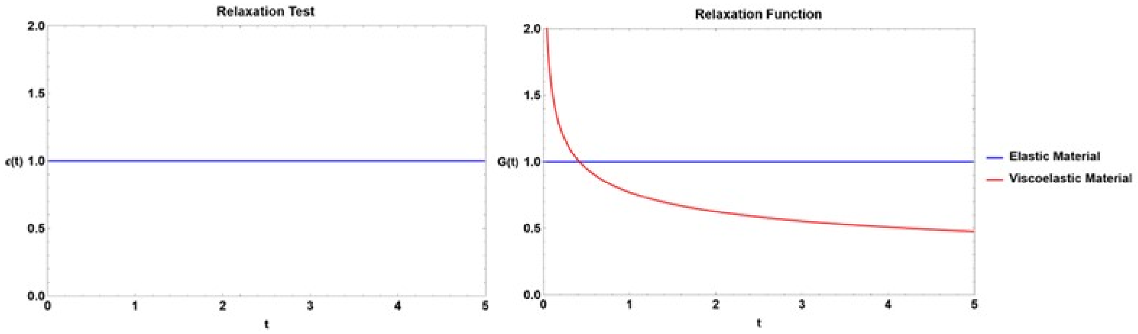

Figure 2.2: *Mechanical response during a Relaxation Test, comparing an elastic material (blue-line) with a viscoelastic material (red-line).*

Anyway, looking at *Figure 2.2*, the jump in stress at $t = 0$ is another indication of instantaneous springiness (or elasticity), while the fact that non-zero stress is required to maintain the strain at ε_0 is another indication that the material is solid. If $G(\infty; \varepsilon_0) = 0$, then no stress would be required to hold the material in a strained state, which is a characteristic of fluid response. The two functions $G(t; \varepsilon_0)$ and $J(t; \sigma_0)$ have a different dependence on time t and strain ε_0 (or stress σ_0) for each material and are therefore considered a material property, containing all information about the viscoelastic behavior. It is also useful to note that they are positive functions $\forall t > 0$, while they are zero for $t < 0$.

2.2 Linear Hereditariness of Biological Tissue

The classical models seen in the previous paragraph are unable to fully describe the viscoelastic behavior of materials. Indeed, the Creep test is well interpreted by the Kelvin-Voigt model, but it is ineffective in the Relaxation phenomenon. In contrast, the Maxwell model correctly describes Relaxation but fails for the Creep phenomenon. This involves double modeling to fully describe the behavior of the same material, which is unacceptable because the same material can't have different behavior depending on the test. In addition, the solution of these models always results in an exponential form of the response function in contrast to what Nutting discovered around 1921. Particularly, he found that the law between strain-time and force-time could be determined through a single general power law [11]. This formulation was the beginning of the research for alternative forms to express the Creep and Relaxation functions that would best describe the response of hereditary material under imposed loading or deformation. Hence *Scott-Blair* introduced the *Springpot* mathematical model, from which the formulation of the constitutive stress-strain law via fractional calculus began [12]. The use of *Fractional Differential Models* allows greater flexibility with fewer parameters, which results in considerable simplification. The flexibility of such a model is given by the fact that the derivation order can vary to obtain a constitutive law suitable for each material.

Fractional calculus is a branch of mathematical analysis that studies the different possibilities of defining real number powers or complex number powers of the differentiation operator and the integration operator. This field generalizes classical calculus by developing a calculus for such operators (refer to *Appendix* for more details about fractional calculus)[13]. It has found applications in various fields of science and engineering. It is particularly useful for studying dynamical systems, as fractional order operators are non-local and capture the history of dynamics.

Linear hereditariness is certainly the field of the most extensive applications of fractional calculus, given its ability to model hereditary phenomena with a long memory. In the framework of linear hereditariness, an important assumption in this regard is that the material response is linear. The linearity property of the response includes two conditions: scalarity and superposition. In this case, they will be used only for the stress or strain response to a strain or stress history, respectively. Consequently, if a strain history $\varepsilon(t)$ is scaled by constant α, then the corresponding stress $\sigma(t)$ is also scaled by α, or if two strain histories are superposed, then the corresponding stresses are also superposed. It is important to note that the property of linearity of response does not refer to the shape of the material response curve, but it refers to the method of constructing the stress response of a complex deformation history by scaling and superimposing the individual stress responses. So, if the load (or strain) program is more complex than a simple unit load (or strain), the material response, i.e. Eqs. (2.7) and (2.8), is transformed into a convolution integral of the previous history of stress or strain, respectively.

$$\sigma(t) = \int_0^t G(t-\tau)\dot{\varepsilon}(\tau)d\tau + \varepsilon_0 G(t) \tag{2.9a}$$

$$\varepsilon(t) = \int_0^t J(t-\tau)\dot{\sigma}(\tau)d\tau + \sigma_0 J(t) \tag{2.9b}$$

Where $\dot{\sigma} = d\sigma/dt$ and σ_0 is the value of stress at $t = 0$, similarly $\dot{\varepsilon} = d\varepsilon/dt$ and ε_0 is the value of strain at $t = 0$. Eqs. (2.9a) and (2.9b) are defined in terms of *Boltzmann's superposition principle.* There is a linear relationship between stress and strain and their time derivatives so that the strain produced by any set of applied stresses is the sum of the strains produced by the separate steps of the load history set when acting alone. In other terms, it assumes that the material has a memory of the events that affected it, so the mechanical response at a generic time is a function of all the previous history.

Additionally, the creep and relaxation functions must satisfy the reciprocity relation in the Laplace domain:

$$\hat{J}(s)\hat{G}(s) = \frac{1}{s^2} \tag{2.10}$$

s indicates the Laplace parameter and $\hat{f}(s) = \mathcal{L}[f(t)]$ is the *Laplace transform* of the generic function $f(t)$[16]. The relation (2.10) expresses the circumstance that $G(t)$ and $J(t)$ are functions related to each other in Laplace's domain. It follows that if $J(t)$ is determined through experimental evidence, the function $G(t)$ is determined accordingly, and vice versa. Moreover, in the presence of material fading memory, the relaxation matrix $G(t)$ can be obtained as a combination of creep functions relative to the uniaxial creep test.

These linearity assumptions for the creep and relaxation functions allow the introduction of material hereditariness for the unitary value of applied stress.

The basic idea of fractional-order linear hereditariness is to express the Creep and

Stress Relaxation functions as power laws of time, so that:

$$G(t) = \frac{G_0}{\Gamma(1-\beta)}\left(\frac{t}{\tau_0}\right)^{-\beta} \tag{2.11a}$$

$$J(t) = \frac{1}{G_0\Gamma(1+\beta)}\left(\frac{t}{\tau_0}\right)^{\beta} \tag{2.11b}$$

where $\Gamma(\beta)$ is the Euler-Gamma function, G_0 (the Relaxation function at the t=0) is the elastic modulus of the material, while β and τ_0 are material parameters that may be estimated through a best-fitting procedure of experimental data. Replacing (2.11a) and (2.11b) in the Boltzmann integral equations (2.9a) and (2.9b), the fractional constitutive relation between strain and stress history, and between stress and strain history become:

$$\sigma(t) = \frac{G_0\tau_0^\beta}{\Gamma(1-\beta)}\int_0^t (t-\tau)^{-\beta}\dot{\varepsilon}(\tau)d\tau = G_0\tau_0^\beta\left({}_c\mathcal{D}_{0+}^\beta\varepsilon\right)(t) \tag{2.12a}$$

$$\varepsilon(t) = \frac{1}{G_0\tau_0^\beta\Gamma(1+\beta)}\int_0^t (t-\tau)^{\beta}\dot{\sigma}(\tau)d\tau = \frac{1}{G_0\tau_0^\beta}\left(\mathcal{I}_{0+}^\beta\sigma\right)(t) \tag{2.12b}$$

Where $\left({}_c\mathcal{D}_{0+}^\beta\right)(t)$ is the *Fractional Caputo Derivative*, while $\left(\mathcal{I}_{0+}^\beta\right)(t)$ is the *Fractional Reimann-Liouville Integral* [15]. Through these generalized linear laws, it is possible to characterize the hereditary behavior of a biological tissue. As a consequence, a mathematical formulation that can be used to represent this mechanical behavior is the linear theory of material hereditariness that is nowadays described by the so-called Fractional-Order Hereditariness (FOH). In this setting, the formalism of fractional calculus, lately used in several biomechanical contexts [17, 18, 19, 20] allows replacing of the well-known constitutive equations of classical linear elasticity with their-fractional-order counterparts, involving, additional parameters the derivation order $\beta \in [0, 1]$.

2.2.1 Springpot

Springpot is a mechanical element that combines stress and strain using a fractional derivative operator. In detail, it has an intermediate behavior between an elastic solid and a Newtonian fluid. The Springpot can reduce to the elasticity of a spring on one side, and to the storage of a dashpot on the other one, as schematic represented in *Figure 2.3*.

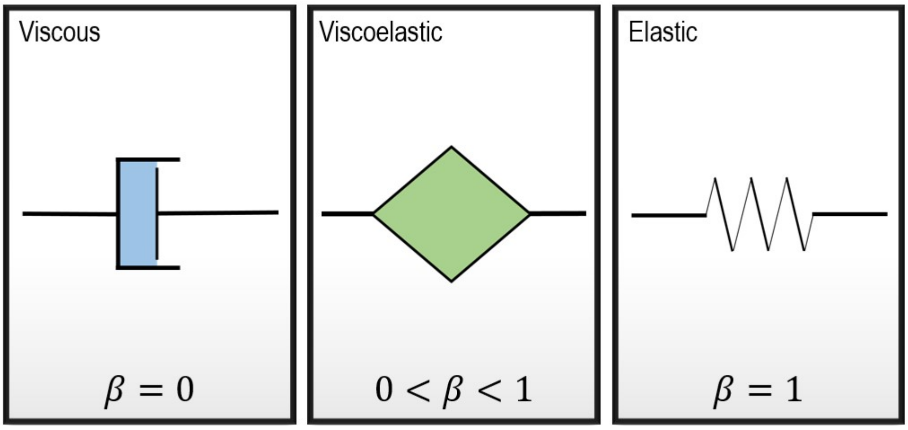

Figure 2.3: *Mathematical model of "Springpot"*

Knowing that in elastic solid, stress is proportional to the zero-order derivative of strain (*Eq.2.3*), whereas, for liquid, stress is proportional to the first-order derivative of deformation (*Eq.2.4*), then it is logical that for a viscoelastic material, the stress is proportional to the β real-order derivative, intermediate between 0 and 1 of the strain. The generalized Spring-Pot governing equation, initially proposed by Scott Blair [12], and then extended by Gerasimov and G.L. Slonimsky, is as follows:

$$\sigma(t) = C_\beta \left({}_c\mathcal{D}^{\beta}_{0^+}\varepsilon \right)(t) \quad (0 \le \beta \le 1) \tag{2.13}$$

But also

$$\varepsilon(t) = \frac{1}{C_\beta} \left(\mathcal{I}^{\beta}_{0^+}\sigma \right)(t) \quad (0 \le \beta \le 1) \tag{2.14}$$

Where β and C_β depend on the material's properties and can be obtained from a best-fitting of experimental data. Comparing Eqs.(2.13) and (2.14) with Eqs.(2.12a) and (2.12b), respectively, it can be seen that $C_\beta = G_0 \cdot \tau_0^\beta$, i.e. that C_β is a kind of fractional modulus of the material. The physical dimensions of the coefficients are $[C_\beta] = Pa \cdot s^\beta$ and $[G_0] = Pa$.
Moreover, it is possible to observe in *Figure 2.3* that:

- if $\beta = 0$, the order of fractional derivation is zero, therefore the constitutive fractional relation returns to Hooke's law (2.3), so the spring-pot reduces to the spring and coefficient C_β returns to elastic modulus E;
- if $\beta = 1$, the order of fractional derivation is one, therefore the constitutive fractional relation returns to Netwon-Petroff's law (2.4), so the spring-pot reduces to the dashpot and coefficient C_β returns to material viscosity η.

The concept of fractional derivative plays a fundamental role in the formulation of viscoelasticity, and more in detail, of hereditary behavior materials describing the mechanical response of these hybrid materials in depth.
The springpot allows classic rheological models to be generalized through fractional calculations, too. There are many formulations of different fractional rheological models, where Springpot is connected in series or parallel to Maxwell's model, Kelvin-Voigt's model, or Zener's model, and so on[21]. However, as the number

of connected components increases, the number of parameters also increases, making the governing equation complex.
These models are certainly better than the classical ones because they manage to qualitatively describe the Creep and Stress Relaxation curves well, at least as far as linear fractional viscoelasticity is concerned. Indeed, the only problem with the use of the springpot is the lack of complete physical interpretation.

2.3 Three-axial constitutive equations

Relations (2.12a) and (2.12b) are expressed in mono-dimensional form. Their extension to the more general case of three axial isotropic materials is shortly discussed in this section. The three-axial state of stress in *Fractional Hereditary Materials* (FHM) is described by the 2^{nd} order stress tensor σ with component σ_{ij} which presents the symmetries $\sigma_{ij} = \sigma_{ji}$ for $i \neq j$ and $i, j = x, y, z$. In the same way, the state of strain is described, by the 2^{nd} order small strain tensor ε. Particularly, the six-component stress and strain vectors are, respectively:

$$\sigma^{\mathbf{T}}(\mathbf{t}) = [\sigma_{xx}(t)\,\sigma_{yy}(t)\,\sigma_{zz}(t)\,\tau_{yz}(t)\,\tau_{xz}(t)\,\tau_{xy}(t)] \tag{2.15a}$$

$$\varepsilon^{\mathbf{T}}(\mathbf{t}) = [\varepsilon_{xx}(t)\,\varepsilon_{yy}(t)\,\varepsilon_{zz}(t)\,\varepsilon_{yz}(t)\,\varepsilon_{xz}(t)\,\varepsilon_{xy}(t)] \tag{2.15b}$$

where t is the current time, while $\sigma_{ij}(t)$ and $\varepsilon_{ij}(t)$ are the mixed index stress and strain components, namely $i \neq j$ denote shear stress and strain, respectively. A schematic representation of these stresses against a generic cubic element is shown in *Figure 2.4*.

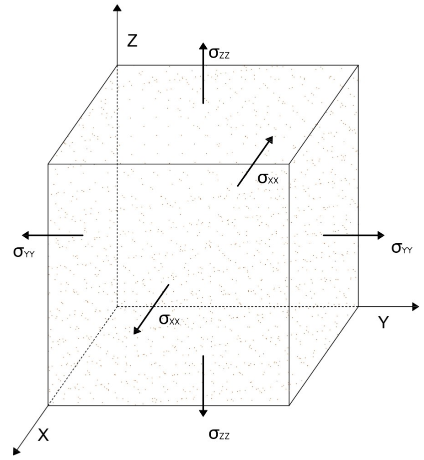

Figure 2.4: *Schematic representation of a cubic element where the black arrows represent normal stresses related to each surface.*

Let us assume that $\sigma_{ij}(t) = \sigma_{ij}(t)\delta_{ij}$, where δ_{ij} is the well-known Kronecker symbol that is $\delta_{ij} = 0$ when $i \neq j$ and $\delta_{ij} = 1$ for $i = j$; consequently, a single normal stress is $\sigma_{ii} = 1$ for $(i = x, y, z)$.

In this context, the evolution of the strain $\varepsilon_{ij}\left(t\right)$ both along the stress direction $\sigma_{ii}\left(t\right)$ and in the orthogonal planes reads:

$$\varepsilon_{ii}\left(t\right) = J_L\left(t\right)\sigma_{ii} = J_L\left(t\right) \tag{2.16a}$$

$$\varepsilon_{kk}\left(t\right) = \varepsilon_{jj}\left(t\right) = -J_v\left(t\right)\sigma_{ii} = -J_v\left(t\right) \tag{2.16b}$$

with $i \neq j \neq k$ and $i,\, j,\, k \,=\, x, y, z$. In Eqs.(2.16a) $J_L\left(t\right)$ and $J_v\left(t\right)$ are the axial and the transverse creep functions concerning the stress direction, respectively. Under the assumption of smooth load process $\sigma_{ij}(t)$ with $i = x, y, z$, the presence of simultaneous stresses can be excused by the integral:

$$\varepsilon_{ii}\left(t\right) = \int_0^t J_L\left(t-\sigma\right)\dot{\sigma}_{ii}\left(\sigma\right) - J_v\left(t-\sigma\right)\left[\dot{\sigma}_{jj}\left(\sigma\right) + \dot{\sigma}_{kk}\left(\sigma\right)\right]d\sigma \tag{2.17}$$

In the context of isotropic material , shear strains $2\varepsilon_{ij}(t)$ are not involved by the axial stress $\sigma_{ii}\left(t\right)$, but only by the shear stress as $\sigma_{ij}(t)$ with $i \neq j$. The evolution of the shear strain $2\varepsilon_{ij}(t)$ due to a generic shear stress history $\sigma_{ij}(t)$ may be obtained by superposition integrals using the shear creep function $J_T(t)$ as:

$$2\varepsilon_{ij}\left(t\right) = \int_0^t J_T\left(t-\sigma\right)\dot{\sigma}_{ij}\left(\sigma\right)d\sigma \tag{2.18}$$

with $i \neq j$ and $i, j = x, y, z$. The constitutive equations reported in Eqs.(2.17),(2.18) may be reported in Voigt notation as:

$$\varepsilon\left(t\right) = \int_0^t \mathbf{J}\left(t-\sigma\right)\dot{\sigma}\left(\sigma\right)d\sigma \tag{2.19}$$

where $\mathbf{J}(t)$ is the creep functions matrix that is described as:

$$\mathbf{J}\left(t\right) = \left[\begin{array}{cc} \mathbf{J}^{(A)}\left(t\right) & \mathbf{0} \\ \mathbf{0} & \mathbf{J}^{(T)}\left(t\right) \end{array}\right] \tag{2.20}$$

$\mathbf{J}^{(A)}(t)$ includes the elements of the axial creep matrix, i.e. :

$$J_{ij}^{(A)}\left(t\right) = J_L\left(t\right)\delta_{ij} - \left(1-\delta_{ij}\right)J_v\left(t\right) \tag{2.21}$$

While $\mathbf{J}^{(T)}(t)$ is the shear creep matrix, which is a diagonal matrix gathering the shear creep functions $J_T\left(t\right)$ as:

$$J_{ij}^{(T)}\left(t\right) = J_T\left(t\right)\delta_{ij} \tag{2.22}$$

Particularly, the three creep functions $J_L(t)$, $J_v(t)$ and $J_T(t)$ are related by a linear relation that reads [22]:

$$J_T(t) = 2J_L(t) - J_v(t) \tag{2.23}$$

that may be obtained, with straightforward manipulations, by introducing a shear stress state $\sigma_{ij}(t)$ that involves a shear strain state under the isotropic assumption, namely $\gamma_{ij} = 2\varepsilon_{ij}(t)$, and as evaluating the elongation and the stress along the principal axes at angles of 90°.

Under the assumption of linear elasticity, the creep functions coincide with the material compliance, which reads $J_T = 1/G$,$J_L = 1/E$ and J_v/E. After substitution in Eq. (2.23), this yields:

$$\frac{1}{G} = 2\left(\frac{1}{E} + \frac{v}{E}\right) = \frac{2(1+v)}{E} \tag{2.24}$$

that is the well-known relation among elasticity moduli.
In addition, creep function matrix $\mathbf{J}(t)$ in Eq.(2.20) is related to the definition of the relaxation matrix $\mathbf{G}(t)$ by means of the coniugation relation as:

$$\hat{\mathbf{G}}(s)\hat{\mathbf{J}}(s) = \frac{1}{s^2}\mathbf{I} \tag{2.25}$$

where $\mathbf{I}$ is the identity matrix, while $\hat{\mathbf{G}}(s)$ and $\hat{\mathbf{J}}(s)$ are the Laplace transforms of the relaxation $\mathbf{G}(t)$ and creep $\mathbf{J}(t)$ functions matrices, respectively.
With straightforward manipulations of Eq.(2.25), the relaxation matrix may be written as:

$$\mathbf{G}\left(t\right) = \begin{bmatrix} \mathbf{G}^{(A)}\left(t\right) & \mathbf{0} \\ \mathbf{0} & \mathbf{G}^{(T)}\left(t\right) \end{bmatrix} \tag{2.26}$$

where:

$$G_{ij}^{(A)}\left(t\right) = \mathcal{L}^{-1}\left[\frac{1}{s^2\left(\hat{J}_L + \hat{J}_v\right)\left(\hat{J}_L - 2\hat{J}_v\right)}\right]\left[\left(\hat{J}_L - \hat{J}_v\right)\delta_{ij} + \left(1-\delta_{ij}\right)\hat{J}_v\right] \tag{2.27a}$$

$$G_{ij}^{(T)}\left(t\right) = \mathcal{L}^{-1}\left[\frac{1}{s^2\left(\hat{J}_L + \hat{J}_v\right)}\right]\delta_{ij} \tag{2.27b}$$

Similarly to the previous case, $\mathbf{G}^{(A)}(t)$ includes the elements of the axial relaxation matrix, while $\mathbf{G}^{(T)}(t)$ is the shear relaxation matrix, which is a diagonal matrix gathering the shear relaxation functions, i.e:

$$G_{ij}^{(A)}\left(t\right) = G_L\left(t\right)\delta_{ij} - \left(1-\delta_{ij}\right)G_v\left(t\right) \tag{2.28a}$$

$$G_{ij}^{(T)}\left(t\right) = G_T\left(t\right)\delta_{ij} \tag{2.28b}$$

The torsional, longitudinal and transverse relaxation functions $G_T(t)$,$G_L(t)$ and $G_v(t)$ are linearly related by an equation that is similar to the one involving creep functions in Eq.(2.23), reading [12]:

$$G_v\left(t\right) = G_L\left(t\right) - 2G_T\left(t\right) \tag{2.29}$$

Consequently, the stress vector can be evaluated using Boltzmann's superposition principle as:

$$\sigma\left(t\right) = \int_0^t \mathbf{G}\left(t-\sigma\right)\dot{\varepsilon}\left(\sigma\right)d\sigma \tag{2.30}$$

Introducing the power-law representation of the *Relaxation Matrix Functions* $\mathbf{G}\left(t\right)$ into Eq.(2.30), ans substituting C_β with G_β, results in:

$$\mathbf{G}\left(t\right) = \mathbf{G}_\beta\frac{t^{-\beta}}{\Gamma\left(1-\beta\right)} + \bar{\mathbf{G}} \tag{2.31}$$

with the coefficient matrices:

$$\mathbf{G}_\beta = \begin{bmatrix} G_\beta^L & G_\beta^v & G_\beta^v & 0 & 0 & 0 \\ G_\beta^v & G_\beta^L & G_\beta^v & 0 & 0 & 0 \\ G_\beta^v & G_\beta^v & G_\beta^L & 0 & 0 & 0 \\ 0 & 0 & 0 & G_\beta^T & 0 & 0 \\ 0 & 0 & 0 & 0 & G_\beta^T & 0 \\ 0 & 0 & 0 & 0 & 0 & G_\beta^T \end{bmatrix} \tag{2.32a}$$

$$\overline{\mathbf{G}} = \begin{bmatrix} \bar{G}_L & \bar{G}_v & \bar{G}_v & 0 & 0 & 0 \\ \bar{G}_v & \bar{G}_L & \bar{G}_v & 0 & 0 & 0 \\ \bar{G}_v & \bar{G}_v & \bar{G}_L & 0 & 0 & 0 \\ 0 & 0 & 0 & \bar{G}_T & 0 & 0 \\ 0 & 0 & 0 & 0 & \bar{G}_T & 0 \\ 0 & 0 & 0 & 0 & 0 & \bar{G}_T \end{bmatrix} \tag{2.32b}$$

It yields a relation among the stress vector and the history of the strain vector, as:

$$\sigma\left(t\right) = \mathbf{G}_\beta \int_0^t \left(t-\tau\right)^{-\beta} \dot{\varepsilon}\left(\tau\right) d\tau + \bar{\mathbf{G}} = \mathbf{G}_\beta \left(\mathcal{D}_{0^+}^{\beta} \varepsilon\right)\left(t\right) + \bar{\mathbf{G}} \tag{2.33}$$

Eq.(2.33) is the generalization of the constitutive equation reported in Eq.(2.13) under the assumption of isotropic material hereditariness.
Moreover, if $\bar{\mathbf{G}} = \mathbf{0}$, the inverse constitutive equation corresponding to Eq.(2.33) is obtained:

$$\varepsilon\left(t\right) = \mathbf{J}_\beta \int_0^t \left(t-\tau\right)^{\beta-1} \dot{\sigma}\left(\tau\right) d\tau = \mathbf{J}_\beta \left(\mathcal{I}_{0^+}^{\beta} \sigma\right)\left(t\right) \tag{2.34}$$

where $\mathbf{J}_\beta = \mathbf{G}_\beta^{-1}$ is the *Creep Matrix Function*s and plays the same role as the compliance matrix in linear elasticity theory. More specifically, It is defined as:

$$\mathbf{J}_\beta = \begin{bmatrix} J_\beta^L & J_\beta^\nu & J_\beta^\nu & 0 & 0 & 0 \\ J_\beta^\nu & J_\beta^L & J_\beta^\nu & 0 & 0 & 0 \\ J_\beta^\nu & J_\beta^\nu & J_\beta^L & 0 & 0 & 0 \\ 0 & 0 & 0 & J_\beta^T & 0 & 0 \\ 0 & 0 & 0 & 0 & J_\beta^T & 0 \\ 0 & 0 & 0 & 0 & 0 & J_\beta^T \end{bmatrix} \tag{2.35}$$

Hence, the constitutive equations for a three-axial state are found as well as moduli and coefficients that are necessary to describe the mechanical response for an isotropic hereditary material.

Bibliography

[1] Gioacchino Alotta, M. D. P. Fractional viscoelasticity under combined stress and temperature variations. **2019**. doi:10.1007/978-3-030-41057-5.

[2] Bologna E., Di Paola M., Dayal K., Deseri L. & Zingales, M. Fractional-order nonlinear hereditariness of tendons and ligaments of the human knee: FOH for fibrous tissues.*Philos. Trans. R. Soc. A Math. Phys. Eng. Sci* . 378, **2020**.

[3] Bologna E., Zingales M., Alotta G. & Deseri L. Quasi-Fractional Models of Human Tendons Hereditariness. *IEEE 4th Int. Forum Res. Technol. Soc. Ind. RTSI 2018 - Proc.* **2018** doi:10.1109/RTSI.2018.8548419.

[4] Yohan P. & Jacques O. Biomechanics of Living Organs. **2017**. doi:10.1016/c2015-0-00832-2.

[5] Deseri L., Di Paola, M., Zingales, M. & Polacci, P. Power-law hereditariness of hierarchical fractal bones. *International Journal for Numerical Methods in Engineering* vol. 29 1338–1360 **2016**.

[6] Sciortino V., Cerniglia, D., Pasta, S., & Ingrassia, T. Fractional Calculus as a New Perspective in the Viscoelastic Behaviour of the Intervertebral Disc. *European Workshop on Structural Health Monitoring* (pp. 915-925), **2022**.

[7] Mino G. Di et al. Linear and nonlinear fractional hereditary constitutive laws of asphalt mixtures.*Journal of Civil Engineering and Management* 22, 882–889 **2016**.

[8] Di Paola, M. & Granata, M. F. Fractional model of concrete hereditary viscoelastic behavior.*Arch. Appl. Mech.* 87, 335–348 **2017**.

[9] Capurso M. Lezioni di Scienza Delle Costruzioni. 1–304 **2006**.

[10] Carpinteri A. Scienza delle Costruzioni Vol 2. pp 333-384 **1992**.

[11] Nutting P. G. A new general law of deformation. *J. Franklin Inst.* 191, 679–685 **1921**.

[12] Blair G. W. S. & Caffyn, J. E. VI. An application of the theory of quasi-properties to the treatment of anomalous strain-stress relations.*London, Edinburgh, Dublin Philos. Mag. J. Sci.* 40, 80–94 **1949**.

[13] Zhmakin A. I. A Compact Introduction to Fractional Calculus. **2022**

[14] Mainardi F. Fractional calculus: Theory and applications. *Mathematics* 6, **2018**.

[15] Di Paola M, Pinnola FP. "Calcolo frazionario & viscoelasticità". Published online **2011**.

[16] Podlubny I. Fractional Differential Equations. **1999**.

[17] Zingales M., "An exact thermodynamical model of power-law temperature time scaling".*Annals of Physics.* (N. Y). 365, 24–37,**2016**.

[18] Caputo M., Cametti C. "Fractional derivatives in the diffusion process in heterogeneous systems: The case of transdermal patches". *Mathematical Biosciences.* 291, 38–45, **2017**.

[19] Di Paola M., Pirrotta A., Valenza A., "Visco-elastic behavior through fractional calculus: an easier method for best fitting experimental results",*Mech. Mater.*, vol. 43 (12). 799–806, **2011**.

[20] Ionescu C., Lopes A., Copot D., Machado J. A. T., Bates J. H. T. "The role of fractional calculus in modeling biological phenomena: A review".*Communications in Nonlinear Science and Numerical Simulation.* 51, 141–159,**2017**.

[21] Sandev, T. & Tomovski, Ž. "Fractional Equations and Models". *Developments in Mathematics* vol. 61, **2019**.

[22] Bologna E., Graziano F., Deseri L., Zingales M., “Power-Laws heredinariness of biomimetic ceramics for cranioplasty", *International Journal of Non-Linear Mechanics*, vol. 115, pp. 61-67, **2019**.

Chapter. 3

A Generalized Theory of Poromechanics

Poromechanics is a branch of physics, and specifically continuum mechanics, that studies the behavior of a biphasic continuum comprising an elastic porous matrix with an infiltrating pore fluid. Generally, a porous medium or a porous material is composed of a solid (often called matrix) permeated by an interconnected network of voids (pores), through which there is the presence and movement of a fluid (liquid or gas). Rocks, soil, and biological tissues are examples of porous materials. Porous media whose solid matrix is elastic and the fluid is viscous are called poroelastic, so *Poroelasticity* is the elastic theory of the mechanical behavior of porous materials.
The presence of fluid free to move in a porous medium changes its mechanical response. The key mechanisms of matrix-fluid interaction are such that: (i) an increase in pore pressure induces an expansion of the solid matrix and (ii) compression of the matrix, in turn, causes an increase in pore pressure if the fluid is prevented from escaping from the porous material. The combination of the two mechanisms gives the mechanical properties of the solid matrix an apparent time dependence. The increase in pore pressure due to compression dissipates if diffusion transport of the fluid mass is allowed; in this case, further deformation of the solid matrix takes place. The first theory that considered the influence of fluid in the pores of soil under quasi-static deformation conditions was developed in 1923 by *Karl von Terzaghi*, who proposed a one-dimensional model for soil consolidation. His theory was generalized to the three-dimensional case by *Rendulic*, in 1936. However, It was not until 1961 that *Maurice Anthony Biot* developed a linear poroelastic theory consistent with the two basic mechanisms commented on above [1]; here, the volumetric deformation of the solid matrix leads to the fluid flowing into the material. On the other hand, fluid forced into the material causes matrix deformation. So, fluid-saturated porous solids, for example, polymer foams, metal foams, sponges, or biological tissues can be described by a two-phase model.[2]

However, these equations do not enable us to describe the behavior of those materials that have a history of deformation or interaction between matrix and fluid, such as biological tissues. This problem has already been addressed in the literature in several ways, such as modifying Fick and/or Darcy transport equations using fractional calculus to introduce the memory effect induced by the interaction of fluid particles and pore structure of the elastic medium [3, 4, 5, 6]. In other studies, a power-law variation of the geometric and physical properties of the porous medium was considered, leading to a fractional-order relationship between incoming flow and pressure applied to the control section [7, 8].

The common base of the aforementioned approaches is represented by the linear elastic behavior of the tissue. However, it is well-known, as discussed in *Chapter 2*, that in biological tissue the stress depends on the history of strain and not only on the actual value of the strain [9, 10, 11]. This effect is known as *material hereditariness* and it is usually represented by coupling linear elastic spring and linear viscous dashpot, i.e. the spring-pot [12, 13, 14, 15, 16, 17].

This paper considers a fluid-saturated solid with materially incompressible constituents. The incompressibility of a constituent (or material incompressibility) implies an incompressibility in the micro-range of the material, which does not lead to macroscopic ones. Even if the realistic density of a constituent is constant, the partial density can still change through changes in the volume fraction. Therefore, the so-called point of compaction exists. This deformation state is reached when all pores are closed and further volume deformations are impossible due to the incompressibility constraint of the solid skeleton material. Fluid viscosity is taken into account by the drag force, where the permeability is independent of the actual porosity of the solid skeleton. Concerning the numerical treatment of the volumetric coupled solid-fluid problem, incompressibility of both constituents leads to a system of *differential equations* in the time domain. This differential equation system must be handled by an appropriate time integration scheme. The spatial discretization is carried out by numerical method. Firstly, the classical theory of poroelasticity is described in *Section 3.1*, and then the model proposed will be discussed in *Section 3.2*. Particularly, the fractional-order hereditariness model was used to describe the mechanical behavior of fibrous tissue through a three-axial model. The use of Boltzmann superposition (see *Section 2.2*) allows to formulate the constitutive model of the material in terms of Caputos' fractional derivative [18] so that the coupling effect within the pore pressure field yields a fully coupled theory of poromechanics involving fractional-order hereditariness. Finally, a numerical example has been discussed, involving a confined compression test in a semi-drained condition (*Section 3.3.1*) and a fully drained test (*Section 3.3.2*) to exploit the constitutive relation of the investigated model.

3.1 Classical Constitutive Equation

In engineering practice, it is well known that when a load is applied to such a structure, the porous solid does not assume an instantaneous deflection, but gradually settles at a variable rate, depending on the speed at which the water is squeezed out of the voids. To study this settlement, consider a *Representative Volume Elements* (RVE) of the biological tissue, i.e. the smaller volume that contains elements of solids and pores filled by the fluid phase involved in poromechanics (shown in *Figure 3.1*). This element is sufficiently large about the size of the pores so that it can be treated as homogeneous, and at the same time sufficiently small concerning the scale of macroscopic phenomena so that it can be considered infinitesimal in mathematical treatment.

RVE contains at the same time the two phases that only interact under conditions

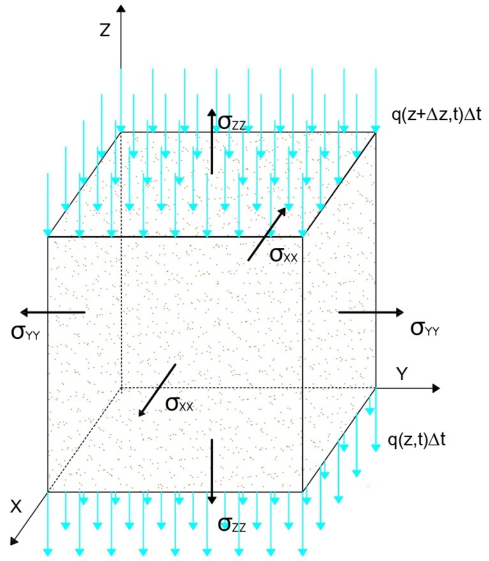

Figure 3.1: *Schematic RVE where the blue arrows represent fluid flow across the cubic element surfaces, while the black arrows represent normal stresses to each surface.*

of forces equilibrium (Eq.3.1) and undergo the same deformation.

$$\begin{cases} \frac{\partial \sigma_{xx}}{\partial x} + \frac{\partial \tau_{xy}}{\partial y} + \frac{\partial \tau_{xz}}{\partial z} & = 0 \\ \frac{\partial \tau_{yx}}{\partial x} + \frac{\partial \sigma_{yy}}{\partial y} + \frac{\partial \tau_{yz}}{\partial z} & = 0 \\ \frac{\partial \tau_{zx}}{\partial x} + \frac{\partial \tau_{zy}}{\partial y} + \frac{\partial \sigma_{zz}}{\partial z} & = 0 \end{cases} \tag{3.1}$$

Denoting by u, v, w the components of the displacement of the soil and assuming the strain to be small, the values of the strain components are [19, 20]:

$$\begin{cases} \varepsilon_{xx} = \frac{\partial u}{\partial x}; & \gamma_{yz} = \frac{\partial w}{\partial y} + \frac{\partial v}{\partial z} \\ \varepsilon_{yy} = \frac{\partial v}{\partial y}; & \gamma_{xz} = \frac{\partial w}{\partial x} + \frac{\partial u}{\partial z} \\ \varepsilon_{zz} = \frac{\partial w}{\partial z}; & \gamma_{xy} = \frac{\partial v}{\partial x} + \frac{\partial u}{\partial y} \end{cases} \tag{3.2}$$

In physical terms, this stress can be divided into two parts: one due to the hydrostatic pressure of the water filling the pores, and the other due to the average stress in the pores. Consequently, the constitutive equations of poromechanics require, the addition of a hydrostatic stress field ($\mathbf{p}$) to the six relationships between the six components of the stress vector (σ) and the six components of the strain vector (ε) in Voigt's representation, without spatial dependence, which represents the pressure variation in the fluid phase, as reported in the following systems of equations:

$$\begin{cases} \varepsilon_{xx} &= \frac{\sigma_{xx}}{E} - \frac{\nu}{E}(\sigma_{yy} + \sigma_{zz}) + \frac{p}{3H} \\ \varepsilon_{yy} &= \frac{\sigma_{yy}}{E} - \frac{\nu}{E}(\sigma_{xx} + \sigma_{zz}) + \frac{p}{3H} \\ \varepsilon_{zz} &= \frac{\sigma_{zz}}{E} - \frac{\nu}{E}(\sigma_{xx} + \sigma_{yy}) + \frac{p}{3H} \\ \gamma_{xy} &= \frac{\tau_{xy}}{G} \\ \gamma_{xz} &= \frac{\tau_{xz}}{G} \\ \gamma_{yz} &= \frac{\tau_{yz}}{G} \end{cases} \tag{3.3}$$

where H is the *Bulk modulus* for fluid variation pressure[1].In this relation, G and ν are *Shear Modulus* and *Poisson's coefficient*, respectively; which are related to Young's Modulus E by:

$$G = \frac{E}{2(1+\nu)} \tag{3.4}$$

The increase in water pressure p cannot produce any shearing strain because of the assumed isotropic material; so its effect must be the same on all three components of strain.

Thereafter, to fully describe the macroscopic state of the RVE, it's necessary to consider an additional variable that indicates the amount of water in the pores. $\xi(t)$ denotes the increase in the volume of water per unit volume of soil, consequently, the variation of water content can be expressed as:

$$\xi(t) = \frac{1}{3H}(\sigma_{xx} + \sigma_{yy} + \sigma_{zz}) + \frac{p}{R} \tag{3.5}$$

Where R is a physical constant, too [1].

In the first approximation, *Equations 3.3* and 3.5 are the fundamental relations that completely describe the properties of the material for strain and water content under equilibrium conditions. However, it is convenient to express stress as a function of strain and fluid pressure, namely:

$$\begin{cases} \sigma_{xx} &= 2G(\varepsilon_{xx} + s\theta_I) - ap \\ \sigma_{yy} &= 2G(\varepsilon_{yy} + s\theta_I) - ap \\ \sigma_{zz} &= 2G(\varepsilon_{zz} + s\theta_I) - ap \\ \tau_{yz} &= G\gamma_{yz} \\ \tau_{xz} &= G\gamma_{xz} \\ \tau_{xy} &= G\gamma_{xy} \end{cases} \tag{3.6}$$

With two specific coefficients:

$$s = \frac{\nu}{1-2\nu}; \quad a = \frac{2(1+\nu)G}{3(1-2\nu)H}; \tag{3.7}$$

Whereas, θ_I represents the volume increase of the solid per initial volume unit, namely the *linear strain invariant*: $\theta_I = \varepsilon_{xx} + \varepsilon_{yy} + \varepsilon_{zz}$. Although, substituting

Eq.(3.6) into *Eq.*(3.5), increase in fluid content ξ becomes:

$$\xi(t) = a\left[\theta_I - \frac{p}{H}\right] + \frac{p}{R} \tag{3.8}$$

Its derivative to time is:

$$\dot{\xi}(t) = a\left[\frac{\partial \theta_I}{\partial t} - \frac{1}{H}\frac{\partial p}{\partial t}\right] + \frac{1}{R}\frac{\partial p}{\partial t} \tag{3.9}$$

Additionally, *Darcy's law*, which governs water flow in the porous medium, has been introduced to complete the system:

$$\mathbf{q} = -\frac{k}{\mu}\nabla p \tag{3.10}$$

Where $\mathbf{q}$ is the vector of specific volume flux across a generic cross-section, k is the Darcy *permeability coefficient* depending on the material $[m^2]$ and μ is the *dynamic fluid viscosity* $[kg \cdot m^{-1} \cdot s^{-1}]$. Besides, assuming that water is incompressible, the water content rate of the solid must be equal to the volume of water entering per second through the surface of the element, so:

$$\dot{\xi}(t) = -\nabla \cdot \mathbf{q} \tag{3.11}$$

Combining the last two equations:

$$\dot{\xi}(t) = \frac{k}{\mu}\nabla^{\mathbf{2}}\mathbf{p} \tag{3.12}$$

and substituting *Eq.*(3.12) into *Eq.*(3.9), the constitutive equation for an isotropic elastic porous medium becomes:

$$\left[\frac{1}{R} - \frac{a}{H}\right]\frac{\partial p}{\partial t} - a\frac{\partial \theta_I}{\partial t} = \frac{k}{\mu}\nabla^2 p \tag{3.13}$$

It is the equation of *Classical Theory of Poroelasticity* for a three-axial geometry [1].

3.2 Fractional Poro-viscoelasticity

The three-axial hereditariness presented in *Section 2.2* allows for the introduction of the effects of the presence of fractional operator into the system of equations 3.3.

So that,

$$\begin{cases} \varepsilon_{xx} &= J_\beta^L \; {}_0\mathcal{I}_t^\beta \left(\sigma_{xx} - J_\beta^\nu(\sigma_{yy} + \sigma_{zz})\right) + \dfrac{p}{3H} \\ \varepsilon_{yy} &= J_\beta^L \; {}_0\mathcal{I}_t^\beta \left(\sigma_{yy} - J_\beta^\nu(\sigma_{xx} + \sigma_{zz})\right) + \dfrac{p}{3H} \\ \varepsilon_{zz} &= J_\beta^L \; {}_0\mathcal{I}_t^\beta \left(\sigma_{zz} - J_\beta^\nu(\sigma_{yy} + \sigma_{xx})\right) + \dfrac{p}{3H} \\ \gamma_{yz} &= J_\beta^T \; {}_0\mathcal{I}_t^\beta \tau_{yz} \\ \gamma_{xz} &= J_\beta^T \; {}_0\mathcal{I}_t^\beta \tau_{xz} \\ \gamma_{xy} &= J_\beta^T \; {}_0\mathcal{I}_t^\beta \tau_{xy} \end{cases} \tag{3.14}$$

where H is the bulk modulus for fluid variation pressure expressed in *Section 3.1*, while $J_\beta^L, J_\beta^\nu, J_\beta^T$ are the axial, transverse and torsional component of the *Creep Matrix Functions* ($\mathbf{J}_\beta$) defined as *Eq.*(2.35). Furthermore, system equations (3.14) can also be written in matrix form, as:

$$\varepsilon = \mathbf{J}_\beta \left({}_0\mathcal{I}_t^\beta \sigma\right) + \frac{1}{3H}\mathbf{p} \tag{3.15}$$

where ε and σ are the well-known strain and stress vectors of the solid, respectively. While, $\mathbf{p}$ is the fluid pressure field vector, defined as $\mathbf{p}^T = p\begin{bmatrix}1 & 1 & 1 & 0 & 0 & 0\end{bmatrix}$. However, it is convenient to express stress as a function of strain and fluid pressure, namely:

$$\sigma = {}_c\mathcal{D}_t^\beta \left[\mathbf{G}_\beta \left(\varepsilon - \frac{1}{3H}\mathbf{p}\right)\right] \tag{3.16}$$

Where $\mathbf{G}_\beta$ is the *Relaxation Matrix Functions* reported in *Eq.*(2.32a).
The overall stress components in the saturated FHM may then be referred to as the strain components and the fluid pressure as:

$$\begin{cases} \sigma_{xx} &= 2G_\beta^T \; {}_c\mathcal{D}_t^\beta(\varepsilon_{xx} + r\theta_I) - \alpha \; {}_c\mathcal{D}_t^\beta p \\ \sigma_{yy} &= 2G_\beta^T \; {}_c\mathcal{D}_t^\beta(\varepsilon_{yy} + r\theta_I) - \alpha \; {}_c\mathcal{D}_t^\beta p \\ \sigma_{zz} &= 2G_\beta^T \; {}_c\mathcal{D}_t^\beta(\varepsilon_{zz} + r\theta_I) - \alpha \; {}_c\mathcal{D}_t^\beta p \\ \tau_{yz} &= G_\beta^T \; {}_c\mathcal{D}_t^\beta \gamma_{yz} \\ \tau_{xz} &= G_\beta^T \; {}_c\mathcal{D}_t^\beta \gamma_{xz} \\ \tau_{xy} &= G_\beta^T \; {}_c\mathcal{D}_t^\beta \gamma_{xy} \end{cases} \tag{3.17}$$

With two specific coefficients:

$$r = \frac{G_\beta^\nu}{2G_\beta^T}; \quad \alpha = \frac{2G_\beta^T + 3G_\beta^\nu}{3H}; \tag{3.18}$$

Although, substituting *Eq.*(3.17) into *Eq.*(3.5), increase in fluid content $\xi(t)$ becomes:

$$\xi(t) = \alpha \; {}_c\mathcal{D}_t^\beta \left[\theta_I - \frac{p}{H}\right] + \frac{p}{R} \tag{3.19}$$

Its derivative is:

$$\dot{\xi}(t) = \alpha \ {}_c\mathcal{D}_t^{\beta+1} \left[\theta_I - \frac{p}{H}\right] + \frac{1}{R}\frac{\partial p}{\partial t} \tag{3.20}$$

Substituting *Eq.*(3.20) into *Eq.*(3.12), according to Darcy's law (3.10), the water content rate of the solid must be equal to the volume of water entering per second through the surface of the element. Thus, the constitutive equation for an isotropic viscoelastic hereditary porous medium becomes:

$$\alpha \ {}_c\mathcal{D}_t^{\beta+1} \left[\theta_I - \frac{p}{H}\right] + \frac{1}{R}\frac{\partial p}{\partial t} = \frac{k}{\mu}\nabla^{\mathbf{2}}\mathbf{p} \tag{3.21}$$

For the particular case of $\beta = 0$, the porous medium has an elastic behaviour, so *Eq.*(3.21) is equals to the classical poroelasticity equation, i.e. *Eq.*(3.13).
Eq.(3.21) was used to describe the settling phenomenon that occurs in a porous FHM medium under permanent static conditions in *Section 3.3* and under varying load in *Section 3.4*.

3.3 Poromechanics Of a Cylindrical FHM under constant load

Let us consider a symmetric cylinder to describe the settling phenomenon in poromechanics problem, as shown in *Figure 3.3*, that allows for the reduction of the kinematic field represented by the components of the displacement vector along a cylindrical reference system, namely: $u_r\,(r,\theta,z,t)$, $u_\theta\,(r,\theta,z,t)$ and $u_z\,(r,\theta,z,t)$ to just a one-dimensional component. Indeed for this case, $u_r = u_\theta = 0$ everywhere and $u_z\,(r,\theta,z,t) = w\,(z,t)$. The specimen is loaded by a constant and uniform pressure $\bar{\sigma}$ along the free surface of the cylinder ($z = h$) and we denote the fluid pressure field as $p\,(z,t)$. Under those circumstances, the kinematic restrictions (3.2) associated to the problem reads:

$$\begin{cases} \varepsilon_{zz} = \dfrac{\partial w\,(z,t)}{\partial z} \\ \varepsilon_{rr} = \varepsilon_{\theta\theta} = 0 \end{cases} \tag{3.22}$$

Both displacement ω and the water pressure p will depend only on the coordinate z and the time t. So that, the first-invariant reads: $\theta_I = \varepsilon_{zz}$.
The first example handles a fluid-saturated porous tube, where the upper boundary is perfectly drained and loaded by a time-dependent external force. The other boundaries are rigid and undrained (see *Figure 3.3*).
In this section, we don't consider specific *Boundary Conditions* (BD) at the bottom of the specimen (for $z = 0$), which will be provided for two cases of semi-drained and fully drained cases in *Sections 3.3.1* and *3.3.2*, respectively. The flow across the bottom vanishes in one of the two cases ($q(z,t) = 0$ for $z = 0$), whereas vanishing over-pressure is observed at the top bottom in both cases $p(z,t) = 0$ for $z = h$.

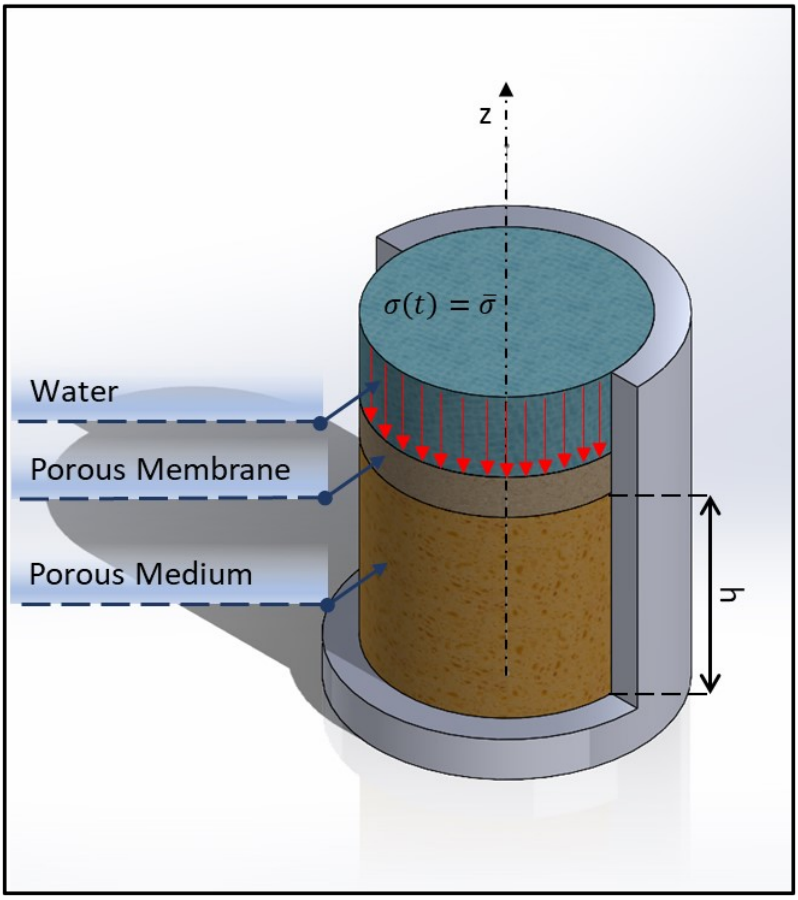

Figure 3.2: *Scheme of confined compression problem of a porous cylindrical material on which a constant pressure is imposed by a porous membrane.*

In the following, simplified notation will be used introducing a z-axis positive downward, with the same origin and, therefore the vertical stress field will be denoted as $\sigma_{zz}(z,t) = -\bar{\sigma}$. So that,

$$\frac{\partial p(z,t)}{\partial z} = 0 \quad for\ z = 0 \tag{3.23}$$

Consequently, differential fluid Eq.(3.21) becomes:

$$\alpha\ {}_c\mathcal{D}_t^{\beta+1}\left[\frac{\partial w(z,t)}{\partial z} - \frac{p(z,t)}{H}\right] + \frac{1}{R}\frac{\partial p(z,t)}{\partial t} = \frac{k}{\mu}\frac{\partial^2 p(z,t)}{\partial z^2} \tag{3.24}$$

Supporting a load σ_0 on z-axis, Eq.(3.17) becomes:

$$\sigma_{zz} = \left(2G_\beta^T + G_\beta^\nu\right)\ {}_c\mathcal{D}_t^\beta \frac{\partial w(z,t)}{\partial z} - \alpha\left({}_c\mathcal{D}_t^\beta p\right)(z,t) = -\bar{\sigma} \tag{3.25}$$

Deriving Eq.(3.25) and replacing it in Eq.(3.24) :

$$C_\beta\left({}_c\mathcal{D}_t^{\beta+1} p\right)(z,t) + C_\alpha\frac{\partial p(z,t)}{\partial t} = \frac{\partial^2 p(z,t)}{\partial z^2} \tag{3.26}$$

C_α and C_β are the so-called *anomalous consolidation coefficients* ("anomalous" in the sense of fractional calculus), defined as:

$$C_\beta = \frac{\alpha\mu}{k}\left(\frac{\alpha}{2G_\beta^T + G_\beta^\nu} - \frac{1}{H}\right) \quad \text{and} \quad C_\alpha = \frac{\mu}{Rk} \tag{3.27}$$

Particularly, as $\beta = 0$ the porous medium has an elastic behavior, the well-known consolidation equation is obtained, in one-dimensional condition (see *Eq.5.4 [1]*). In detail, the sum of these two coefficients returns the inverse of the so-called consolidation constant c_v $[m^2/s]$.

$$C_\beta + C_\alpha = \frac{1}{c_v} \tag{3.28}$$

Eq.(3.26), with *Initial Conditions* (IC) and BD, leads to the complete solution of the diffusion problem in a porous medium. In detail, this diffusion phenomenon is ruled by three parameters, namely the anomalous consolidation coefficients C_α and C_β, and the order of Caputo's derivative β.
To further reduce the number of parameters, the relation (3.26) can be converted into a non-dimensional form using the parameters reported below:

$$\bar{p} = \frac{p}{\sigma_0} \quad \bar{C}_\beta = \frac{C_\beta}{\tau_c} \quad \bar{t} = \frac{t}{\tau_c} \quad \bar{z} = \frac{z}{h} \tag{3.29}$$

So that, $\bar{C}_\beta$ is the part of the anomalous consolidation coefficient which is independent of β. Meanwhile, considering τ_c the characteristic time of the process and h the cylinder height, $\bar{t}$ and $\bar{z}$ respectively correspond to the dimensionless values of time and space.
Consequently, the non-dimensional equation of *Eq.*(3.26) is:

$$\frac{\partial}{\partial \bar{t}}\left[\bar{C}_\beta(\mathcal{D}_{\bar{t}}^{\beta}\bar{p})(\bar{z},\bar{t}) + \frac{C_\alpha}{\tau_c}\bar{p}(\bar{z},\bar{t})\right] = \frac{\partial^2 \bar{p}(\bar{z},\bar{t})}{\partial \bar{z}^2} \tag{3.30}$$

Eq.(3.30) has been solved through variable separation method (see *Section 2.2.1 [21]*), namely separating $\bar{p}(\bar{z},\bar{t})$ into non-dimensional space-dependent $\phi(\bar{z})$ and non-dimensional time-dependent $y(\bar{t})$ functions, as reported below:

$$\bar{p}(\bar{z},\bar{t}) = \phi(\bar{z})y(\bar{t}) \tag{3.31}$$

After substituting *Eq.*(3.31) into *Eq.*(3.30), a separation constant λ has been introduced:

$$\frac{1}{\phi}\frac{d^2\phi}{d\bar{z}^2} = \frac{1}{y}\left[\bar{C}_\beta \mathcal{D}^{\beta+1} y + \frac{C_\alpha}{\tau_c}\frac{dy}{d\bar{t}}\right] = -\lambda^2 \tag{3.32}$$

Eq.(3.32) is equivalent to the two following differential equations:

$$\phi''(\bar{z}) + \lambda^2\phi(\bar{z}) = 0 \tag{3.33a}$$

$$\bar{C}_\beta\left(\mathcal{D}^{\beta+1}y\right)(\bar{t}) + \frac{C_\alpha}{\tau_c}y'(\bar{t}) + \lambda^2 y(\bar{t}) = 0 \tag{3.33b}$$

The first equation (3.33a)is related to space-evolution, while the second one (3.33b) is related to time-evolution. In detail, *Eq.*(3.33a) is a second-order differential equation whose general solution is, for $\lambda > 0$:

$$\phi(\bar{z}) = D_1 \cos(\lambda \bar{z}) + D_2 \sin(\lambda \bar{z}) \tag{3.34}$$

Where D_1 and D_2 are two arbitrary constants, which have been evaluated through the BD.
Solving the non-dimensional space $\bar{z}$ problem, the non-dimensional time dimension has also been solved. Particularly, Laplace transform method [22, 23, 24, 25] has been used to solve the fractional differential equation of *Eq.*(3.33b), so that:

$$Y(s) = \frac{y(0)\left[\bar{C}_\beta s^\beta + \frac{C_\alpha}{\tau_c}\right] + \bar{C}_\beta s^{\beta-1} y'(0)}{\bar{C}_\beta s^{\beta+1} + \frac{C_\alpha}{\tau_c} s + \lambda^2} \tag{3.35}$$

Where, the inverse Laplace transform is: $y(\bar{t}) = \mathcal{L}^{-1}\{Y(s)\}$. Consequently, the solution is (see *Eq.5.3.38 [22]*):

$$\begin{aligned} y(\bar{t}) = & \sum_{k=0}^{\infty} \left(-\frac{\lambda^2}{\bar{C}_\beta}\right)^k \frac{\bar{t}^{k(\beta+1)}}{k!} E^k_{\beta,k(\beta+1)+1}\left(-\frac{C_\alpha}{\tau_c \bar{C}_\beta}\bar{t}^\beta\right) + \\ & + \frac{C_\alpha}{\tau_c \bar{C}_\beta} \sum_{k=0}^{\infty} \left(-\frac{\lambda^2}{\bar{C}_\beta}\right)^k \frac{\bar{t}^{k(\beta+1)+\beta}}{k!} E^k_{\beta,(\beta+1)(k+1)}\left(-\frac{C_\alpha}{\tau_c \bar{C}_\beta}\bar{t}^\beta\right) \end{aligned} \tag{3.36}$$

$E^k_{\beta,k(\beta+1)}$ is the three parameters *Mittag-Leffler function* [26, 27]. In any case, this function is commonly used to find the solution to initial value problems of a class of fractional partial differential equations (PDE).
Replacing Eq.(3.36) and (3.34) into Eq.(3.31), the general solution is:

$$\begin{aligned} \bar{p}(\bar{z},\bar{t}) = & (D_1 \cos(\lambda \bar{z}) + D_2 \sin(\lambda \bar{z})) \sum_{k=0}^{\infty} \left(-\frac{\lambda^2}{\bar{C}_\beta}\right)^k \frac{\bar{t}^{k(\beta+1)}}{k!} E^k_{\beta,k(\beta+1)+1}\left(-\frac{C_\alpha}{\tau_c \bar{C}_\beta}\bar{t}^\beta\right) + \\ & + \frac{C_\alpha}{\tau_c \bar{C}_\beta} \sum_{k=0}^{\infty} \left(-\frac{\lambda^2}{\bar{C}_\beta}\right)^k \frac{\bar{t}^{k(\beta+1)+\beta}}{k!} E^k_{\beta,(\beta+1)(k+1)}\left(-\frac{C_\alpha}{\tau_c \bar{C}_\beta}\bar{t}^\beta\right) \end{aligned} \tag{3.37}$$

In the following sections numerical examples for a semi-drained condition as well as of an undrained condition will be exploited to show the effect of fluid diffusion across the pores of an FHM, namely: in *Section 3.3.1* with initial pressure zero at $z = 0$ and in *Section 3.3.2* with pressure zero for $z = 0$ and $z = h$. In detail, the input parameters of the mathematical equation are $\tau_c = 30s, \bar{C}_\beta = 7s^\beta/m^2, C_\alpha = 8s/m^2$. The use of these values has been an arbitrary choice of the authors in order to achieve steady-state flow and to have a qualitative representation of the fractional diffusion phenomenon.

3.3.1 Confined Compression test

The derivation order β on the *Eq.*(3.30) in an unconfined compression test has been analyzed in this section. It means that the pressure of the water under the load is zero,i.e. on the top surface because the permeability of the slab through which the load is applied is assumed to be large concerning that of the soil. Moreover, no water can escape through the bottom. Consequently, for the non-dimensional space *Eq.*(3.33a), the BD are:

$$\begin{cases} \bar{p}(1,t) = \phi(1)y(t) = \phi(1) = 0 \\ \dfrac{\partial \bar{p}\,(0,t)}{\partial \bar{z}} = \phi^{'}(0)y\,(t) = \phi^{'}(0) = 0 \end{cases} \tag{3.38}$$

Solving Eq.(3.33a), It implies that $D_2 = 0$ and $cos(\lambda) = 0 \rightarrow \lambda_n = \frac{(2n-1)\pi}{2}$; with $n = 1, 2, 3.....$ So Eq.(3.34) becomes, trivial solution excluded,

$$\phi(\bar{z}) = D_1 \cos{(\lambda_n \bar{z})} \tag{3.39}$$

To satisfy ID, $p(z, \bar{t}) = 1$ at $\bar{t} = 0$ has been set, obtaining:

$$\sum_{n=1}^{\infty} D_n \cos{(\lambda_n \bar{z})} = 1 \tag{3.40}$$

due to the fact that $\forall n \rightarrow y_n(0) = 1$.
This Sturm-Liouville series on $0 < \bar{z} < 1$ can be thought of as a Fourier cosine series on $0 < \bar{z} < 2$ for which the even-numbered cosine terms are absent [28]. The orthogonality relations have been used to determine the coefficients D_n:

$$D_n = 2\int_0^1 \cos{(\lambda_n \bar{z})} d\bar{z} = \frac{4(-1)^n}{\pi(1-2n)} \tag{3.41}$$

Therefore, the solution to the dimensionless problem in a confined system is:

$$\begin{aligned} \bar{p}(\bar{z},\bar{t}) = {} & \frac{4}{\pi}\sum_{n=1}^{\infty}\frac{(-1)^n}{1-2n}\cos{(\lambda_n\bar{z})}\sum_{k=0}^{\infty}\left(-\frac{\lambda_n^2}{\bar{C}_\beta}\right)^k\frac{\bar{t}^{k(\beta+1)}}{k!}E^k_{\beta,k(\beta+1)+1}\left(-\frac{C_\alpha}{\tau_c\bar{C}_\beta}\bar{t}^\beta\right) + \\ & + \frac{C_\alpha}{\tau_c\bar{C}_\beta}\sum_{k=0}^{\infty}\left(-\frac{\lambda_n^2}{\bar{C}_\beta}\right)^k\frac{\bar{t}^{k(\beta+1)+\beta}}{k!}E^k_{\beta,k(\beta+1)+1+\beta}\left(-\frac{C_\alpha}{\tau_c\bar{C}_\beta}\bar{t}^\beta\right) \end{aligned} \tag{3.42}$$

Thereafter, to show the trend of pressure with the variation of non-dimensional $\bar{z}$-coordinate and $\bar{t}$-time, we solved *Eq.*(3.42) with *Wolfram Mathematica 13.1 Software*, using the following equation:

$$\begin{aligned} \bar{f}_1(\beta,\bar{t},\bar{z}) = {} & \frac{4}{\pi}\sum_{n=1}^{N}\frac{(-1)^n}{1-2n}\cos\left[\frac{(2n-1)\pi\bar{z}}{2}\right]\sum_{k=0}^{100}\left(-\frac{\left(\frac{(2n-1)\pi z}{2}\right)^2\tau_c^\beta}{C_\beta}\right)^k\frac{\bar{t}^{(\beta+1)k}}{k!} \\ & \left(\frac{\Gamma[k+1]}{\Gamma[k(\beta+1)+1]} - \frac{C_\alpha\tau_c^{\beta-1}\bar{t}^\beta\Gamma[k+2]}{C_\beta\Gamma[\beta+k(\beta+1)+1]}\right) + \left(-\frac{\left(\frac{(2n-1)\pi z}{2}\right)^2\tau_c^\beta}{C_\beta}\right)^k\frac{C_\alpha\tau_c^{\beta-1}\bar{t}^{\beta+(\beta+1)k}}{C_\beta k!} \\ & \left(\frac{\Gamma[k+1]}{\Gamma[\beta+k(\beta+1)+1]} - \frac{C_\alpha\tau_c^{\beta-1}\bar{t}^\beta\Gamma[k+2]}{C_\beta\Gamma[2\beta+k(\beta+1)+1]}\right) \end{aligned} \tag{3.43}$$

Since the three parameters Mittag-Leffler's function isn't present in the special functions of Wolfram Mathematica, the Gamma Eulero function has been adopted into the code based on its definition [26, 27]. This solution (3.43) is used to solve the problem for intermediate value of β in the fractional poromecanical model, in particular $\beta = 0, 0.25, 0.50, 0.75, 0.90$ and 1, fixing the value of the dimensionless time $\bar{t}$, as shown in *Figure 3.7.* Meanwhile the authors used Eq.(3.44a) and (3.44b) to solve the particular solution of Eq. (3.42) for $\beta = 0$ and $\beta = 1$, respectively.

$$\bar{p}_1(\bar{t}, \bar{z}) = \frac{4}{\pi} \sum_{n=1}^{N} \frac{(-1)^n}{1-2n} \cos\left[\frac{(2n-1)\pi z}{2}\right] e^{-\frac{\left(\frac{(2n-1)\pi \bar{z}}{2}\right)^2 \bar{t}\tau_c}{C_\alpha + C_\beta \tau_c}} \tag{3.44a}$$

$$\bar{g}_1(\bar{t}, \bar{z}) = \frac{4}{\pi} \sum_{n=1}^{N} \frac{(-1)^n}{1-2n} \cos\left[\frac{(2n-1)\pi \bar{z}}{2}\right] e^{-\frac{C_\alpha t}{2C_\beta}} \left[\cos\left(\frac{t\sqrt{4C_\beta\left(\frac{(2n-1)\pi z}{2}\right)^2 \tau_c - C_\alpha^2}}{2C_\beta}\right) + \right.$$
$$\left. + \frac{C_\alpha \sin\left(\frac{t\sqrt{4C_\beta\left(\frac{(2n-1)\pi z}{2}\right)^2 \tau_c - C_\alpha^2}}{2C_\beta}\right)}{\sqrt{4C_\beta\left(\frac{(2n-1)\pi z}{2}\right)^2 \tau_c - C_\alpha^2}}\right] \tag{3.44b}$$

3.3.2 Unconfined Compression test

The fully draining case has been analyzed in this section. Considering *Eq.*(3.37), only the BD changes because in this case water cannot escape laterally, but it can escape through both the bottom and top surface; so the BDs are:

$$\begin{cases} \bar{p}(1, \bar{t}) = \phi(1)y(\bar{t}) = \phi(1) = 0 \\ \bar{p}(0, \bar{t}) = \phi(0)y(\bar{t})) = \phi(0) = 0 \end{cases} \tag{3.45}$$

It implies that $D_1 = 0$ and $sin(\lambda) = 0 \rightarrow \lambda_n = (2n-1)\pi;$ with $n = 1, 2, 3.....$ So, *Eq.*(3.33b) becomes, trivial solution excluded,

$$\phi(\bar{z}) = D_2 \sin(\lambda_n \bar{z}) \tag{3.46}$$

On the other side, considering the non-dimensional time function $y(\bar{t})$, it remains unchanged as well as *Eq.*(3.36) is still a solution of *Eq.*(3.33a). Consequently,

$$\bar{p}(\bar{z}, \bar{t}) = \sum_{n=1}^{\infty} D_n \sin(\lambda_n \bar{z}) y_n(\bar{t}) \tag{3.47}$$

It is an extension of *Eq.*(3.31). Thereafter, as done in *Section 3.3.1*, the orthogonality relations has been used to determine the coefficients D_n:

$$D_n = 2 \int_0^1 \sin(\lambda_n \bar{z}) d\bar{z} = \frac{4(-1)^{2n}}{\pi(2n-1)} \tag{3.48}$$

Therefore, the general solution to the dimensionless problem for fully drained cases is:

$$\bar{p}(\bar{z},\bar{t}) = \frac{4}{\pi}\sum_{n=1}^{\infty}\frac{(-1)^{2n}}{2n-1}\sin\left(\lambda_n\bar{z}\right)\sum_{k=0}^{\infty}\left(-\frac{\lambda_n^2}{\bar{C}_\beta}\right)^k\frac{\bar{t}^{k(\beta+1)}}{k!}E^k_{\beta,k(\beta+1)+1}\left(-\frac{C_\alpha}{\tau_c\bar{C}_\beta}\bar{t}^\beta\right)+$$

$$+\frac{C_\alpha}{\tau_c\bar{C}_\beta}\sum_{k=0}^{\infty}\left(-\frac{\lambda_n^2}{\bar{C}_\beta}\right)^k\frac{\bar{t}^{k(\beta+1)+\beta}}{k!}E^k_{\beta,k(\beta+1)+1+\beta}\left(-\frac{C_\alpha}{\tau_c\bar{C}_\beta}\bar{t}^\beta\right) \tag{3.49}$$

Thereafter, *Eq.*(3.49) has been implemented into Wolfram Mathematica, using *Eq.* (3.50a) for intermediate value of β, while *Eq.*(3.50b) and *Eq.*(3.50c) for β equals to zero and one, respectively.

$$f_2(\beta,\bar{t},\bar{z}) = \frac{4}{\pi}\sum_{n=1}^{N}\frac{(-1)^{2n}}{2n-1}\sin\left[(2n-1)\pi\bar{z}\right]\sum_{k=0}^{100}\left(-\frac{\left((2n-1)\pi z\right)^2\tau_c^\beta}{C_\beta}\right)^k$$

$$\frac{\bar{t}^{(\beta+1)k}}{k!}\left(\frac{\Gamma[k+1]}{\Gamma[k(\beta+1)+1]}-\frac{C_\alpha\tau_c^{\beta-1}t^\beta\Gamma[k+2]}{C_\beta\Gamma[\beta+k(\beta+1)+1]}\right)+\left(-\frac{\left((2n-1)\pi z\right)^2\tau_c^\beta}{C_\beta}\right)^k$$

$$\frac{C_\alpha\tau_c^{\beta-1}\bar{t}^{\beta+(\beta+1)k}}{C_\beta k!}\left(\frac{\Gamma[k+1]}{\Gamma[\beta+k(\beta+1)+1]}-\frac{C_\alpha\tau_c^{\beta-1}\bar{t}^\beta\Gamma[k+2]}{C_\beta\Gamma[2\beta+k(\beta+1)+1]}\right) \tag{3.50a}$$

$$\bar{p}_2(\bar{t},\bar{z}) = \frac{4}{\pi}\sum_{n=1}^{N}\frac{(-1)^{2n}}{2n-1}\sin\left[(2n-1)\pi\bar{z}\right]e^{-\frac{\left((2n-1)\pi z\right)^2\bar{t}\tau_c}{C_\alpha+C_\beta\tau_c}} \tag{3.50b}$$

$$\bar{g}_2(\bar{t},\bar{z}) = \frac{4}{\pi}\sum_{n=1}^{N}\frac{(-1)^{2n}}{2n-1}\sin\left[(2n-1)\pi z\right]e^{-\frac{C_\alpha t}{2C_\beta}}\left[\cos\left(\frac{\bar{t}\sqrt{4C_\beta\left((2n-1)\pi\bar{z}\right)^2\tau_c-C_\alpha^2}}{2C_\beta}\right)+\right.$$

$$\left.+\frac{C_\alpha\sin\left(\frac{\bar{t}\sqrt{4C_\beta\left((2n-1)\pi z\right)^2\tau_c-C_\alpha^2}}{2C_\beta}\right)}{\sqrt{4C_\beta\left((2n-1)\pi\bar{z}\right)^2\tau_c-C_\alpha^2}}\right] \tag{3.50c}$$

3.4 Poromechanics Of a Cylindrical FHM under variable load

In *Section 3.3* we considered a viscoelastic porous medium using Caputo's fractional derivative in the constitutive flow-pressure equations, simulating a confined compression test in *Section 3.3.1*, as well as a fully drained compression test in *Section 3.3.2.* This relation, along with initial and BD, leads to the complete solution of the diffusion phenomenon in a biological porous medium. However, we considered a constant load σ_0, but it is known that biological tissues are generally subjected to a variable load during normal journey activity, such as walking, cycling, running, etc. For this reason, in this section we extended the previous application, considering the diffusion phenomenon within a porous medium under a cyclic load. This allows us to elucidate structure-function relationships and predict the mechanical response

of biological tissue under various and realistic loading conditions.
In detail, we considered a symmetric cylinder of FHM, as shown in *Figure 3.3*, that allows for the reduction of the kinematic field represented by the components of the displacement vector along a cylindrical reference system, namely: $u_r\left(r,\theta,z,t\right)$, $u_\theta\left(r,\theta,z,t\right)$ and $u_z\left(r,\theta,z,t\right)$. Indeed, we also assumed that $u_r=u_\theta=0$ everywhere and $u_z\left(r,\theta,z,t\right)=w\left(z,t\right)$. Consequently, the first invariant is:

$$\theta_I=\varepsilon_{zz}=\frac{\partial w\left(z,t\right)}{\partial z} \tag{3.51}$$

The specimen is loaded by a cyclic and uniform pressure $\sigma(t)=\sigma_0+\sin\left(\omega t\right)$ on the free surface of the cylinder, where σ_0 and ω are the amplitude and the frequency of the applied load, respectively.

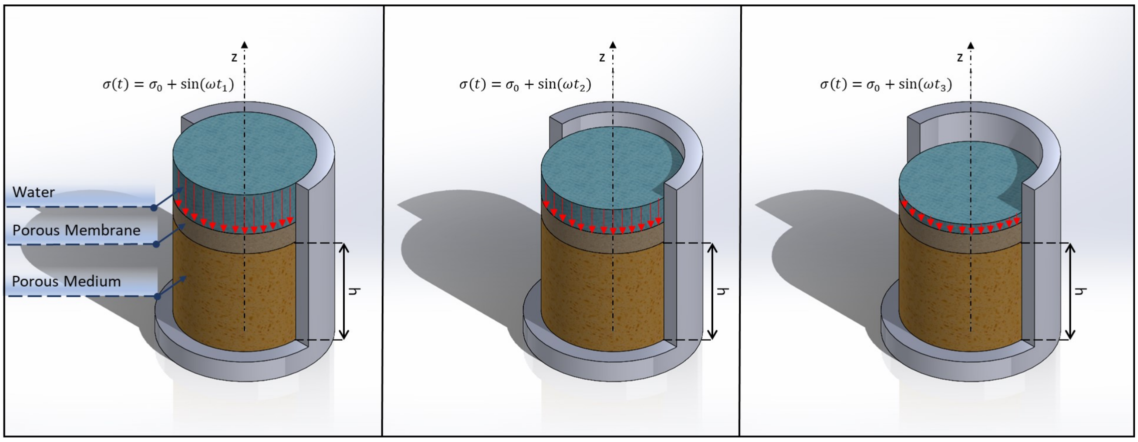

Figure 3.3: *Schematic representation of a confined compression test for three different time instants, where a variable pressure $\sigma(t)$ is imposed on a porous FHM through a highly porous membrane.*

Consequently, the differential fluid *Eq.*(3.24) is still valid. Meanwhile, supporting a load $\sigma(t)=\sigma_0+\sin\left(\omega t\right)$ on z-axis, *Eq.*(3.17) becomes:

$$\sigma_{zz}=\left(2G_\beta^T+G_\beta^\nu\right)\,{}_c\mathcal{D}_t^\beta\frac{\partial w(z,t)}{\partial z}-\alpha\left({}_c\mathcal{D}_t^\beta p\right)(z,t)=-\sigma_0-\sin\left(\omega t\right) \tag{3.52}$$

Deriving *Eq.*(3.52) and replacing it in *Eq.*(3.24):

$$C_\beta\left({}_c\mathcal{D}_t^{\beta+1}p\right)(z,t)+C_\alpha\frac{\partial p(z,t)}{\partial t}+A_\beta\cos\left(\omega t\right)=\frac{\partial^2 p(z,t)}{\partial z^2} \tag{3.53}$$

Where $A_\beta=\frac{\alpha\mu\omega}{k(2G_\beta^T+G_\beta^\nu)}$ is the amplitude of sinusoidal function, while C_α and C_β are the so-called *anomalous consolidation coefficients*, already defined in *Eq.*(3.26).
Eq.(3.53), with initial and BD, leads to the complete solution of the diffusion problem in a porous medium. Despite the presence of a non-constant load, the diffusion phenomenon is still ruled by three parameters, as in the previous analysis (*Section*

3.3), namely the anomalous consolidation coefficients C_α and C_β, and the order of Caputo's derivative β; while A_β depends on the same variable.
To further reduce the number of parameters, relation (3.53) can be converted into a non-dimensional form using the parameters: $\bar{p}$, $\bar{C}_\beta$, $\bar{t}$,and $\bar{z}$, as expressed in *Eq.* (3.29).
Consequently, we can rearrange *Eq.3.53* into a non-dimensional pressure equation:

$$\frac{\partial}{\partial \bar{t}}\left[\bar{C}_\beta(\mathcal{D}_{\bar{t}}^{\beta}\bar{p})(\bar{z},\bar{t})+\frac{C_\alpha}{\tau_c}\bar{p}(\bar{z},\bar{t})\right]-\frac{\partial^2\bar{p}(\bar{z},\bar{t})}{\partial\bar{z}^2}=Q(\bar{z},\bar{t}) \tag{3.54}$$

Eq.(3.54) is a non-homogeneous fractional equation with homogeneous BD (3.56), that can be solved using the eigenfunction expansions of solutions. Compared to the previous Section 3.3.1, the only difference is related to the presence of function $Q(\bar{z},\bar{t})$ in the PDE (3.30).

$$Q(\bar{z},\bar{t})=-A_\beta\cos\left(\omega\bar{t}\tau_c\right) \tag{3.55}$$

It describes the generation of pressure at position $\bar{z}$ and time $\bar{t}$ due to the variable external load. For particular cases of low frequency, so that the external load is constant, then $Q\simeq 0$ and Eq.(3.54) is equal to Eq.(3.30).
Considering a confined compression test, as shown in *Figure 3.3*, the homogeneous BD are:

$$\begin{cases}\bar{p}(1,\bar{t})=0\\ \dfrac{\partial\bar{p}\,(0,\bar{t})}{\partial\bar{z}}=0\end{cases} \tag{3.56}$$

Consequently, the Sturm-Liouville can be adopted as in the corresponding homogeneous problem, i.e. $Q\equiv 0$. Then, we can use the set of eigenvalues $\phi_n(\bar{z})$ obtained in *Section 3.3.1* to solve the limit-value/eigenvalue problem of the corresponding homogeneous differential equation (ODE), briefly :

$$\begin{cases}\lambda_k=\frac{(2k-1)\pi}{2h};\ \text{with } k=1,2,3....\\ \phi_k(\bar{z})=\cos\left(\lambda_k\bar{z}\right)\end{cases} \tag{3.57}$$

Thereafter, for each value of $\bar{t}$, we can treat $Q(\bar{t})$ and $\bar{p}(\bar{z};\bar{t})$ as functions of just $\bar{z}$. Since our set of eigenfunctions $\phi_k(\bar{z})$ is a complete orthogonal set, we can express $Q(\bar{t})$ and $\bar{p}(\bar{z},\bar{t})$ in terms of the following eigenfunctions:

$$\bar{p}(\bar{z},\bar{t})=\sum_{k=1}^{\infty}a_k(\bar{t})\phi_k(\bar{z}) \tag{3.58}$$

and

$$Q(\bar{z},\bar{t})=\sum_{k=1}^{\infty}q_k(\bar{t})\phi_k(\bar{z}) \tag{3.59}$$

Anyway, the use of eigenfunctions (3.58) and (3.59) should ensure that $\bar{p}(\bar{z},\bar{t})$ have to satisfies the given BD (3.58). Particularly, the $q_k(\bar{t})$ are the generalized Fourier coefficients of $Q(\bar{t})$ with respect to the $\phi_k(\bar{z})$ at time $\bar{t}$ .Then, the orthogonality of the eigenfunctions gives the system of ODEs:

$$q_k(\bar{t}) = \frac{\int_0^1 Q(\bar{z},\bar{t}) \cdot \phi_k(\bar{z}) d\bar{z}}{\int_0^1 \phi_k^2(\bar{z}) d\bar{z}} = A_\beta \cos\left(\omega \bar{t} \tau_c\right) \cdot \frac{4(-1)^k}{\pi(1-2k)} \tag{3.60}$$

Here, we cannot calculate $a_k(\bar{t})$ as we calculated $q_k(\bar{t})$. However, since $\phi_k(\bar{z})$ are eigenvalues of the corresponding boundary value problem, inserting $p_k(\bar{t},\bar{z})$ for $\bar{p}$ in the left-hand side of (3.54) yields the result. Consequently, by substituting $Q(\bar{t})$ and $\bar{p}(\bar{z},\bar{t})$ into the given PDE with their expansions to the eigenvalues, a differential equation is obtained for each $a_k(\bar{t})$. Solving this differential equation yields the formula for each $a_k(\bar{t})$, a formula that involves one or two arbitrary constants.
So that, replacing $\bar{p}$ with $p_k(\bar{z};t) = a_k(\bar{t})\phi_k(\bar{z})$ in the left side of 3.54:

$$\begin{aligned}
&\frac{\partial}{\partial \bar{t}}\left[\bar{C}_\beta(\mathcal{D}_{\bar{t}}^{\beta} p_k) + \frac{C_\alpha}{\tau_c} p_k\right] - \frac{\partial^2 p_k}{\partial \bar{z}^2} = \\
&\qquad = \frac{\partial}{\partial \bar{t}}\left[(\mathcal{D}_{\bar{t}}^{\beta} a_k(\bar{t})\phi_k(\bar{z})) + \frac{C_\alpha}{\tau_c} a_k(\bar{t})\phi_k(\bar{z})\right] - \frac{\partial^2}{\partial \bar{z}^2}\left[a_k(\bar{t})\phi_k(\bar{z})\right] \\
&\qquad = \phi_k(\bar{z})\left[\bar{C}_\beta(\mathcal{D}_{\bar{t}}^{\beta+1} a_k)(\bar{t}) + \frac{C_\alpha}{\tau_c}\frac{\partial a_k(\bar{t})}{\partial \bar{t}}\right] - a_k(\bar{t})\frac{\partial^2 \phi_k(\bar{z})}{\partial \bar{z}^2} \\
&\qquad = \cos\left(\lambda_k \bar{z}\right)\left[\bar{C}_\beta(\mathcal{D}_{\bar{t}}^{\beta+1} a_k)(\bar{t}) + \frac{C_\alpha}{\tau_c}\frac{\partial a_k(\bar{t})}{\partial \bar{t}}\right] - a_k(\bar{t})\frac{\partial^2 \cos\left(\lambda_k \bar{z}\right)}{\partial \bar{z}^2} \\
&\qquad = \cos\left(\lambda_k \bar{z}\right)\left[\bar{C}_\beta(\mathcal{D}_{\bar{t}}^{\beta+1} a_k)(\bar{t}) + \frac{C_\alpha}{\tau_c}\frac{\partial a_k(\bar{t})}{\partial \bar{t}}\right] + a_k(\bar{t})\lambda_k^2 \cos\left(\lambda_k \bar{z}\right) \\
&\qquad = \cos\left(\lambda_k \bar{z}\right)\left[\bar{C}_\beta(\mathcal{D}_{\bar{t}}^{\beta+1} a_k)(\bar{t}) + \frac{C_\alpha}{\tau_c}\frac{\partial a_k(\bar{t})}{\partial \bar{t}} + a_k(\bar{t})\lambda_k^2\right]
\end{aligned} \tag{3.61}$$

And thus, using the eigenfunction expansions for $\bar{p}$ and Q, we have:

$$\begin{aligned}
\frac{\partial}{\partial \bar{t}}\left[\bar{C}_\beta(\mathcal{D}_{\bar{t}}^{\beta} p)(\bar{z},\bar{t}) + \frac{C_\alpha}{\tau_c} p(\bar{z},\bar{t})\right] - \frac{\partial^2 p(\bar{z},\bar{t})}{\partial \bar{z}^2} &= Q(\bar{z},\bar{t}) \\
\frac{\partial}{\partial \bar{t}}\left[\bar{C}_\beta \mathcal{D}_{\bar{t}}^{\beta} \sum_{k=1}^{\infty} p_k(\bar{z},\bar{t}) + \frac{C_\alpha}{\tau_c}\sum_{k=1}^{\infty} p_k(\bar{z},\bar{t})\right] - \frac{\partial^2}{\partial \bar{z}^2}\sum_{k=1}^{\infty} p_k(\bar{z},\bar{t}) &= \sum_{k=1}^{\infty} q_k(\bar{t})\phi_k(\bar{z}) \\
\sum_{k=1}^{\infty}\left[\bar{C}_\beta \mathcal{D}_{\bar{t}}^{\beta+1} p_k(\bar{z},\bar{t}) + \frac{C_\alpha}{\tau_c}\frac{\partial p_k(\bar{z},\bar{t})}{\partial \bar{t}} - \frac{\partial^2 p_k(\bar{z},\bar{t})}{\partial \bar{z}^2}\right] &= \sum_{k=1}^{\infty} q_k(\bar{t})\phi_k(\bar{z}) \\
\sum_{k=1}^{\infty}\left[\bar{C}_\beta(\mathcal{D}_{\bar{t}}^{\beta+1} a_k)(\bar{t}) + \frac{C_\alpha}{\tau_c}\frac{\partial a_k(\bar{t})}{\partial t} + \lambda_k^2 a_k(\bar{t})\right]\cos\left(\lambda_k \bar{z}\right) &= \sum_{k=1}^{\infty} q_k(\bar{t})\cos\left(\lambda_k \bar{z}\right)
\end{aligned} \tag{3.62}$$

Hence, for each k , it follows that:

$$\bar{C}_\beta(\mathcal{D}_{\bar{t}}^{\beta+1} a_k)(\bar{t}) + \frac{C_\alpha}{\tau_c} a_k'(\bar{t}) + \lambda_k^2 a_k(\bar{t}) = q_k(\bar{t}) \tag{3.63}$$

Eq.(3.63) is a non-homogeneous fractional differential equation with constant coefficients that can be solved using the Laplace transform method. Anyway, the general solution to the equation 3.63 is also a sum of its particular solution and the general solution to the corresponding homogeneous equation, i.e. $q_k(t) = 0$. Consequently, the general time-dependent solution is (see *Eq.5.3.73* [22]):

$$a_k(\bar{t}) = \int_0^{\bar{t}} (\bar{t}-\tau)^{\beta} G_{\beta}(\bar{t}-\tau) q_k(\tau) d\tau + \sum_{j=0}^{1} c_j a_j(\bar{t}) \tag{3.64}$$

Where

$$G_{\beta}(\bar{t}-\tau) = \sum_{n=0}^{N} \left(-\frac{\lambda_k^2}{\bar{C}_{\beta}}\right)^n \frac{(\bar{t}-\tau)^{(\beta+1)n}}{n!} {}_1\Psi_1 \left[\begin{matrix}(n+1,1)\\(\beta+1)n+(\beta+1),\beta\end{matrix} \middle| -\frac{C_{\alpha}}{\bar{C}_{\beta}\tau_c}(\bar{t}-\tau)^{\beta}\right] \tag{3.65a}$$

$$\begin{aligned} a_0(\bar{t}) =& \sum_{n=0}^{N} \left(-\frac{\lambda_k^2}{\bar{C}_{\beta}}\right)^n \frac{\bar{t}^{(\beta+1)n}}{n!} {}_1\Psi_1 \left[\begin{matrix}(n+1,1)\\(\beta+1)n+1,\beta\end{matrix} \middle| -\frac{C_{\alpha}}{\bar{C}_{\beta}\tau_c}\bar{t}^{\beta}\right] + \\ &+ \sum_{n=0}^{N} \left(-\frac{\lambda_k^2}{\bar{C}_{\beta}}\right)^n \frac{\bar{t}^{(\beta+1)n+\beta}}{n!} {}_1\Psi_1 \left[\begin{matrix}(n+1,1)\\(\beta+1)n+1+\beta,\beta\end{matrix} \middle| -\frac{C_{\alpha}}{\bar{C}_{\beta}\tau_c}\bar{t}^{\beta}\right] \end{aligned} \tag{3.65b}$$

while c_j are arbitrary real constants depending on ID, and${}_1\Psi_1$ is the so-called *Wright function* [22, 24].Particularly, the first solution (3.65a) is relative to the particular integral, while the second one (3.65b) is relative to the homogeneous problem.
For brevity, let's further rewrite 3.64 as:

$$a_k(\bar{t}) = \int_0^{\bar{t}} (\bar{t}-\tau)^{\beta} G_{\beta}(\bar{t}-\tau) q_k(\tau) d\tau + c_0 a_0(\bar{t}) \tag{3.66}$$

Thus:

$$\begin{aligned} p(\bar{z},\bar{t}) &= \sum_{k=1}^{\infty} a_k(\bar{t}) \phi_k(\bar{z}) \\ &= \sum_{k=1}^{\infty} \left[\int_0^{\bar{t}} (\bar{t}-\tau)^{\beta} G_{\beta}(\bar{t}-\tau) q_k(\tau) d\tau + c_0 a_0(\bar{t})\right] \cos(\lambda_k \bar{z}) \end{aligned} \tag{3.67}$$

Finally, the initial condition $p(\bar{z}, 0) = 1$ can be applied, obtaining:

$$\begin{aligned} p(\bar{z},0) = \sum_{k=1}^{\infty} a_k(0)\phi_k(\bar{z}) &= \sum_{k=1}^{\infty} [0 + c_0 \cdot 1] \cos(\lambda_k \bar{z}) \\ &= \sum_{k=1}^{\infty} c_0 \cos(\lambda_k \bar{z}) = 1 \end{aligned} \tag{3.68}$$

due to the fact that $\forall k \rightarrow a_k(0) = 1$.
This Sturm-Liouville series on $0 < \bar{z} < 1$ can be thought of as a Fourier cosine series on $0 < \bar{z} < 2$ for which the even-numbered cosine terms are absent [21]. So, the orthogonality relations have been used to determine coefficient c_0:

$$c_0 = 2\int_0^1 \cos(\lambda_k \bar{z}) d\bar{z} = \frac{4(-1)^k}{\pi(1-2k)} \tag{3.69}$$

Therefore, the general solution to the dimensionless problem is:

$$p(\bar{z},\bar{t}) = \sum_{k=0}^{\infty} \frac{4(-1)^k}{\pi(1-2k)} \left[g_\beta(\bar{t}) + a_0(\bar{t})\right] \cos\left(\lambda_k \bar{z}\right) \tag{3.70}$$

with

$$g_\beta(\bar{t}) = \int_0^{\bar{t}} \sum_{n=1}^{N} \left(-\frac{\lambda_k^2}{\bar{C}_\beta}\right)^n \frac{(\bar{t}-\tau)^{(\beta+1)n+\beta}}{n!} {}_1\Psi_1 \left[\begin{matrix}(n+1,1) \\ (\beta+1)n+(\beta+1),\beta\end{matrix} \middle| -\frac{C_\alpha}{\tau_c \bar{C}_\beta}(\bar{t}-\tau)^\beta\right] A_\beta \cos(\omega\tau) d\tau \tag{3.71}$$

In the following section a numerical application for a semi-drained condition will be exploited to show the effect of fluid diffusion across the pores of an FHM.

3.4.1 Confined Compression test

In this section, the authors provide a numerical application for the particular cases of a confined compression test, so that: water pressure is zero on the top surface $z = h$. In detail, the author investigated the choice of model parameters to be used to achieve steady-state flow. In detail, the input parameters used are $\tau_c = 30s, \bar{C}_\beta = 7s^\beta/m^2, C_\alpha = 8s/m^2, \omega = 0.001s^{-1}, A_\beta = 10MPa$. Eq.(3.64) was solved using *Wolfram Mathematica 13.1 Software*, to analyze the evolution of the problem for different values of β, in particular $\beta = 0, 0.25, 0.50, 0.75, 0.90, 1$, fixing the value of the dimensionless time $\bar{t}$.
Nevertheless, since the *Fox-Wright function* is not included in the special functions of the Wolfram Mathematica package, the Gamma Euler function was adopted in the mathematical code according to its definition [26, 27]; obtaining the following equation:

$$\begin{aligned} f_1(\beta,t) = &\sum_{n=0}^{N} \left(-\frac{\left(\frac{(2k-1)\pi z}{2}\right)^2 \tau_c}{C_\beta}\right)^k \frac{t^{n(\beta+1)}}{n!} \left(\frac{\Gamma[n+1]}{\Gamma[n(\beta+1)+1]} - \frac{C_\alpha t^\beta \Gamma[n+2]}{C_\beta \tau_c \Gamma[n(\beta+1)+1+\beta]}\right) + \\ &+ \frac{C_\alpha}{C_\beta \tau_c} \left(-\frac{\left(\frac{(2k-1)\pi z}{2}\right)^2 \tau_c}{C_\beta}\right)^k \frac{t^{n(\beta+1)+\beta}}{n!} \left(\frac{\Gamma[n+1]}{\Gamma[n(\beta+1)+1+\beta]} - \frac{C_\alpha t^\beta \Gamma[n+2]}{C_\beta \tau_c \Gamma[k(\beta+1)+2\beta+1]}\right) \end{aligned} \tag{3.72a}$$

$$\begin{aligned} f_2(\beta,t) = &\int_0^{\bar{t}} (\bar{t}-\tau)^\beta \sum_{n=0}^{N} \left(-\frac{\left(\frac{(2k-1)\pi z}{2}\right)^2 \tau_c}{C_\beta}\right)^k \frac{(t-\tau_c)^{n(\beta+1)}}{n!} \left(\frac{\Gamma[n+1]}{\Gamma[n(\beta+1)+1]} + \right. \\ &\left. - \frac{C_\alpha t^\beta \Gamma[n+2]}{C_\beta \tau_c \Gamma[n(\beta+1)+1+2\beta]}\right) A_\beta \cos(\omega\tau) d\tau \end{aligned} \tag{3.72b}$$

$$f_3(\beta,t,z) = \frac{4}{\pi} \sum_{k=1}^{K} \frac{(-1)^k}{1-2k} \cos\left[\frac{(2k-1)\pi z}{2}\right] \left[f_1(\beta,t) + f_2(\beta,t)\right] \tag{3.72c}$$

$$\begin{aligned} p_1(t,z) = &\frac{4}{\pi} \sum_{k=1}^{K} \frac{(-1)^k}{1-2k} \cos\left[\frac{(2k-1)\pi z}{2}\right] \frac{e^{-\frac{\lambda_k^2 \tau_c}{\bar{C}_\beta \tau_c + C_\alpha} t}}{\tau_c(\lambda_k^4 + \omega^2(\bar{C}_\beta \tau_c + C_\alpha)^2)} \left[-A_\beta \lambda_k^2 + \lambda_k^4 \tau_c + \omega^2 (\bar{C}_\beta \tau_c + C_\alpha)^2 \tau_c + \right. \\ &\left. + A_\beta \lambda_k^2 e^{\frac{\lambda_k^2 \tau_c}{\bar{C}_\beta \tau_c + C_\alpha} t} \cos(\omega \tau_c \bar{t}) + A_\beta (\bar{C}_\beta \tau_c + C_\alpha) \omega e^{\frac{\lambda_k^2 \tau_c}{\bar{C}_\beta \tau_c + C_\alpha} t} \sin(\omega \tau_c \bar{t})\right] \end{aligned} \tag{3.72d}$$

Where the Wright series was approximated to the first two terms. Then, *Eq.*(3.72c) was used to solve the problem for an intermediate value of β in the fractional poromechanical model, while *Eq.*(3.72d) was adopted to solve the particular solution of *Eq.*(3.64) for $\beta = 0$.

3.5 Results

In this paper, the poromechanic of a hereditary porous media was investigated using fractional calculus. Firstly, the constitutive equations for a semi-drained and fully drained condition were found in *Section 3.3.1* and *3.3.2*, respectively. After that, this analysis was extended from constant load to a general and realistic case, considering a confined compression test with variable load in *Section 3.4.1.* In detail, *Eqs.*(3.30) and (3.53) have shown that the biomechanics of FHM is markedly influenced by three parameters in both conditions, namely the anomalous consolidation coefficients C_α and C_β, and the β order of Caputo's fractional derivative. Furthermore, comparing confined and unconfined problem solutions, i.e. *Eqs.*(3.42) and (3.49),it can be seen that these solutions are very similar. The only significant difference is related to the coefficients D_n and the non-dimensional space solution $\phi(\bar{z})$. Particularly, there is the cosine function of $\bar{z}$ in the first case and the sine function in the second one. Anyway, the non-dimensional time solution $y(\bar{t})$ is still the same in both cases. Meanwhile, comparing confined solutions for a constant and variable load, i.e. *Eqs.*(3.42) and (3.70), the only significant difference is related to the non-dimensional time solution $y(\bar{t})$, noting that *Eq.*(3.36) is a part of *Eq.*(3.64). Consequently, when $Q(\bar{t}) \equiv 0$, these two solutions coincide.

After that, the numerical application of founding governing equations was done using Wolfram Mathematica. Particularly, *Figure 3.4, 3.6* and *3.5* showed the relationship between the three parameters considered: dimensionless time $\bar{t}$, dimensionless height inside the cylinder $\bar{z}$ and order of the fractional derivative β, in the three different conditions analyzed. Meanwhile, *Figure 3.7, 3.8* and *3.9* show the trend of non-dimensional pressure $\bar{p}$ for different value of β, in particular $\beta = 0, 0.25, 0.50, 0.75, 0.90$ and 1, fixing the value of the dimensionless time $\bar{t}$.

In any application, It can be seen that the time evolution of the pressure is strongly influenced by the order of Caputo's fractional derivative. The deviation from elastic behavior, i.e. $\beta = 0$, has been revealed in the rapid pressure reduction in both time and space: when $\beta = 0$, pressure remained constant and at the same initial value for almost all of $\bar{z}$-value. This depression effect becomes more pronounced as the deviation from elastic behavior increases, i.e. $\lim_{\beta\to 1}$. In all cases, as time increases the pressure value decreases, but anomalous porous media, namely $\beta \neq 0$, require shorter non-dimensional times than classical one (*Figures 3.7a, 3.8a* and *3.9a*) to reach stability.

Observing the confined compression test in *Section 3.3.1*, it is interesting to note that the non-dimensional pressure gradually decreases when $\beta < 0.5$; on the other side, on the other side, when $\beta \geq 0.5$, the reduction in pressure becomes progressively smaller and the pressure moves to negative values, too (*Figures 3.7d, 3.7e, 3.7f*). As β increases, the $\bar{z}$ value of which it occurs decreases since the hereditary material drives far and far from the elasticity. Moreover, for $\beta = 1$, a fast pressure drop from -1 to 0 is observed (see *Figure 3.7f*). On the other hand, considering the fully drained test in *Section 3.3.2*, the pressure moves to negative values for a smaller value of β, i.e. $\beta = 0.25$ (see *Figure 3.8b*). In addition, when $\beta = 1$ and $\bar{t} \geq 0.60$, the non-dimensional pressure also returns to positive values, but lower than initial values (see *Figure 3.8f*). In the semi-drained test, it happens for a greater value of

$\bar{t}$, i.e. only when $\bar{t} \geq 1.9$, as shown in *Figure 3.10a.* Generally, it is noticed that the solution's dependence on the β value is greater in the fully drained case than in the semi-drained case. As further confirmation, if we compare the pressure trend for the same value of $\bar{t}$, a greater part of the porous medium has a negative value of $\bar{p}$ in the fully drained test, as shown in *Figure 3.11.*

Conversely, the pressure never reaches negative values when the load is not constant (see *Figure 3.6* and *3.9*). Moreover, when $\beta = 1$ the external pressure did not affect $\bar{p}$ (see *Figure 3.9f.* In other words, it behaves like a solid when the applied pressure is weak and imperceptible. In any case, the variable pressure did not affect the material response it behaved as if the applied pressure was constant.

The main result of this study reported the overpressure effect caused by beta-order variability of the constitutive equation. It has been shown that the porous FHM under pressure caused by loading conditions strongly depends on the order of Caputo's fractional derivative: the higher the order of β, the less pronounced the phenomenon. In predicting bone damage, which can be favored by a slow release of overpressure in the presence of repetitive loading, this aspect can be a significant problem. The phenomenon of consolidation occurs when $\beta \geq 0.5$ in the confined compression test under constant load. Furthermore, as $\beta = 1$, it has been shown that the pressure remains constant and moves towards higher values when the non-dimensional time value increases. This effect is interesting since no evidence has been found in the literature of a constant pressure field if the load is variable during time, using classical mathematical modeling to represent material inheritance.

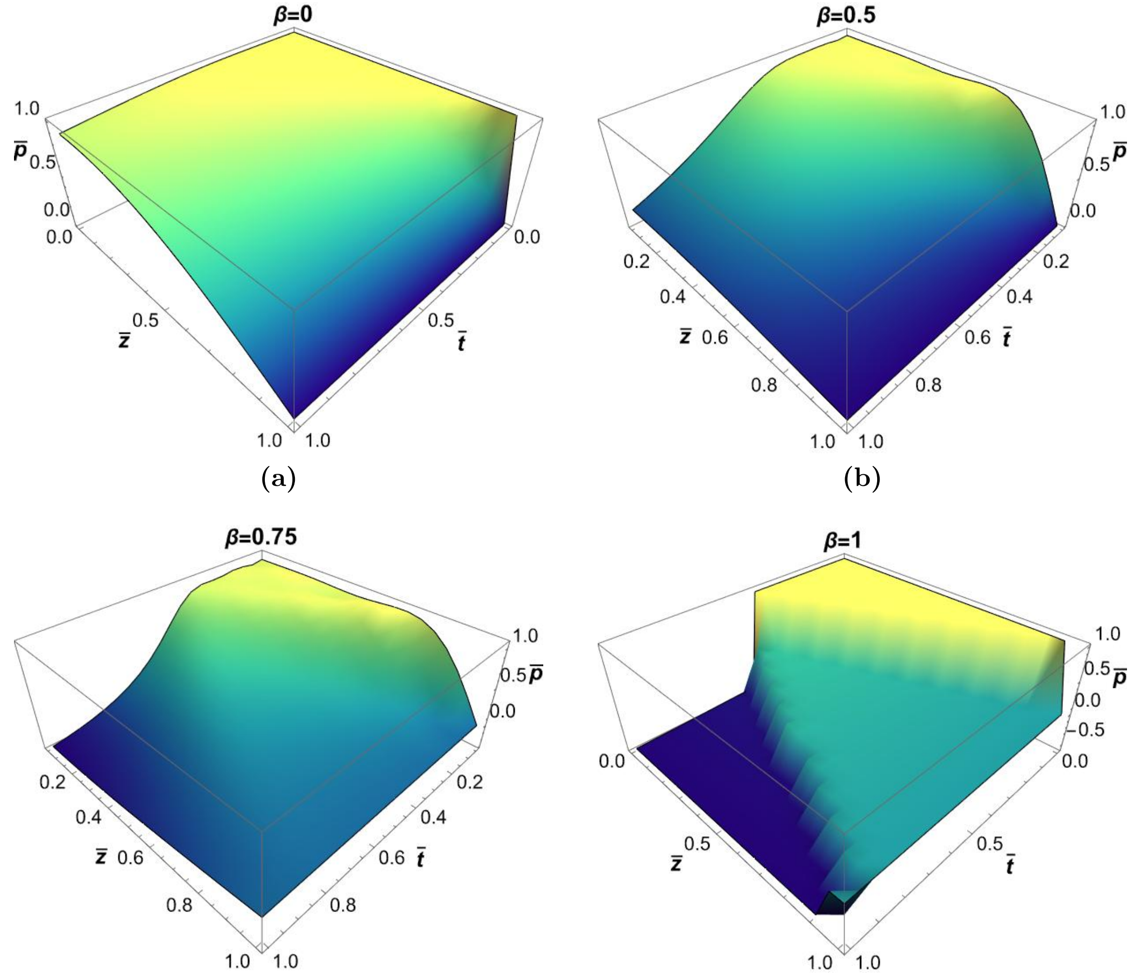

(a) **(b)**

(c) **(d)**

Figure 3.4: *Three-dimensional representation of non-dimensional pressure field* $\bar{p}$ *in the confined compression test with constant load for* $\beta = 0$, $\beta = 0.5$, $\beta = 0.75$ *and* $\beta = 1$, *in* ***(a-d)***, *respectively.*

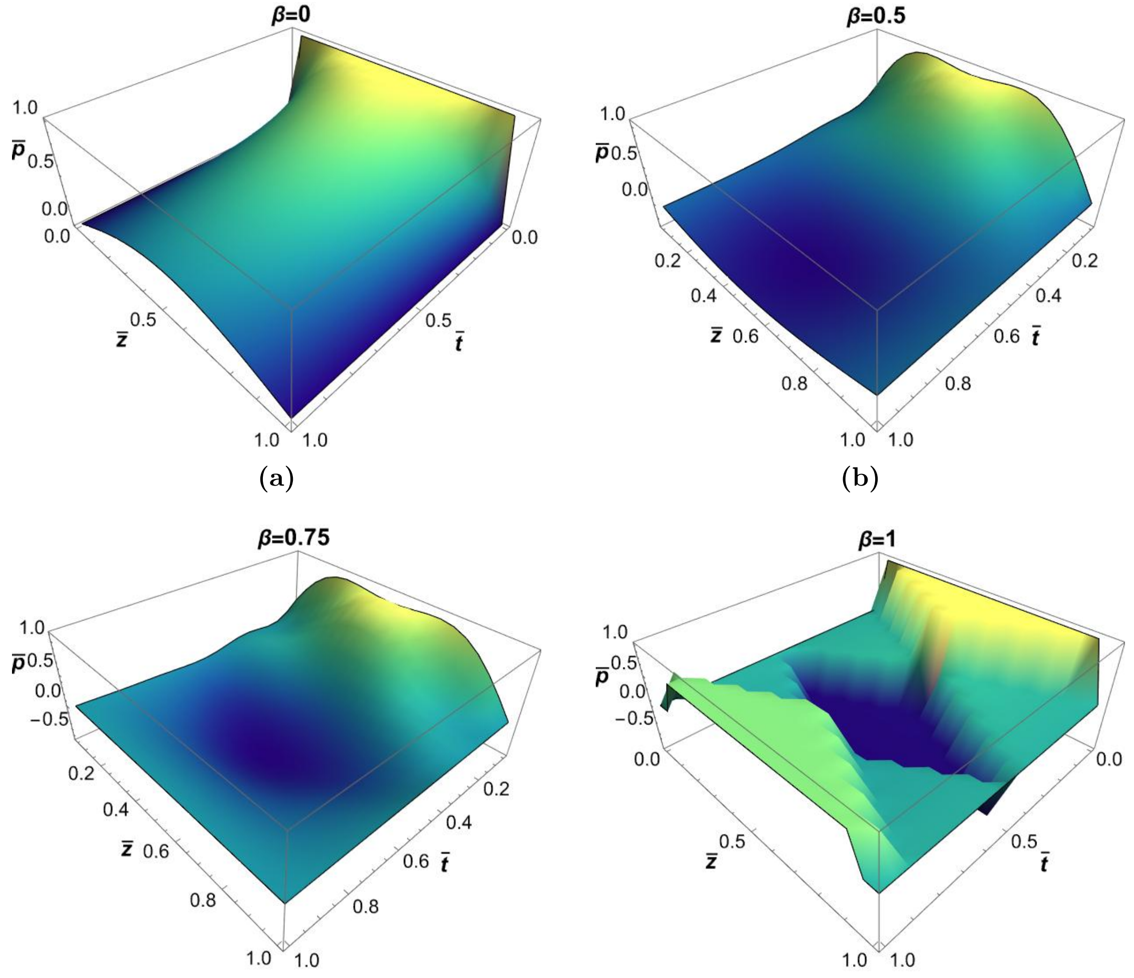

(a) **(b)**

(c) **(d)**

Figure 3.5: *Three-dimensional representation of non-dimensional pressure field $\bar{p}$ for various β values in the fully drained case, particularly: $\beta = 0$ in Figure* ***(a)****, $\beta = 0.5$ in Figure* ***(b)****, $\beta = 0.75$ in Figure* ***(c)****, and $\beta = 1$ in Figure* ***(d)****.*

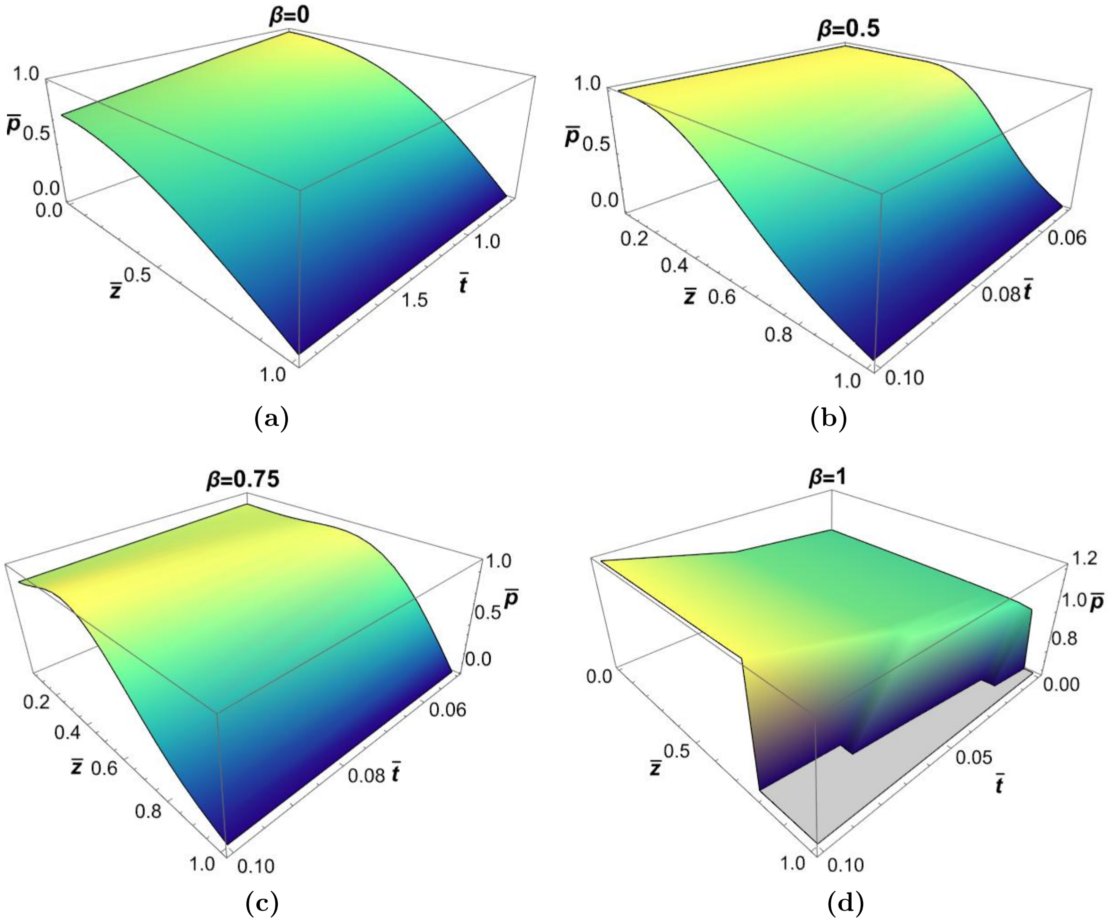

(a) **(b)** **(c)** **(d)**

Figure 3.6: *Three-dimensional representation of non-dimensional pressure field* $\bar{p}(\bar{t},\bar{z})$ *in the confined compression test with variable load for* $\beta = 0$, $\beta = 0.5$, $\beta = 0.75$ *and* $\beta = 1$, *in **(a-d)**, respectively.*

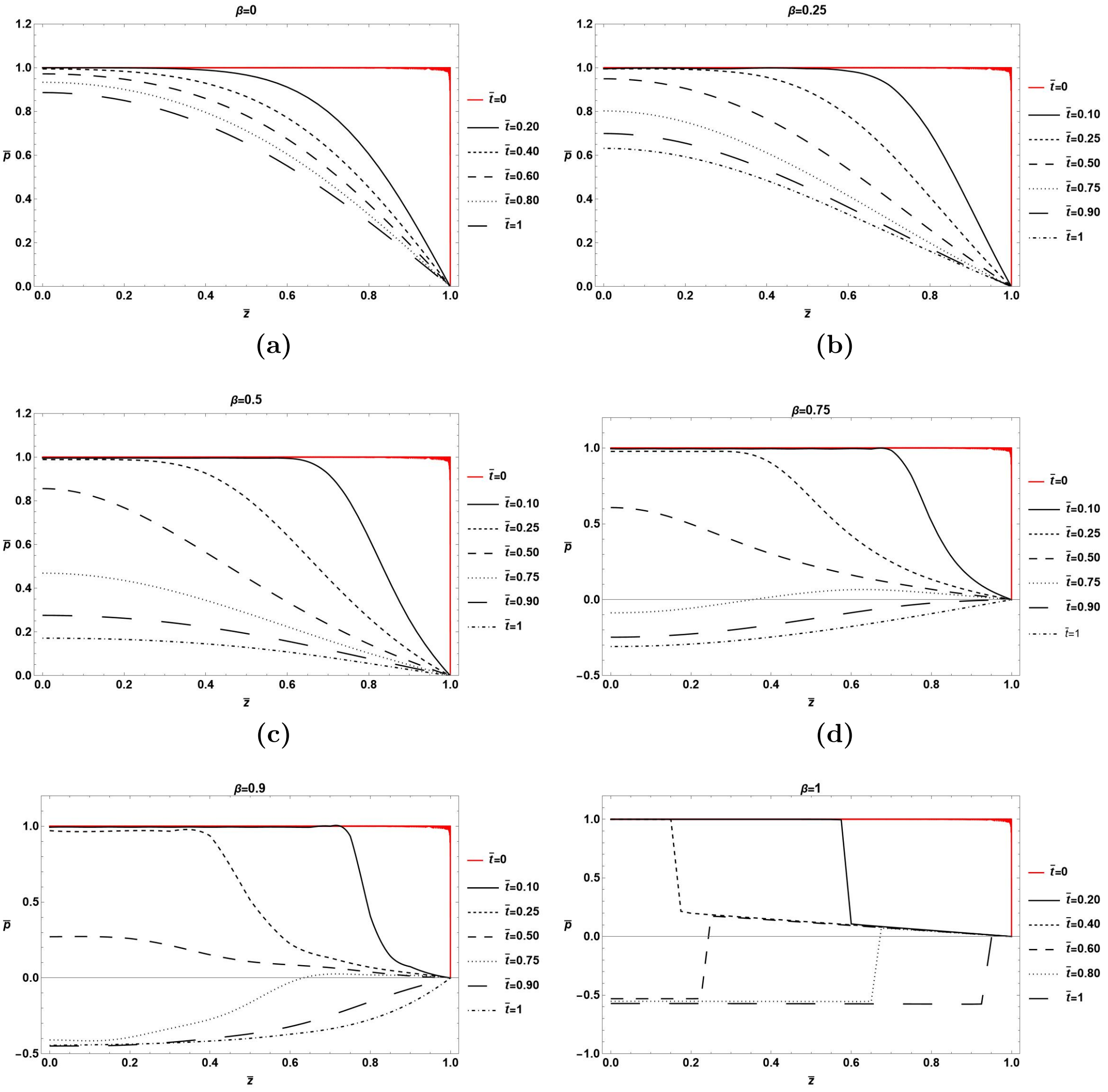

(a) **(b)**

(c) **(d)**

(e) **(f)**

Figure 3.7: *Non-dimensional pressure field* $\bar{p}$ *for different values of* β *in the confined compression test with constant load; particularly* $\beta = 0$ ***(a)***, $\beta = 0.25$ ***(b)***, $\beta = 0.5$ ***(c)***, $\beta = 075$ ***(d)***, $\beta = 0.9$ ***(e)*** *and* $\beta = 1$ ***(f)***. *Each curve represents the pressure field for a specific value of non-dimensional time* $\bar{t}$*; the red-line represents the confined compression test at the initial time, i.e.* $\bar{t} = 0$.

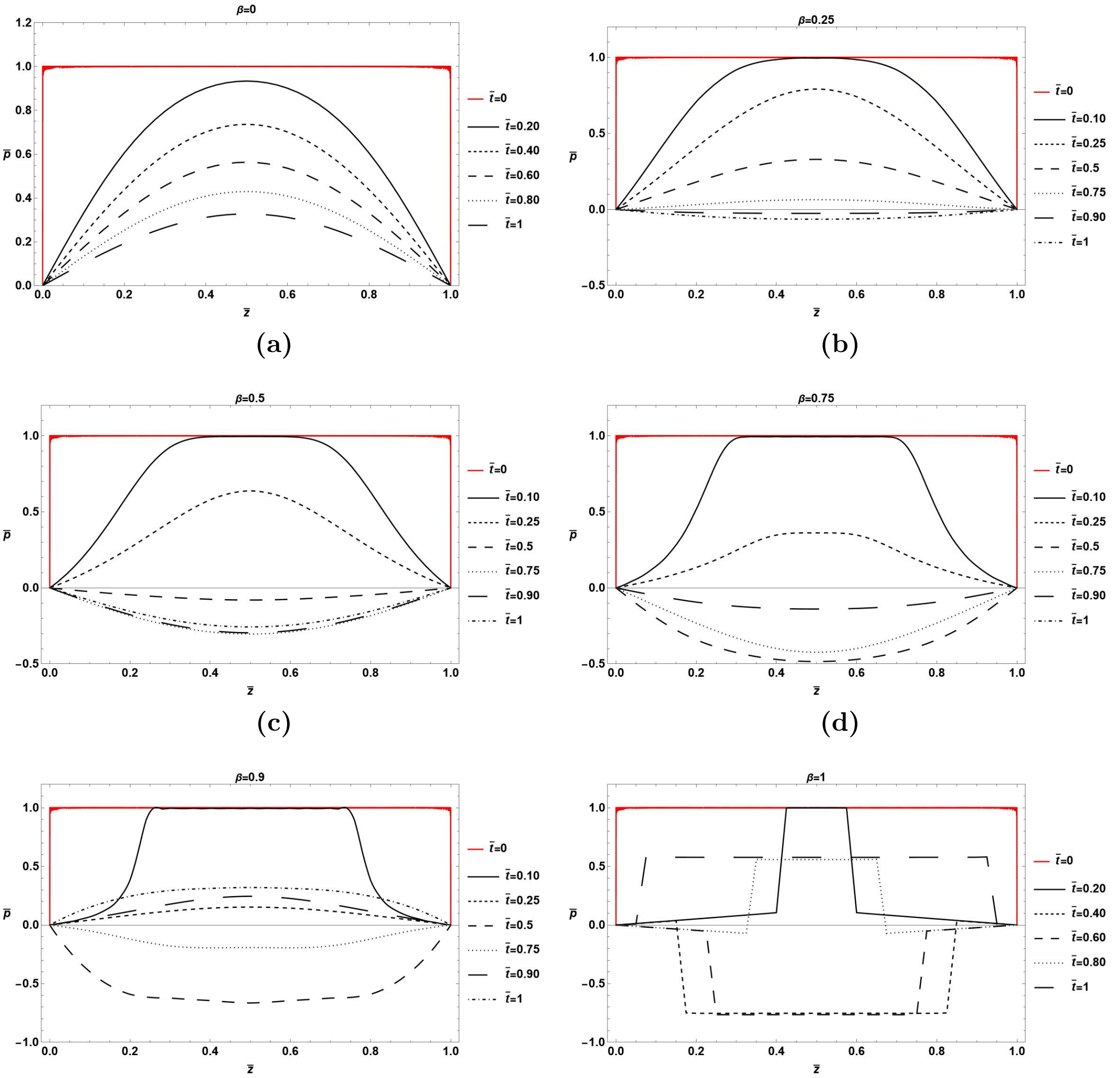

(a) (b)

(c) (d)

(e) (f)

Figure 3.8: *Non-dimensional pressure field $\bar{p}$ for different values of β in the fully drained case, in detail: $\beta = 0$ **(a)**, $\beta = 0.25$ **(b)**, $\beta = 0.5$ **(c)**, $\beta = 0.75$ **(d)**, $\beta = 0.9$ **(e)**, and $\beta = 1$ **(f)**. Each curve represents the pressure field for a specific value of non-dimensional time $\bar{t}$, particularly the red-line represents the confined compression test at the initial time, i.e. $\bar{t} = 0$.*

.

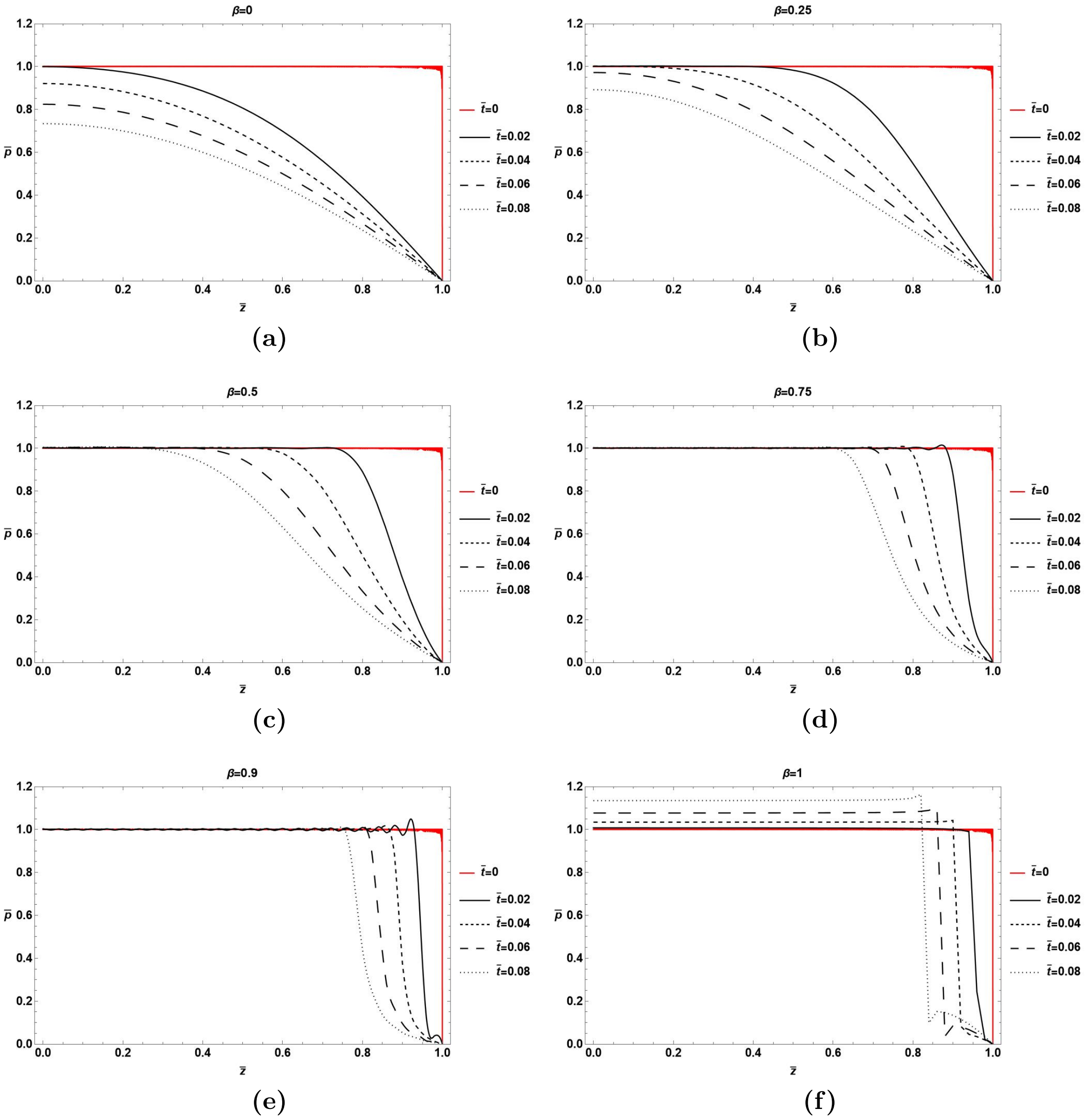

(a) **(b)**

(c) **(d)**

(e) **(f)**

Figure 3.9: *Non-dimensional pressure field* $\bar{p}$ *for different values of* β *in the confined compression test with variable load* $\sigma(\bar{t})$*; particularly* $\beta = 0$ ***(a)****,* $\beta = 0.25$ ***(b)****,* $\beta = 0.5$ ***(c)****,* $\beta = 075$ ***(d)****,* $\beta = 0.9$ ***(e)*** *and* $\beta = 1$ ***(f)****. Each curve represents the pressure field for a specific value of non-dimensional time* $\bar{t}$*; the red-line represents the confined compression test at the initial time, i.e.* $\bar{t} = 0$ *.*

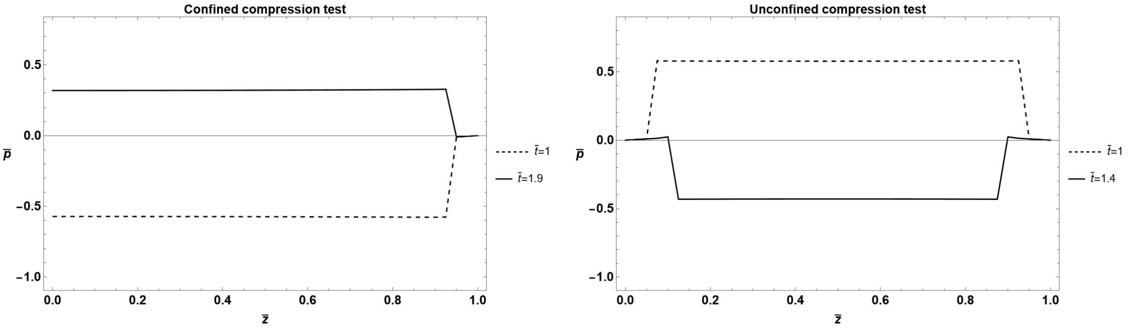

(a) (b)

Figure 3.10: *Comparison of the non-dimensional pressure field* $\bar{p}$ *for* $\beta = 1$ *between the confined case **(a)** and the fully drained case **(b)**, fixing the* $\bar{t}$ *value. In detail, the dotted line is related to* $\bar{t} = 1$*, while the continuous line is related to the time when the pressure reaches the opposite value, i.e. pressure reaches the positive value when* $\bar{t} = 1.9$ *in the confined compression test, and it reaches the negative value when* $\bar{t} = 1.4$ *in the unconfined compression test.*

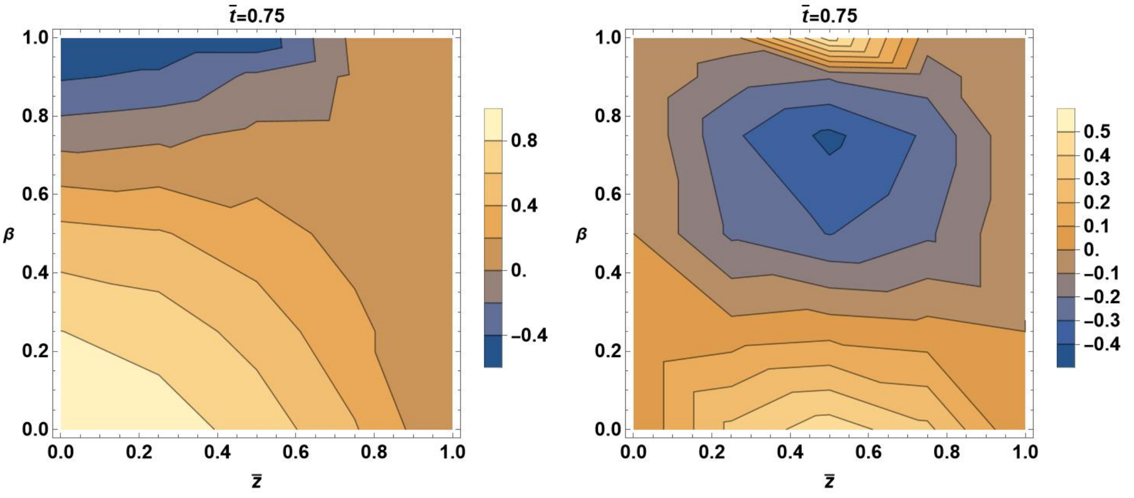

(a) (b)

Figure 3.11: *Comparison of the non-dimensional pressure field* $\bar{p}$ *between the semi-drained case **(a)** and the fully drained case **(b)** under constant load, fixing the value of non-dimensional time* $\bar{t} = 0.75$*.*

Bibliography

[1] Biot M. A., “General Theory of Three Dimensional Consolidation", *Journal of Applied Physics*,vol. 12, 155, **1941**.

[2] Ehlers, W. & Eipper, G. Finite Elastic Deformations in Liquid-Saturated and Empty Porous Solids. *Transp. Porous Media* 34, 179–191 **1999**.

[3] Deseri L., Zingales M., “A mechanical picture of fractional-order Darcy equation”, *Communications in Nonlinear Science and Numerical Simulation*, vol. 20, no. 3, pp. 940–949, **2015**.

[4] Alaimo G., Piccolo V., Cutolo A., Deseri L., Fraldi M., Zingales M., “A fractional order theory of poroelasticity”, *Mechanics Research Communications*, vol. 100, **2019**.

[5] Bologna E., Di Paola M., Dayal K. Deseri L., Zingales M., "Fractional-order nonlinear hereditariness of tendons and ligaments of the human knee".*Phyl. Tran. R. Soc. A: Math. Phys. Eng. Sci.*, 378(2172), 20190220,**2020**.

[6] Maes, J. A., Donahue, T. H. "Time-dependent properties of bovine meniscal attachments: stress relaxation and creep",*Journal of biomechanics*, 39(16), 3055-3061,**2006**.

[7] Bologna E., Graziano F., Deseri L., Zingales M., “Power-Laws heredinariness of biomimetic ceramics for cranioplasty", *International Journal of Non-Linear Mechanics*, vol. 115, pp. 61-67, **2019**.

[8] Deseri L., Di Paola M., Zingale, M., Polacci P. "Power-law hereditariness of hierarchical fractal bones". *International Journal for Numerical Methods in Engineering*, vol. 29 1338–1360, **2016**.

[9] Norberg, C., Filippone, G., Andreopoulos, F., Best, T. M., Baraga, M., Jackson, A. R., Travascio, F. "Viscoelastic and equilibrium shear properties of human meniscus: Relationships with tissue structure and composition", *Journal of biomechanics*, 120, 110343, **2021**.

[10] Camarda L., Bologna E., Pavan D., Morello F., Monachino F., Giacco F., Zingales M., "Posterior meniscal root repair: A biomechanical comparison between human and porcine menisci", *Muscles, Ligaments and Tendons Journal*, 9(1), 76-81, **2019**.

[11] Palumbo F. S., Fiorica C., Pitarresi G., Zingales M., Bologna E., Giammona G., " Multifibrillar bundles of a self-assembling hyaluronic acid derivative obtained

through a microfluidic technique for aortic smooth muscle cell orientation and differentiation", *Biomaterials Sciences*, 6 (9), 2518-2526,**2018**.

[12] Ionescu C., Lopes A., Copot D., Machado J. A. T., Bates J. H. T. "The role of fractional calculus in modeling biological phenomena: A review".*Communications in Nonlinear Science and Numerical Simulation.* 51, 141–159,**2017**.

[13] Carpinteri A., F. M., "Fractals and Fractional Calculus in Continuum Mechanics". *Springer-Verlag Wien GmbH*, **1997**. doi:10.1007/978-3-7091-2664-6.

[14] Nutting P., "A new general law of deformation", *J. Franklin Inst. B*, vol. 191 (5). 679–685, **1921**.

[15] Bologna E., Zingales M., Alotta G. Deseri L.," Quasi-Fractional Models of Human Tendons Hereditariness", *IEEE 4th International Forum on Research and Technologies for Society and Industry, RTSI 2018 - Proceedings*, art. no. 8548419, **2018**.

[16] Caputo M., Plastino W. ," Diffusion in porous layers with memory", *Geophys. Int. J.* vol.158 , 385–396,**2004**.

[17] Caputo M., "Models of flux in porous media with memory," *Water Resour. Res.*, vol. 36, pp. 693–706, Mar.**2000**.

[18] Di Paola M, Pinnola FP." Calcolo frazionario and viscoelasticità". Published online, **2011**.

[19] Capurso, M. Lezioni di Scienza Delle Costruzioni. 1–304 **2006**.

[20] Carpinteri, A. Scienza delle Costruzioni Vol 2. pp 333-384 **1992**.

[21] Pinsky Mark A., "Partial Differential Equations and Boundary-Value Problems with Applications:Third Edition",*Pure and Applied Undergraduate Texts*, Vol. 15; 526, **1998**.

[22] Podlubny I., "Fractional Differential Equations", *Mathematics in science and engineering*, vol.198, **1999**.

[23] Dehghan, M., Manafian, J. & Saadatmandi, A. The solution of the linear fractional partial differential equations using the homotopy analysis method.*Zeitschrift fur Naturforschung - Section A Journal of Physical Sciences*65, 935–949 , **2010**.

[24] Srivastava H.M., Trujillo J.J., et al. , "Theory and Applications of Fractional Differential Equations", *North-Holland Mathematics Studies*, vol. 204, **2006**.

[25] Diethelm K. "The Analysis of Fractional Differential Equations". *Lecture Notes in Mathematics* vol. 2004, **2010**.

[26] Haubold H. J., Mathai A. M., Saxena R. K. "Mittag-leffler functions and their applications". *J. Appl. Math*, 1–51, **2011**.

[27] Gupta I. Sen Debnath, L. "Some properties of the Mittag-Leffler functions". *Integral Transforms and Special Function.* 18, 329–336, **2007**.

[28] Caputo M., Cametti C. "Fractional derivatives in the diffusion process in heterogeneous systems: The case of transdermal patches". *Mathematical Biosciences.* 291, 38–45, **2017**.

Chapter. 4

Scaffold Implementation and Characterization

In this chapter the design and development process of a 3D scaffold for bone regeneration will be exploited, using polymeric materials and a 3D printing technique. At first, we analyzed the viscous encapsulation phenomenon on PLA/PCL blends. The “Viscous encapsulation” phenomenon occurs when two components of the polymer blend have a significant difference in viscosity in the molten state. The polymer with the lower viscosity tends to move, when flowing through a narrow die - such as the extruder nozzle - towards the walls by encapsulating the polymer with higher viscosity[1]. Even though this occurs in any process in which polymers are below their glass transition temperature, these interfacial separated structures and the viscosity imbalance vanish rapidly in a compatible or miscible system owing to the fast inter-diffusion at the micro-level, and thus the intermixing is greatly accelerated. Particularly, the interphase closely depends on the interface microstructure through local entanglements that are gradually established via inter-chain penetration during the inter-diffusion and/or reaction process[2]. Only a few studies have analyzed the viscous encapsulation phenomenon. In most of them, a mathematical model was implemented to explain which forces and factors act during the AM process, focusing on the flow through the nozzle[3, 4, 5]. Several factors can influence this phenomenon, i.e., either polymeric properties (e.g., molecular weight distribution, viscosity, lateral chains) or process parameters (e.g., temperature, shear rate, die geometry, nozzle length/diameter ratio). In detail, the viscosity contrast of two immiscible fluids has been identified as the most important factor in the encapsulation phenomenon; the low-viscosity constituent is in the region of high shear, towards the external region, meanwhile the high-viscosity one is in the opposite region. Here, the lower-viscosity material attempts to encapsulate the higher-viscosity fluid. Naturally, this phenomenon also contributes to the final structure characteristics having unique mechanical, thermal, electrical, or physical properties that can be tailored to the final application [6]. Hence, the properties of these structures are related to the confinement and/or interface effects[7, 8], instead of a continuous multi-layer structure that depends only on the materials’ properties, in which it is not possible to distinguish the phases of each component. Therefore, the related design and manufacturing technologies adopted were also developed over the years to create multi-layer structures, improving classical methods. Specifically, the principal technique used is co-axial AM, which involves the simultaneous deposition of two or more materials with a common longitudinal axis, obtaining a core-shell or a multi-core shell structure [9, 10]. A thorough knowledge of the encapsulation phenomena,

as well as the final properties of the structure, is the main goal of this study. To achieve this, PLA and PCL were used since they are common polymers in biomedical applications [11, 12, 13, 14] for their stable and controllable processing properties, which also play an important role in industrial production. PLA is a thermoplastic aliphatic polyester, known as "green plastic" due to its renewable, biodegradable, and biocompatible characteristics [15], but its brittleness, slow crystallization rate, and low thermal stability usually limit its broader application at a large-scale.
PCL is a biocompatible and biodegradable polyester as well, which exhibits a relatively low glass transition temperature (about -60 °C), a low melting point (about 60 °C), and high flexibility with an elongation at break of about 600% at room temperature [16]. Many studies focused on improving PLA/PCL miscibility, using different strategies, such as the introduction of a new polymer [17, 18], nanoparticles [19, 20], and co-polymers [21, 22, 23]. Among these strategies, blending PLA and PCL is the most versatile and cheapest method in industrial settings to improve PLA toughness, crystallization, and biodegradability [11, 24]. In contrast to what has been done so far, the present research did not try to improve the interaction and, consequently, interdiffusion of PLA and PCL, but to improve their phase separation. Five different PLA/PCL blends were synthesized in the ratio of 10:90, 30:70, 50:50, 70:30, and 90:10, to be processed through 3D printing. Material domains, as well as interphase adhesion, were analyzed through various microscopic techniques to measure the influence of process parameters. The macroscopic properties as mechanical, superficial, biological, morphological, and thermal properties were also investigated, obtaining a detailed overview of the viscous encapsulation phenomenon. These structures are of great interest in biomedical engineering for the design of devices where it is necessary to have structural and therefore chemical properties that change from the core to the shell of the structure. Some of the reasons are:

- Blood vessels: Shell structures can be used to create artificial blood vessels. The core can be made of a biocompatible material, while the shell can be designed to resist mechanical forces and interactions with the bloodstream.
- Controlled drug release devices: shell structures allow the release of drugs to be controlled. The core can contain the drug, while the shell regulates the release over time.
- Scaffolds for tissue regeneration: Shell structures can act as supports for tissue regeneration. The core can provide a three-dimensional structure, while the shell can be designed to promote cell adhesion and growth.

One or more combined techniques are usually adopted to create these structures, such as a fluid deposition method for the core and electrospinning for the shell, or 3D printing with a core-shell nozzle, etc.., requiring more production time, cost and work. Hence, we show an optimization approach toward the advanced design of scaffold microstructures that can be used to regenerate tissues and meet design requirements, overcoming the disadvantages associated with conventional single-material AM techniques to produce core-shell or multicore-shell multi-material structures.
Moreover, as already mentioned in *Chapter 1*, scaffolding structures play a crucial

role in the world of cell interaction, proliferation, and growth. They provide the necessary support and access required for workers to safely and efficiently complete their tasks at various heights. In particular, in the case of bone implants, it is important to ensure that the implants can withstand the increased loads associated with body weight and mobility. For the optimization of bone implant topology, a naturally derived lattice is needed to mimic the function of bone implants. As a result, it is necessary to have two or three areas with different average pore sizes, which results from the need for cell growth in one area and compatible mechanical properties in other parts. this results in the design of cellular structures with a porosity gradient, i.e., Functionally Graded Porous structures (FGPs) for use in prosthetic devices. They offer benefits by meeting both mechanical and biological requirements, avoiding the discontinuity between pore layers, lowering stiffness, and obtaining optimal pore size for osseointegration [25].

Discovered by *Alan Schoen* in 1970, a *Gyroid* is an infinitely connected triple periodic minimal surface. In nature, self-assembled gyroid structures are found in certain surfactant or lipid mesophases [26]. It occurs naturally in polymer science and biology as a high surface area interface. Meanwhile, in biomedical research, gyroid structures are suitable for bone tissue engineering applications, as they can mimic the porosity of the inner part of bone [27]. Similarly, a *Voronoi structure*, also known as a Voronoi diagram, is a mathematical concept used in various fields, including science, technology, and visual art. It's a partition of a plane into regions close to each of a given set of objects. In the simplest case, these objects are just finitely many points in the plane (called seeds, sites, or generators). For each seed, there is a corresponding region, called a Voronoi cell, consisting of all points of the plane closer to that seed than to any other. Due to these properties, a Voronoi structure is considered a good selection as it resembles the interior trabecular structure; moreover, the porosity and interconnectivity of Voronoi-based designs can be beneficial for cell growth and nutrient diffusion [28, 29]. So, the approach within this thesis applies Laguerre-Voronoi and Gyroid tessellation to create various structures with controlled pore size distribution in the whole structure. In detail, the classical 00-90° structure, as well as a 00-45° structure, and two different Gyroid and Voronoi structures were considered for a *Finite Element Method* (FEM) analysis.

After establishing the best scaffold-performing configuration, a promising, low-cost, and environmentally friendly bio-material was synthesized to overcome the most important weaknesses of PCL, such as high hydrophobic and low elasticity, using non-petroleum-based blends. *CA* is an organic compound that occurs in various fruits and vegetables. Biomaterials cross-linked with CA have advanced in-vitro and in vivo material properties that make them suitable for various biomedical applications [30, 31, 32]. So, biopolymers of CA were used to increase the long degradation time and low elasticity of PCL [33, 34, 35, 36, 37]. Most importantly, a combination of *Starch* and CA has shown biocompatibility, heterogeneous nucleation of Hap crystals, appropriate pores for increasing oxygen permeability and nutrient supply to deeper regions [38], and enhancement of barrier property [39]. Starch is the second most abundant biopolymer after cellulose and one of the low-cost polysaccharides, widely present in green plants and every type of tissue [40]. It has been studied as an interesting alternative to partially replace petroleum derivatives due to its ability to increase the rate of biodegradation, which is already widely exploited by the plastics industry [41]. However, due to the limitations of native starch, such as insolubility in cold water, and limitations of breaking down when reheated or treated in acidic environments, various physical, chemical, and enzymatic modifications have been explored to improve the functional properties of starch and facilitate its application for different purposes. *Glycerol* is the most used to increase its plasticity, filler-matrix interaction, as well as thermal and mechanical behavior [42, 43, 44].

This research aims to develop a new biomaterial with appropriate physical, chemical, and mechanical properties by exploiting the advantages and synergistic properties offered by starch, CA, PCL, and glycerol. So, a blend of Starch and CA was first made and then mixed to PCL in different ratios; the same blends were also made with 18%wt glycerol content. A 3D printer was used as AM technique since It has multiple assets, including precision of deposition, cost-effectiveness, simplicity, and controllability of cell distribution, compared to other techniques such as electrospinning, already used in other researchers' groups [36, 37]. The obtained scaffolds were further characterized by mechanics, thermal, physical, and morphological analysis, comparing the results to the pure material. In detail, different Starch, CA, Glycerol, and PCL blends have been elaborated, while PCL was used as reference material. The mixtures were prepared using a combination of two different polymer emulsion reactions: first the mixtures of SC and SGC were made, and then they were blended with PCL, named SC/PCL and SGC/PCL. In detail, six different blends were synthesized in the ratio of 10:90, 30:70, and 50:50, to be processed through 3D printing. Nevertheless, the thermal, physical, chemical, and mechanical characteristics of each blend and pure material were further investigated in this research.

These new blends showed good printability but also a significant improvement in PCL properties, in terms of mechanical properties, thermal stability, and hydrophilicity. Thus, as a valid and competitive substitute, SC/PCL or SGC/PCL could be adopted in all PLA/PCL applications, such as a biomedical field or packaging application, as its valid and competitive substitute. Furthermore, future trends and potential clinical translations will be discussed.

4.1 Materials and Methods

4.1.1 Materials

PCL (product number 440744, 80kDa, MFI 2.01 - 4.03 at 160°C/5kg, 1.145 g/mL at 25 °C), Citric Acid ($\geq$ 99.5%), and Glycerol (G9012) were purchased from Sigma-Aldrich, as well as Ethanol (EtOH), Tetrahydrofuran (THF), Acetic Acid (AA, $\geq$ 99.8%), and Formic Acid (98-100%), while PLA (Ingeo™ 3052D, MFR 14 g/10 min at 210°C/ 2.16kg, Relative Viscosity 3.3) from NatureWorks® LLC and Starch (S9765) from Merck Group. These products were used during the polymeric emulsion process for the blend synthesis.

4.1.1.1 Preparation of PLA/PCL samples

Five blends of PLA/PCL in the ratio of 10:90, 30:70, 50:50, 70:30, and 90:10 (w/w), named PLA10/PCL90, PLA30/PCL70, PLA50/PCL50, PLA70/PCL30, and PLA90 /PCL10, respectively, were synthesized using the following protocol. PLA and PCL pellets were oven-dried for 4h at 80°C, weighted, mixed in selected ratios into THF (in the ratio solute/solvent of 10/90 w/v), and stirred (200 rpm) for $24h$ at room temperature. Subsequently, a polymer "paste" of each blend was obtained through solvent extraction in EtOH and left to evaporate overnight. Finally, it was cut into small pellets, as summarized in *Figure 4.1*.

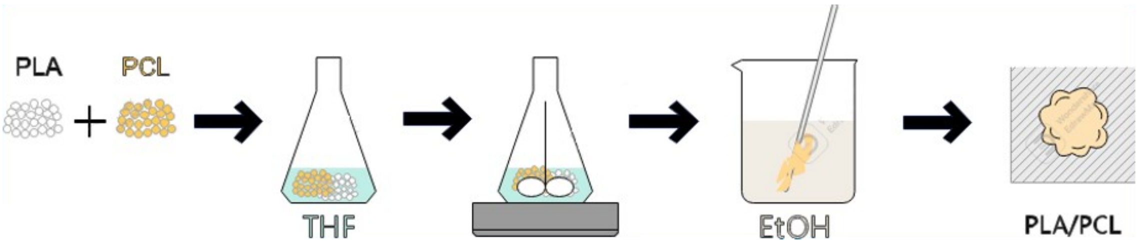

Figure 4.1: *Process scheme followed for PLA/PCL blends synthesis.*

After that, multi-layer scaffolds of each PLA/PCL blend were printed using a pneumatic-driven AM system (Bioscaffolder SYSENG) at 4 bar and with a G22-needle (∅.41 mm), while other process parameters were optimized for each blend, as reported in *Table 4.1*.

Table 4.1: *Process parameters used for each blend in different ratios into the 3D printer Bioscaffolder Syseng.*

Polymer Blends	**Temperature** [°C]	**Extrusion Speed** [mm/min]	**Pre-Flow** [s]	**Post-Flow** [s]	**Screw Speed** [rpm]	**Pullback Retraction** [R/s]
PLA10/PCL90	170	120	2.0	0.5	30	0.5
PLA30/PCL70	170	100	3.0	1.0	10	3.0
PLA50/PCL50	190	160	1.5	0.0	25	1.0
PLA70/PCL30	170	130	1.5	1.0	20	0.5
PLA90/PCL10	180	100	2.5	1.5	20	0.5

All scaffolds had a strand distance of 1 mm a layer thickness of 0.325 mm, and a 0°/90° structure in both rectangular (9 × 9 mm) and cylindrical shape (6 × 6 mm), as shown in *Figure 4.2*.
Furthermore, four different needles were employed, namely G22 (∅.41 mm), G28 (∅.18 mm), G30 (∅.15 mm), and G32(∅.10 mm), at 170°C to print scaffolds using PLA10/PCL90. Needles parameters, as well as process parameters for this blend, were reported in *Table 4.2*.

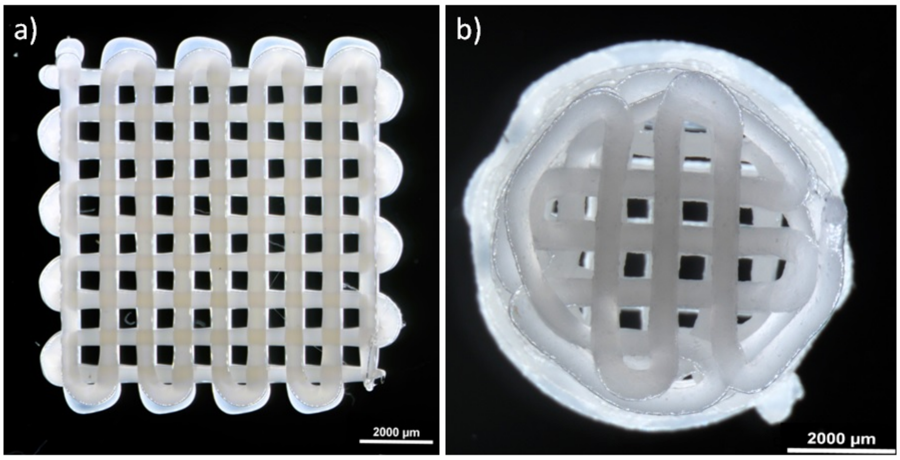

Figure 4.2: *Stereomicroscopy image of PLA50/PCL50 scaffold printed by Bioscaffolder SYSENG into two different shapes: PLA50/PCL50 scaffold in rectangular shape* ***(a)*** *and in cylindrical shape* ***(b)****; scale bar of 2000µm.*

Table 4.2: *Process parameters used to print PLA10/PCL90 scaffolds with different needle diameters.*

Needle-type	**Length/ Diameter** [L/D]	**Strand Distance** [mm]	**Extrusion Speed** [mm/min]	**Pre-Flow** [s]	**Post-Flow** [s]	**Screw Speed** [rpm]	**Pullback Retraction** [R/s]
G22	15.71	1.00	120	2	0.5	7	0.5
G28	35.84	0.77	100	4	0.5	25	0.5
G30	41.97	0.75	150	1.75	0.5	35	0.5
G32	62.55	0.70	150	1.75	0.5	30	1

4.1.1.2 Preparation of Starch/Citric Acid/PCL and Starch/Glycerol/ Citric Acid/PCL samples

Preparation of Starch/CA (SC) was based on the method of Saliu et al[39]. with some modifications. Briefly, Starch (2 gr) was added to 20 mL of distilled water and heated at 90 °C into a magnetic stirring (<200 rpm) for 30 min. The resulting slurry was firstly frozen at $-20°C/min$ overnight and then freeze-dried for 5 days to facilitate gelatinization. Thereafter, it was soaked into a solution of CA (3 gr) and EtOH (10 mL), and conditioned for 16 h at room temperature into a magnetic stirring (<100 rpm). The obtained suspension was filtered and washed with EtOH to remove CA excess. The final SC powder was then collected. A schematic representation of the resulting protocol is reported in *Figure 4.3.*

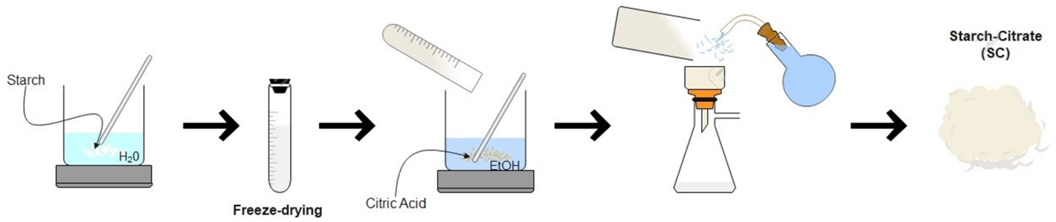

Figure 4.3: *Process scheme for Starch-Citric Acid (SC) blends synthesis.*

Similarly, Starch, Glycerol, and CA (SGC) were blended adding 18wt% of Glycerol into the first step of the previous protocol and soaking the freezer-dryer paste in EtOH (70%) for 2 days to leach out the sugar, as shown in the process scheme in *Figure 4.4*. After that, the same steps illustrated in the previous protocol were done.

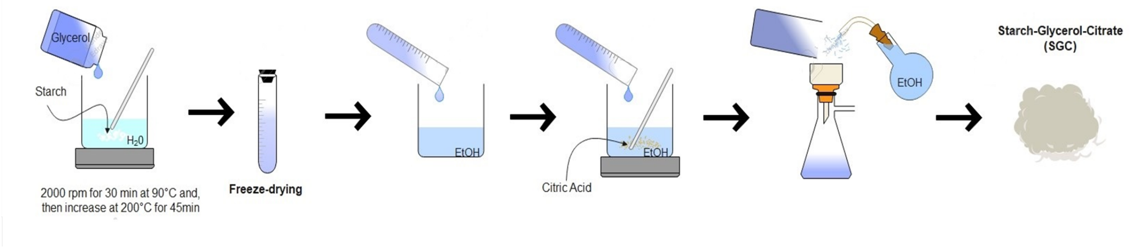

Figure 4.4: *Process scheme for Starch-Glycerol-Citric Acid (SGC) blend synthesis.*

Six blends of SC/PCL and SGC/PCL in the ratio of 10:90, 30:70, and 50:50 (w/w) named respectively SC10/PCL90, SGC10/PCL90, SC30/PCL70, SGC30/PCL70, SC50/PCL50, and SGC50/
PCL50 were synthesized using the following protocol. SC and SGC powders and PCL pellets were weighted and mixed in selected ratios into a solution of Acetic Acid and Formic Acid in the ratio solute/solvent of 10/90 w/v, and stirred (100 rpm) for 24h at 40°C. So, a polymer "paste" of each blend was obtained through a solvent extraction in EtOH. The EtOH solution was also filtered to collect any traces left in the solution. All blends have been left to evaporate overnight before being cut into small pieces.

Multi-layers scaffolds of each SC/PCL and SGC/PCL blend were printed using a pneumatic-driven AM system (Bioscaffolder SYSENG) at 4 bar and with G22-needle (∅.41 mm), while other process parameters were optimized according to each blend, as reported in *Table 4.3*. Printed scaffolds had a strand distance of 1 mm, a layer thickness of 0.325 mm, and a 0°/90° structure in cylindrical shape (6×6 mm), as shown in *Figure 4.5*.

Table 4.3: *Process parameters used for SC/PCL and SGC/PCL blend in different ratios into the 3D printer Bioscaffolder Syseng.*

Polymer Blends	**Temperature** $^{\circ}C$	**Extrusion Speed** [mm/min]	**Pre-Flow** [s]	**Post-Flow** [s]	**Screw Speed** [rpm]	**Pullback Retraction** [R/s]
SC10/PCL90	135	200	0.3	0.3	30	0.0
SGC10/PCL90	130	360	0.7	0.0	30	0.0
SC30/PCL70	135	420	0.0	0.0	30	0.5
SGC30/PCL70	130	360	0.6	0.1	30	0.0
SC50/PCL50	135	360	0.7	0.0	30	0.0
SGC50/PCL50	-	-	-	-	-	-

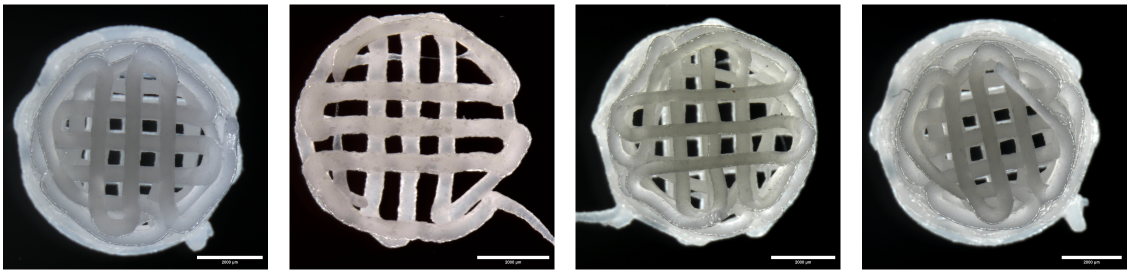

(a) **(b)** **(c)** **(d)**

Figure 4.5: *Stereomicroscopy scaffold image, printed by Bioscaffolder SYSENG into a cylindric shape of* ***(a)*** *SC10/PCL90,* ***(b)****SGC10/PCL90,* ***(c)*** *SC30/PCL70 and* ***(d)*** *SGC30/PCL70; scale bar of 2000µm.*

4.1.2 Characterization of PLA/PCL Scaffolds

4.1.2.1 Rotational Rheometer

PLA and PCL samples were prepared to be analyzed in a rotational rheometer by compression molding at 190°C with a pressure of 200 bar between two Teflon films to obtain a smooth surface and then cut into round disks with a diameter of 20 mm. Dynamic rheological measurements of neat polymers were performed using a stress-controlled rotational rheometer, Discovery HR-2 (Discovery Hybrid Rheometer, TA instrument) with a parallel-plate (20 mm) at 190°C under nitrogen flow.

4.1.2.2 Differential Scanning Calorimetry (DSC)

Small powder-like pieces of each blend were used for DSC experiments (DSC 250, TA instrument) using nitrogen as a purge gas. The samples were initially kept at 20°C for 10 minutes and then heated to 250°C and cooled down to the initial temperature at a rate of 10°C/min. A second heating/cooling cycle was performed with the same temperature range and speed. Thanks to DSC, the enthalpy of melting and enthalpy of cold crystallization were obtained, which were used to estimate the degree of crystallinity X_c.

The relation (4.1) was used to calculate X_c after heating to a temperature just below the melting endotherm:

$$X_c[\%] = \frac{\Delta H_m}{\Delta H_m^0 \cdot \Phi_{PLA}} \times 100 \tag{4.1}$$

where ΔH_m and Φ_{PLA} are respectively fusion enthalpy obtained during the DSC heating process and weight fraction of PLA; while, ΔH_m^0 is the heat of fusion defined as the melting enthalpy of 100% crystalline PLA, which is 93 Jg^{-1} [45]. Consequently, to calculate the degree of crystallinity of the original sample X_c^*, it is necessary to subtract the heat associated with the cold crystallization exotherm (ΔH_{cc}) from the melting endotherm, with the following equation [11, 46]:

$$X_c^*[\%] = \frac{\Delta H_m - \Delta H_{cc}}{\Delta H_m^0 \cdot \Phi_{PLA}} \times 100 \tag{4.2}$$

Here, the melting points were identified as a maximum of the melting endotherms.

4.1.2.3 Scanning electron microscopy (SEM)

For Scanning Electron Microscope (SEM) analysis, PLA/PCL scaffolds were frozen in liquid N2 and cut with a razor blade perpendicularly to the sample height. After that, the obtained samples were sputter-coated with gold (*Cresignton 108 Auto*) and imaged on a microscope (*Jeol JSM-IT200 InTouchScope*) under both secondary and back-scattered electrons with an acceleration voltage of 10 keV.

4.1.2.4 Trasmission electron microscopy (TEM)

The cross-section morphology of the PLA50/PCL50 scaffolds was examined in an FEI/Tecnai G2 Spirit BioTWIN Transmission Electron Microscopy (TEM) operating at a typical accelerating voltage of 80 keV. Samples were embedded on Epon LX112 resin (Hexion) and slowly cured at room temperature for 2 days. Blocks were then sliced on an ultra-cryo microtome Leica EM FC6 at temperatures of $-100°C$ and $-45°C$ for the chamber and the knife, respectively. The samples were collected on TEM carbon-supported Cu grids from the 60% DMSO bath.

4.1.2.5 Polarized Light Microscopy (PLM)

The isothermal phase separation was evaluated from a series of Polarized Light Micrographs (PLM). The data were collected with an inverted Nikon Ti-S/L100 microscope equipped with a Nikon DS-Ri2 color camera, a Lumer Sola SE II for fluorescence, and a CoolLED pE100 system for diascopic white light. In detail, neat polymer and PLA50/PCL50 scaffolds were embedded in an Optimal Cutting Temperature (OCT) compound before cryosectioning. Thin 10µm sections of each sample were cryosectioned, using the Kawamoto tape method [47], and observed in the microscope using transmitted polarized light. OCT was fixed at $-18°C$, except for the sectioning of PLA, for which we decreased the optical temperature to $-22°C$. The samples were washed in Phosphate-buffered saline (PBS) and embedded using a droplet of DAKO mounting medium. For microscopy, we made an overview image at 4×, and detailed images at 20× into the fibers' cross-section.

4.1.2.6 Dissolution Test

The phase separation into the cross-section's surfaces of the samples was also etched with Acetic Acid (AA) at room temperature to dissolve only the PCL phase in the samples containing 50% of PCL w/w [48], using a solute/solvent ratio of 5/95 w/v. Particularly, PLA50/PCL50 scaffolds were extracted at time points of 2, 4, 6, 8, 10, and 12h, and left to dry for 24h at room temperature. Finally, the morphology was investigated by using SEM.

4.1.2.7 Mechanical Test

The mechanical characteristics were evaluated using an MTS Hydraulic testing machine (model LVDT, Italsigma s.r.l., Forlì, Italy) equipped with a 20kgf load cell (HBM-U2B/20kgf). Cylindrical scaffolds of each blend were compressed at 0.04mm/sec until a maximum of 45-50% strain. The compression modulus was defined as the slope of the linear fit according to the stress-strain curve over 0–5% strain [46]. Therefore, all uni-axial compression tests were performed both in wet and dry conditions, under ambient conditions (temperature $25-28°C$ and relative humidity 20–50%). More specifically, samples were soaked into saline solution until complete cover for 5 days before testing for wet conditions.

4.1.2.8 Statistical Analysis

An ANOVA analysis of the collected data was carried out using *software* R. In particular, the compression moduli obtained from the mechanical tests were used to identify a trend in mechanical responses, comparing compositions and conditions. Thereafter, multiple comparison tests (independent T-tests) with Bonferroni correction were subsequently performed to identify which specific combinations of PLA and PCL were significantly different. The compression test was repeated five times for each PLA/PCL blend and each condition, for a total of 50 samples. The mean values as well as the standard deviation of each blend were also calculated.

4.1.2.9 Design of open-porous structures

Six open-porous structures were realized for the FEM analysis. In detail, a simple CAD of 00-90° and 00-45° structure were realized by *Solidworks* (version 2022 Dassault, MA, USA), while a Gyroid and Voronoi structure was made by *nTop* (nTopology Inc.) software. The realized structures are shown in *Figure 4.6.*
In detail, the Laguerre-Voronoi tessellation (LVT) method was used to generate two Voronoi models. The discriminatory feature of the virtual models created is the seed points and the fiber's thickness on nTop. Based on these parameters, the fibers that create the porous structure are then generated. Therefore, a set of random points was adopted in the mid-region of a cube ($6 \times 6 \times 6\ mm$), with $0.3mm$ of fiber thickness. Then, a constant spacing of $0.9mm$ and a random seed of 8 was used for one model, named *V_ cost*, while a ramp point spacing, i.e. from 0.6 to $1.2mm$, and a random seed of 2 was adopted for the second one, named *V_ ramp*. Consequently, *V_ cost* has a constant and homogeneous distribution of fibers, and consequently of pores, along the structure, while the *V_ ramp* has a gradient of porosity from the

inside to the outside part of the structure, as shown in *Figure 4.7*.
Similarly, a walled Triply Periodic Minimal Surfaces (TPMS) cell was used as a unit cell to create the Gyroid structure. The TPMS is composed of infinite, non-self-intersecting, periodic surfaces in three principal directions, named U, V, and W on nTop. According to these directions, there are six possible combinations, but only the UVW orientation was adopted for Gyroid structures. Then, two different frames were used, i.e.: one perpendicular to the bounding box and another turned to 45, called respectively *G:00-90°* and *G:00-45°*, as shown in *Figure 4.8*. The thickness of fiber diameters is approximately $0.2mm$.
All scaffolds have been supported by two boxes of ($6 \times 6 \times 2$ mm) on top and $6 \times 6 \times 1$ mm on the bottom and tested by *Static Analysis* on nTop, simulating the configuration of the compression test. The support structures were created on top and bottom of each scaffold to minimize the deformation of surfaces parallel and guarantee the contact between the structures.

4.1.2.10 Porosity

For each of the six designs, total volume (V_{tot}), mass volume (V_m), and equivalent pore volume (V_p) were estimated based on the model geometries by nTop. Similarly, pore size was determinate according to nTop function called "*Lattice Pore Size* ^{BETA}". Meanwhile, the porosity (P) was calculated using the following equation:

$$P[\%] = \frac{V_{tot} - V_m}{V_{tot}} \times 100 \tag{4.3}$$

and considering a density of $1.3g/cm^3$.

4.1.2.11 FE analysis

Mechanical simulations on six scaffold structures were performed using nTop. In this investigation, a finite element (FE) model was presumed to be isotropic, homogeneous, and linear for every structure. Tetrahedral elements were used for all the structures. In detail, the *S:00-90°* and *S:00-45°* had a total of 1.072.739 and 1.043.384 elements. Meanwhile, the *G:00-90°*, *G:00-45°*, *V_cost* and *V_ramp* designs consisted of 1.261.448, 1.253.718, 1.733.798, and 2.013.868 elements, respectively. Considering a PLA50/PCL50, Young's modulus and Poisson ratio were considered constant for all the designs at *23.41 MPa* and *0.4*, respectively.
The boundary conditions were consistently set in a *Static Structural Analysis* on nTop. Briefly, to imitate a compressive test, faces-loads were applied on top-box elements with forces of $F_z = -500N$, while a fixed displacement on the x, y, and z-axes was set for the bottom-box so that it was completely constrained to the bottom of the plate. Moreover, a structural bonded contact type was employed for the scaffold-boxes interface during the FE analysis. As an example of the configuration set-up for FE analysis, *Figure 4.9* shows the boundary conditions of the model on *S:00-90°* structure.
Due to its printability already shown in the previous subsection, the *S:00-90°* structure was also considered as the standard configuration for the FE analysis.

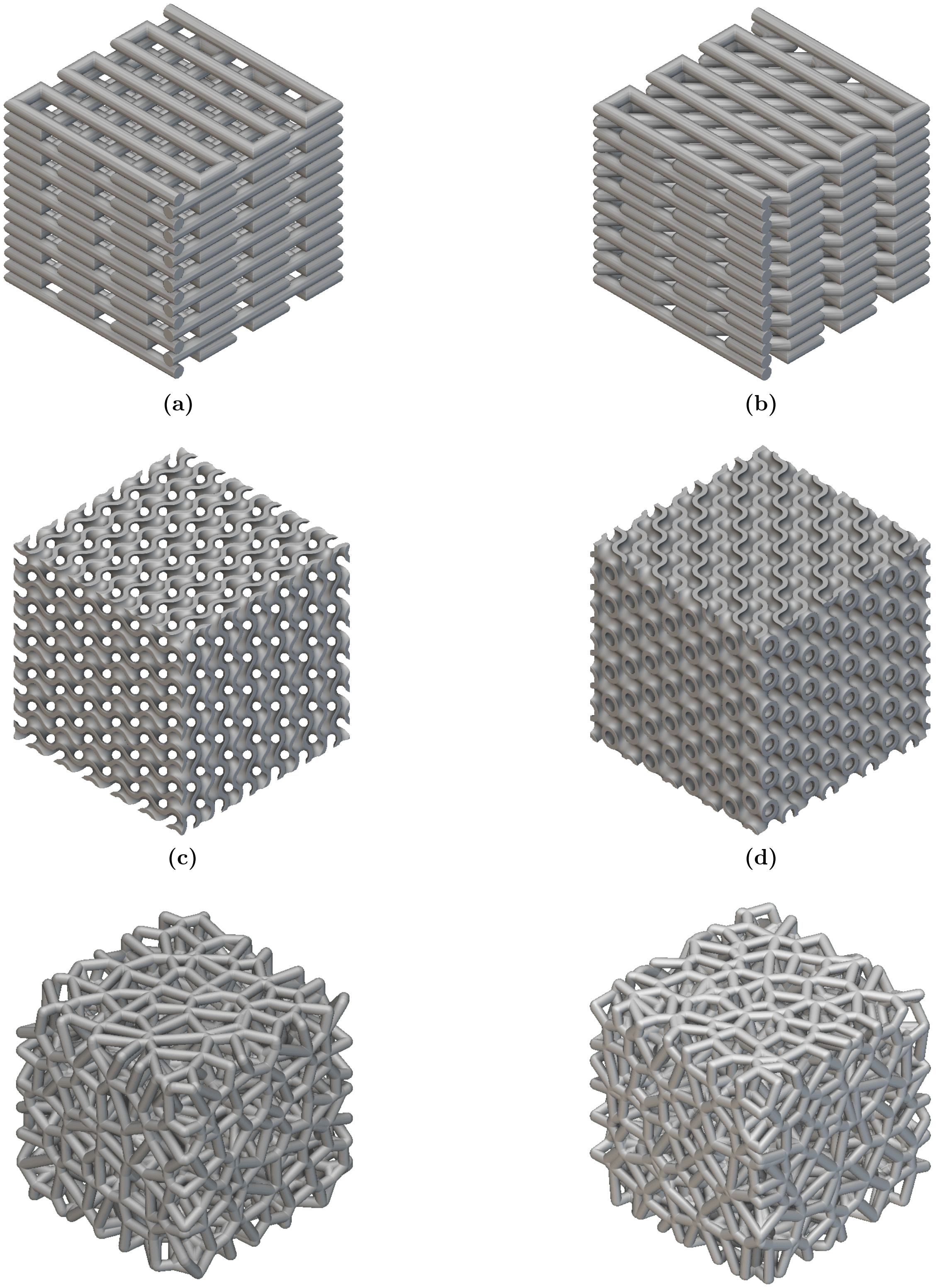

(a)

(b)

(c)

(d)

(e)

(f)

Figure 4.6: *CAD image of scaffold structure made by Solid Works and nTop, into a shape of* ***(a)*** *00-90°,* ***(b)*** *00-45°,* ***(c)*** *Gyroid 00-90°,* ***(d)*** *Gyroid 00-45°,* ***(e)*** *Voronoi with constant point spacing and* ***(f)*** *Voronoi with a gradient point spacing.*

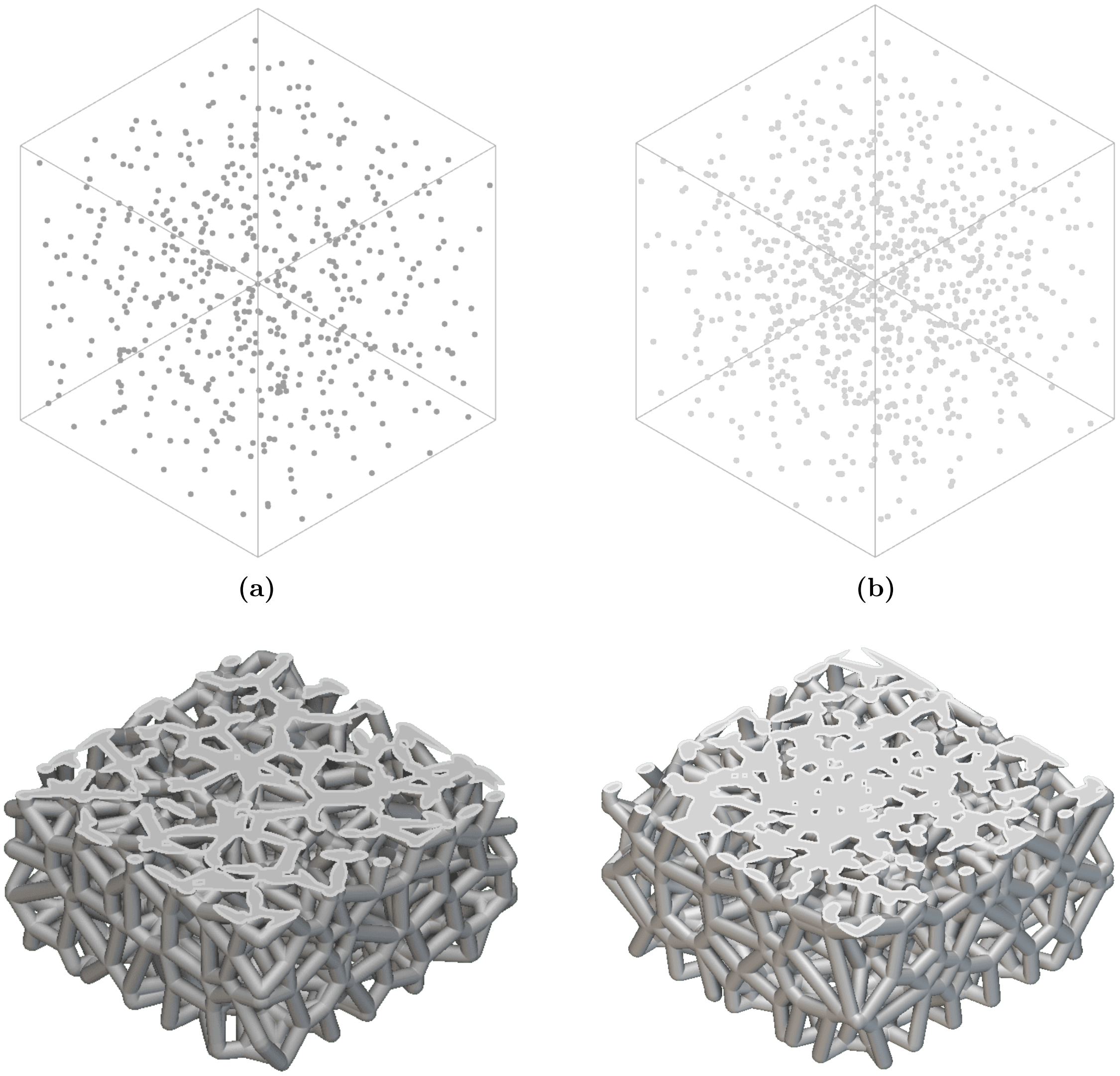

(a) **(b)** **(c)** **(d)**

Figure 4.7: *Distribution of random seed and section of CAD structure with a constant seed points spacing in figure* ***(a)*** *and* ***(c)****, and variable point spacing in figure* ***(b)*** *and* ***(d)*** *made by nTop for Voronoi tessellation.*

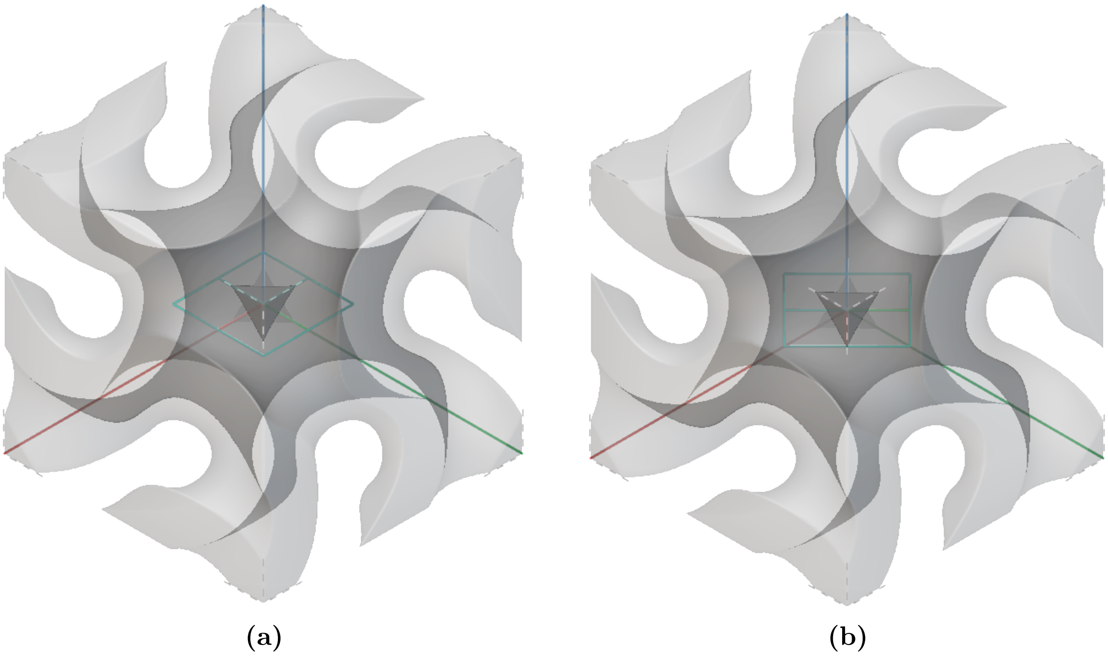

Figure 4.8: *Unit Cell made by nTop to build the Gyroid structure with a perpendicular frame in figure* ***(a)****, and a frame inclination of 45° respect to UVW axes in figure* ***(b)*** *.*

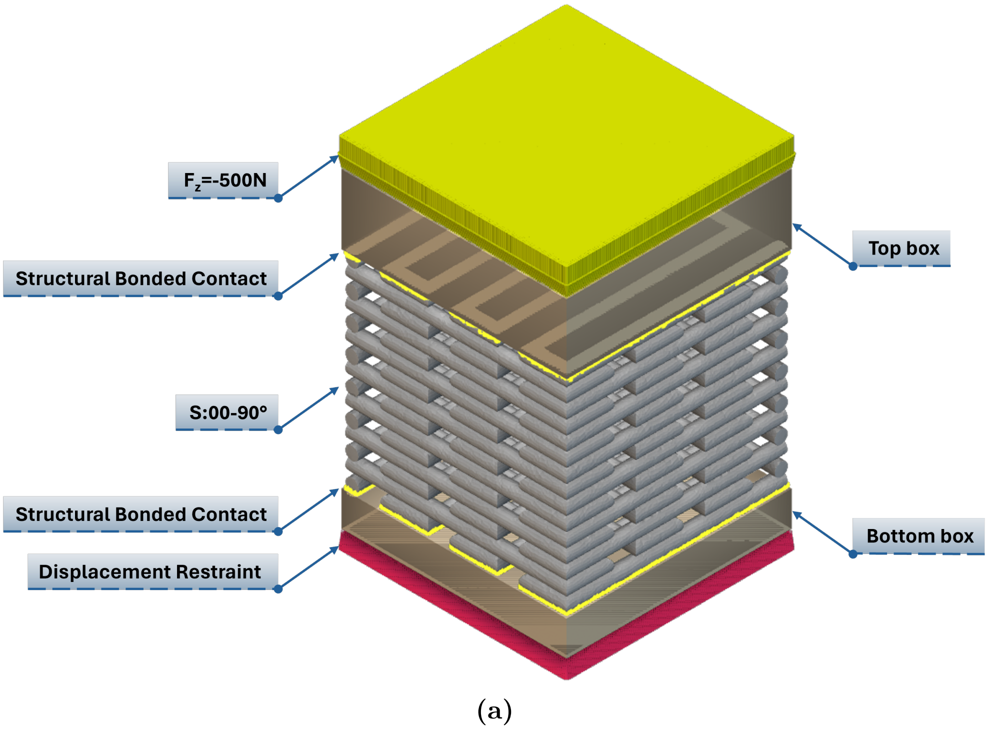

Figure 4.9: *Schematic representation of Boundary Conditions used for S:00-90° structure on nTop for FE analysis.*

4.1.3 Characterization of SC/PCL and SGC/PCL Scaffolds

4.1.3.1 X-Ray Diffraction (XRD)

XRD measurements were carried out on a few powders of pure materials and SC/PCL, SGC/PCL blends using an X-ray diffractometer (Bruker D2 Phaser) equipped with a Ni-filtered CuKα radiation source with a wavelength of $1.542°A$. The measurements were operated at 40 kV and 40 mA with scan angles from 5° to 40° and a scan rate of $3°/min$.

4.1.3.2 Fourier transform infrared spectroscopy (FTIR) Analysis

The Fourier transform infrared spectroscopy (FTIR) spectra were determined using some powders of pure materials and SC/PCL, SGC/PCL blends in FTIR spectroscopy (model Nicolet IS50). The spectra were recorded in the range of $4000–400cm^{-1}$.

4.1.3.3 Thermogravimetric Analysis (TGA)

Thermogravimetric analyses (TGA) were carried out with a Mettler Thermogravimetric Analyzer (TGA550, TA instruments). The measurements were performed on 4–5 mg of SC/PCL and SGC/PCL blend pieces, placed in the platinum pan, from $25°C$ to $700°C$ at a heating rate of $10°C/min$, in a nitrogen atmosphere with a nominal gas flow rate of 30 mL/min. For each composition, the thermogravimetric tests were performed in duplicate.

4.1.3.4 Differential Scanning Calorimetry (DSC)

The thermal analysis on each blend and pure PCL was performed on DSC (DSC 250, TA instrument) using nitrogen as a purge gas. The samples were initially kept at $-20°C$ for 10 min and then heated to $210°C$ and cooled down to the initial temperature at a rate of $10°C/min$. A second heating/cooling cycle was performed with the same temperature range and speed. Through DSC analysis, relation (4.4) was used to calculate X_c:

$$X_c(\%) = \frac{\Delta H_m}{\Delta H_m^0 \cdot \Phi_{PCL}} \times 100\% \tag{4.4}$$

where ΔH_m and Φ_{PCL} are respectively fusion enthalpy obtained during the DSC heating process and weight fraction of PCL in the sample; while, ΔH_m^0 is the heat of fusion defined as the melting enthalpy of 100% crystalline PCL, which is 139.5 Jg^{-1} [34]. For each composition, the DSC analysis was performed in triplicate.

4.1.3.5 Contact Angle Measurements

A few grains grams of each blend were pressed through "Hot Press" at $145 - 150°C$ for 10 minutes to obtain a smooth film. After that, contact angle measurements were performed using a Kruss apparatus (DSA25S), measuring the evolution of a drop of water on film surfaces. The zero point was considered as the time in which the drop was completely spread on the surface, meanwhile, the evolution of the droplet shape was recorded by a CCD video camera. An image analysis software was then used to determine the contact angle evolution, doing an average between the right and left angle of the droplet through a "Single SDM" method.

4.1.3.6 Mechanical Test

The mechanical characteristics were evaluated using an MTS hydraulic testing machine (model LVDT, Italsigma s.r.l., Forlì, Italy) equipped with a $2kN$ load cell (HBM-S9M/2kN). Cylindric scaffolds of each blend were compressed at 0.04 mm/sec until a maximum of 45-50% strain. The compression modulus was defined as the slope of a linear fit to the stress-strain curve over 0–5% strain [46]. All uni-axial compression tests were carried out both in wet and dry conditions, under ambient conditions (temperature $25-28°C$ and relative humidity 20–50%). In detail, samples were soaked into saline solution until complete cover for 5 days before testing for wet conditions.

4.1.3.7 Statistical Analysis

An ANOVA analysis of the collected data was carried out using *software* R. In particular, the compression moduli obtained from the mechanical tests were used to identify a trend in mechanical responses, comparing compositions and conditions. Thereafter, multiple comparison tests (independent T-tests) with Bonferroni correction were subsequently performed to identify which specific combinations of SC or SGC and PCL were significantly different. The compression test was repeated five times for each SC/PCL and SGC/PCL blend and each condition, for a total of 40 samples. The mean values as well as the standard deviation of each blend were also calculated.

4.1.3.8 Scanning electron microscopy (SEM)

For SEM analysis, SC/PCL and SGC/PCL scaffolds were frozen in liquid N_2 and cut with a razor blade perpendicularly to the sample height. After that, the obtaining samples were sputter-coated with gold (Cresignton 108 Auto) and imaged on a microscope (Jeol JSM-IT200 InTouchScope) under both secondary and backscattered electrons with an acceleration voltage of 10 keV. Energy Dispersive X-ray Spectroscopy (EDS) was also performed with an acceleration voltage of 15 keV.

4.1.3.9 Bioevaluation Test

Scaffolds of each blend and pure PCL were immersed into a Simulated Body Fluid (SBF) solution for 0, 7, 14, and 21 days for a bio-evaluation test. Day 0 was used as a control test for each blend. After soaking, samples were washed 2-3 times with MilliQ and let dry overnight under the hood, before EDS analysis.

4.2 Results and Discussion

4.2.1 Properties of PLA/PCL scaffolds

Viscous encapsulation into PLA/PCL blends was extensively investigated in this paper. In detail, five blends of PLA/PCL in the ratio of 10:90, 30:70, 50:50, 70:30, and 90:10, were first synthesized through a polymeric emulsion reaction. Since this phenomenon occurs during a melting process, a 3D FGF technique was adopted for this analysis. Therefore, a preliminary thermal analysis of each blend was necessary, so they were analyzed by DSC (*Figure 4.10*) to evaluate the characteristic temperatures as Glass Transition (T_g), Melting (T_m), and Crystallization (T_c) ones. However, PLA's glass transition temperature (56.52 $°C$) and PCL's melting peak (54.53 $°C$) are so close to each other that it was very difficult to distinguish between them in the thermograms of the blends. Consequently, an endothermic peak attributed to both polymers was observed in each blend, i.e. $\sim 54°C$ and $\sim$148 $°C$, corresponding to the melting peaks of the PCL and PLA phases, respectively. Conversely, PLA90/PCL10 and PLA10/PCL90 showed a DSC thermogram similar to those of neat PLA and neat PCL, respectively. Despite this, the temperature at which this peak occurs did not change significantly as a function of the blending ratio. Indeed, the PLA phase presented cold crystallization temperature and melting peaks of 122.42 and 150.46 $°C$, respectively, which are similar to those of pure PLA, thus suggesting highly immiscible blends.

Table 4.4: *Results of DSC analysis on PLA/PCL blends in different ratios using equations* (4.1) *and* (4.2) *to calculate the degree of crystallinity.*

Sample	[a] ΔH_{cc} [J/g]	[b] ΔH_m^{PLA} [J/g]	[c] X_c^{PLA} [%]	[d] X_c^{*PLA} [%]	[e] T_g [°C]	[f] T_m^{PCL} [°C]	[g] T_c [°C]	[h] T_m^{PLA} [°C]
PLA	18.84	19.87	21.36	1.1	56.52	-	122.42	150.46
PLA90/PCL10	19.87	19.40	23.74	0.6	56.64	-	114.90	149.06
PLA70/PCL30	19.40	19.36	29.79	0.1	-	54.68	101.69	150.77
PLA50/PCL50	19.72	21.15	45.49	3.1	-	53.07	108.65	148.64
PLA30/PCL70	7.52	8.04	28.82	1.9	-	55.38	111.56	148.18
PLA10/PCL90	-	1.07	11.52	11.52	-	54.74	-	146.51
PCL	-	-	-	-	-	54.35	-	-

[a] ΔH_{cc} *cold crystallization heat*
[b] ΔH_m^{PLA} *fusion enthalpy of PLA*
[c] X_c^{PLA} *degree of crystallinity of PLA*
[d] X_c^{*PLA} *degree of crystallinity of PLA in the original sample*
[e] T_g *glass transition temperature of PLA fraction*
[f] T_m^{PCL} *melting temperature of PCL fraction*
[g] T_c *crystallization temperature of PLA fraction*
[h] T_m^{PLA} *melting temperature of PLA fraction*

Then, *Eq.*(4.1) and (4.2) were used to calculate the degree of crystallinity of the neat polymers and PLA/PCL blends, as summarized in *Table 4.4*. It can be noticed that the degree of crystallinity of the PLA phase increased significantly as PCL was blended up to 50%; i.e. it is twice that measured in pure PLA. The increased crystallinity can be explained by interfaces between the phases, which act as nucleation regions for the PLA, as already reported in literature [51].

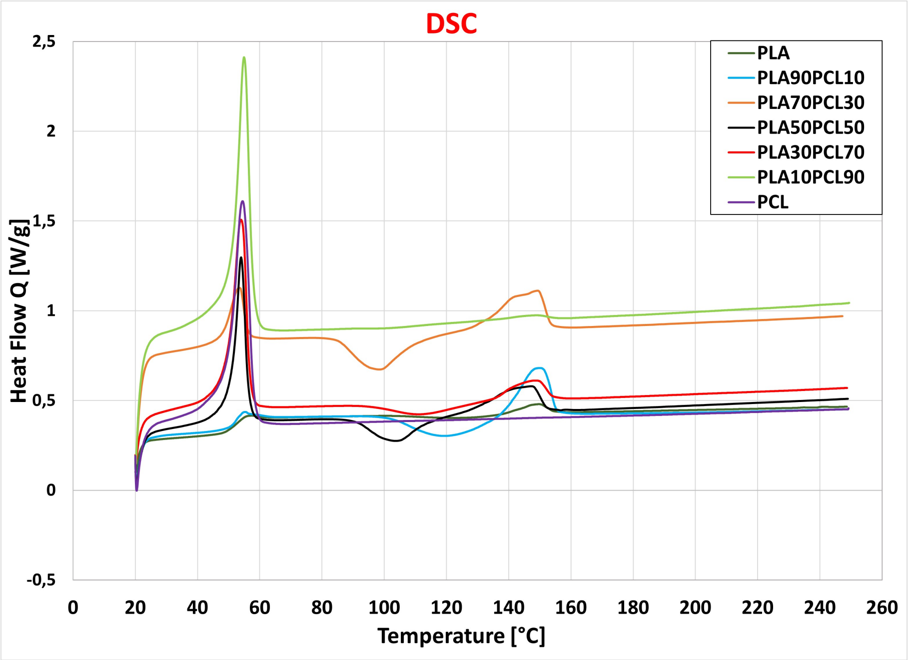

(a) Heating curves

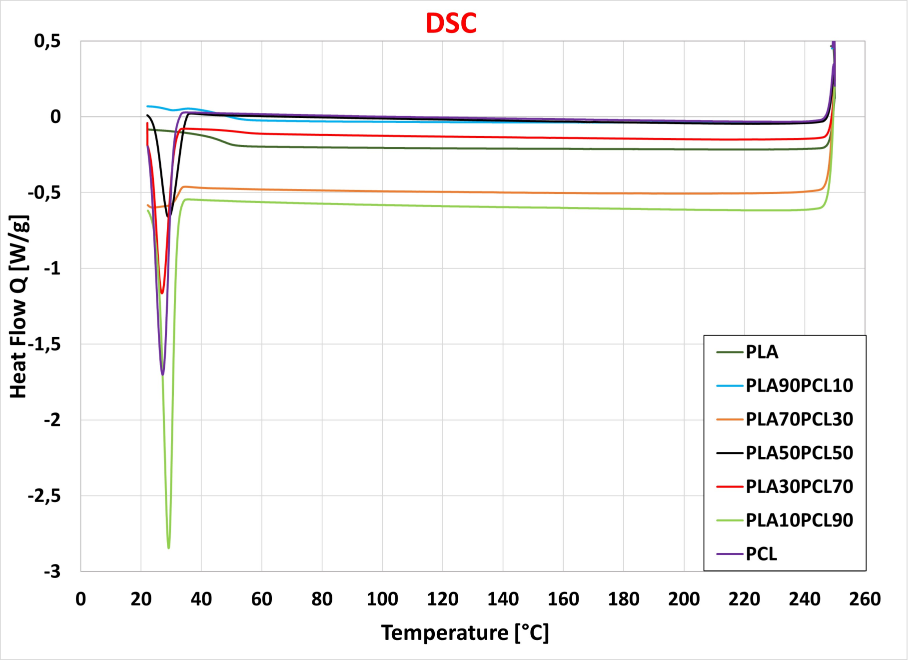

(b) Cooling curves

Figure 4.10: *Heat Flow curves obtained by DSC analysis on PLA/PCL blends during II heating cycle from* 20°*C until* 250°*C in **(a)** and II cooling cycle from* 250°*C until* 20°*C in **(b)**.*

After that, both rectangular and cylindrical scaffolds (*Figure 4.5*) of PLA/PCL

blend were printed optimizing process parameters according to printability of each blend (as reported in *Table 4.1*).
Regarding the rheological properties, a rheological analysis of neat PLA and PCL was also performed, showing that the PCL viscosity curve was lower than the PLA viscosity curve in a lower shear rate region (*Figure 4.11*). This should give an idea of which material encapsulates the other in the viscous encapsulation phenomenon, according to literature [1].
Subsequently, fiber cross-section analysis was carried out in order to highlight the presence of the viscous encapsulation phenomenon. In detail, image analyses were necessary to distinguish PCL and PLA domains in the structure. In fact, *Figure 4.13* shows three different SEM images of the PLA50/PCL50 sample where it was possible to see two different zones: black and white. Similarly, TEM images in *Figure 4.14* showed the clear formation of two different domains: one was related to a black zone, and the other one was related to a black/white zone. However, in both cases, it was not possible to correlate the domain to the material.

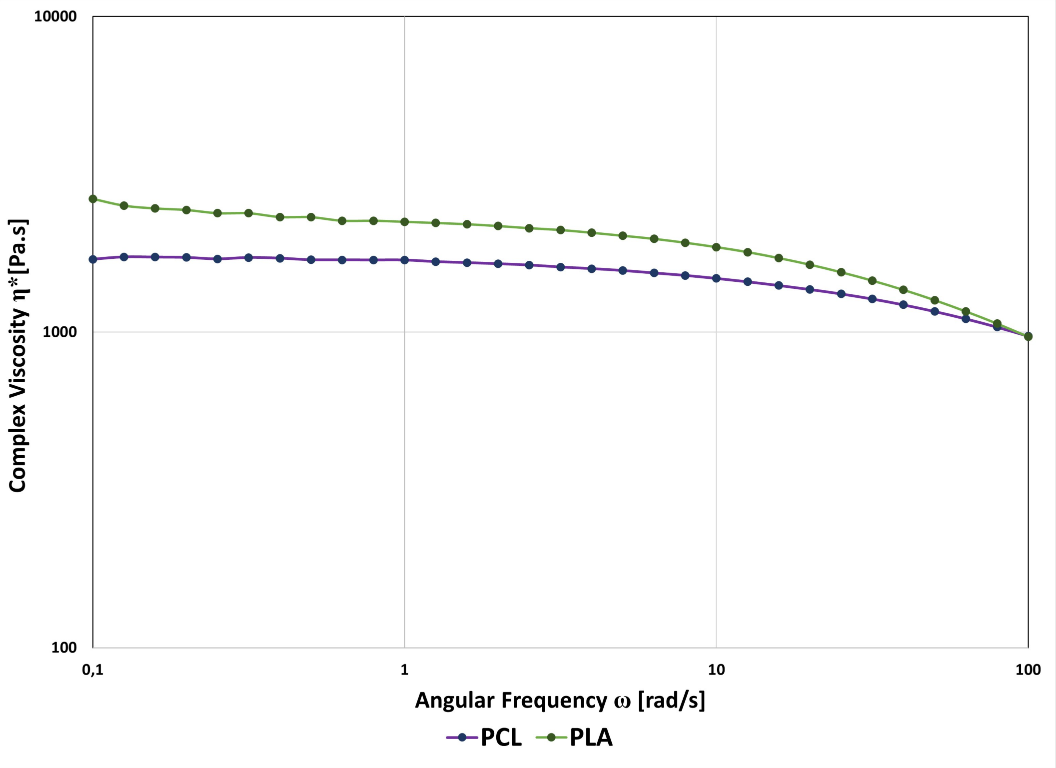

Figure 4.11: *Comparison of Complex viscosity curves of PCL and PLA according to results showed in Figure4.12.*

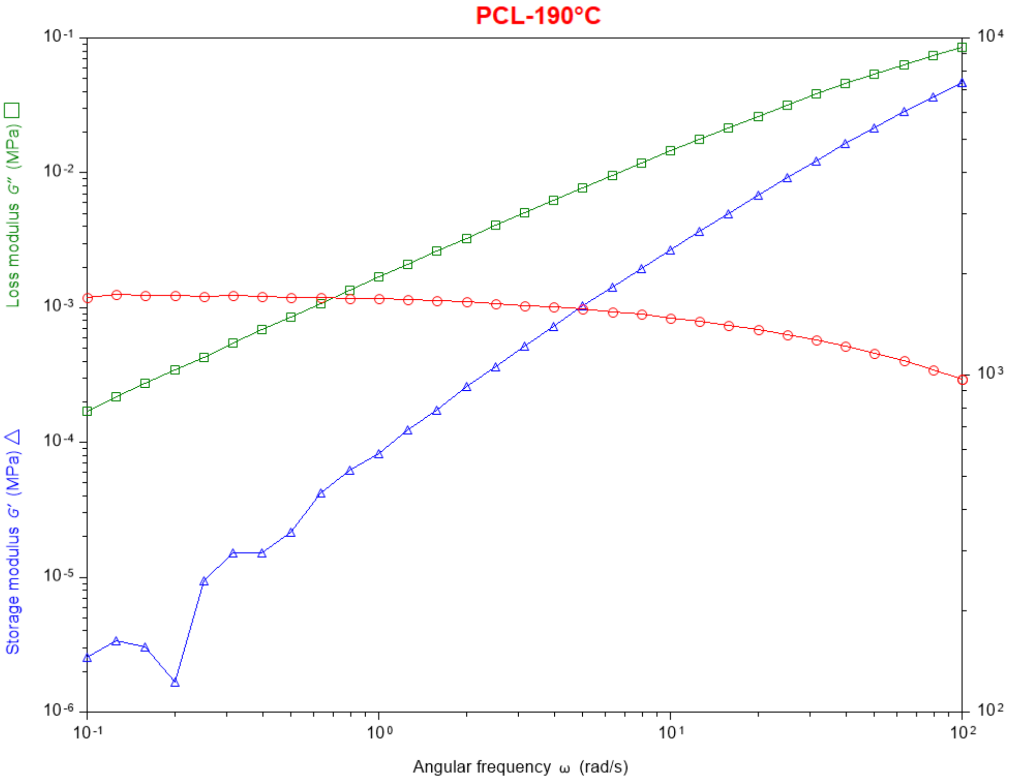

(a) PCL

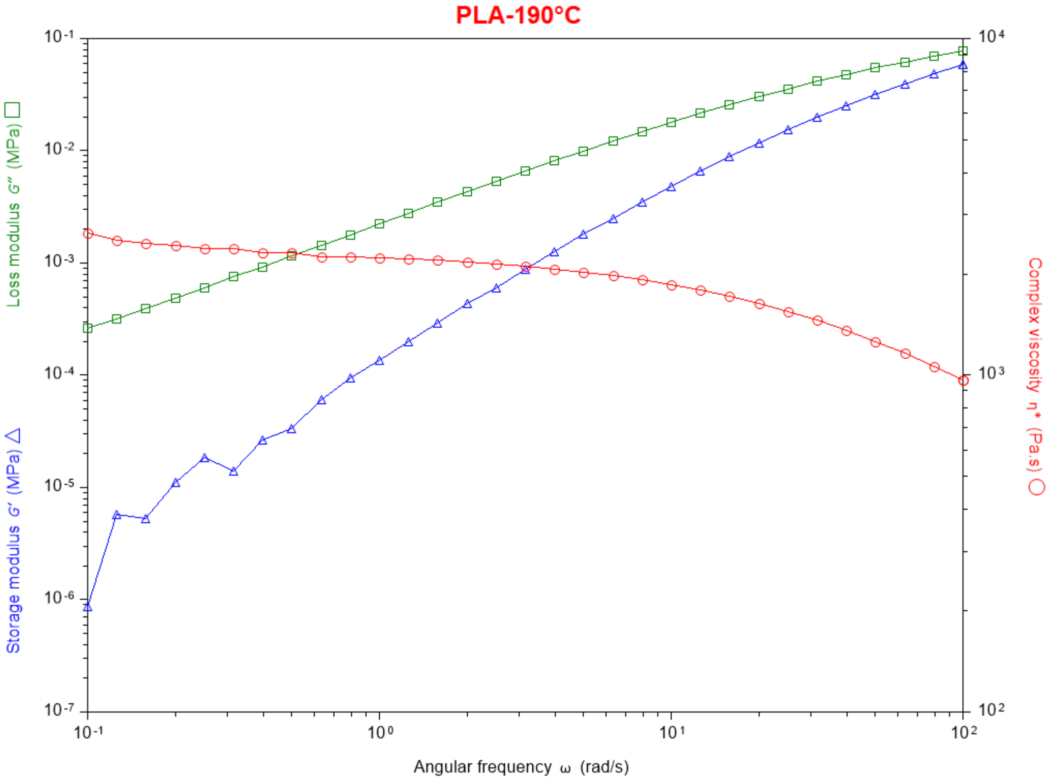

(b) PLA

Figure 4.12: *Complex viscosity curves of PCL and PLA measured by parallel-plane rotational rheometer at 190°C.*

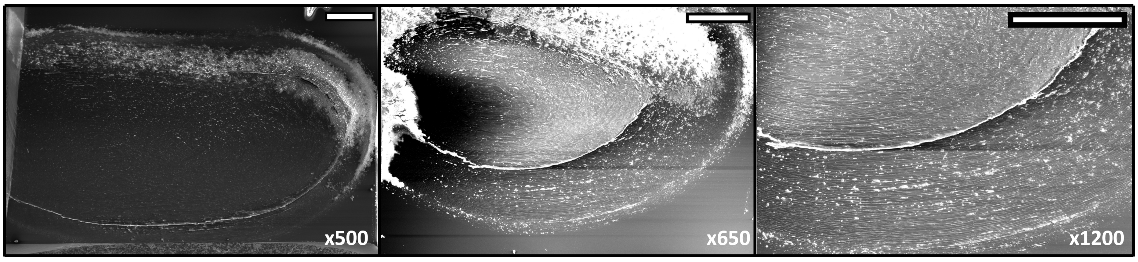

Figure 4.13: *SEM images with increasing magnification showing fibers cross-section of PLA50/PCL50 scaffold, printed by Bioscaffolder SYSENG, where PLA phases (light gray) are in a PCL-rich matrix (dark gray); scale bar 100µm.*

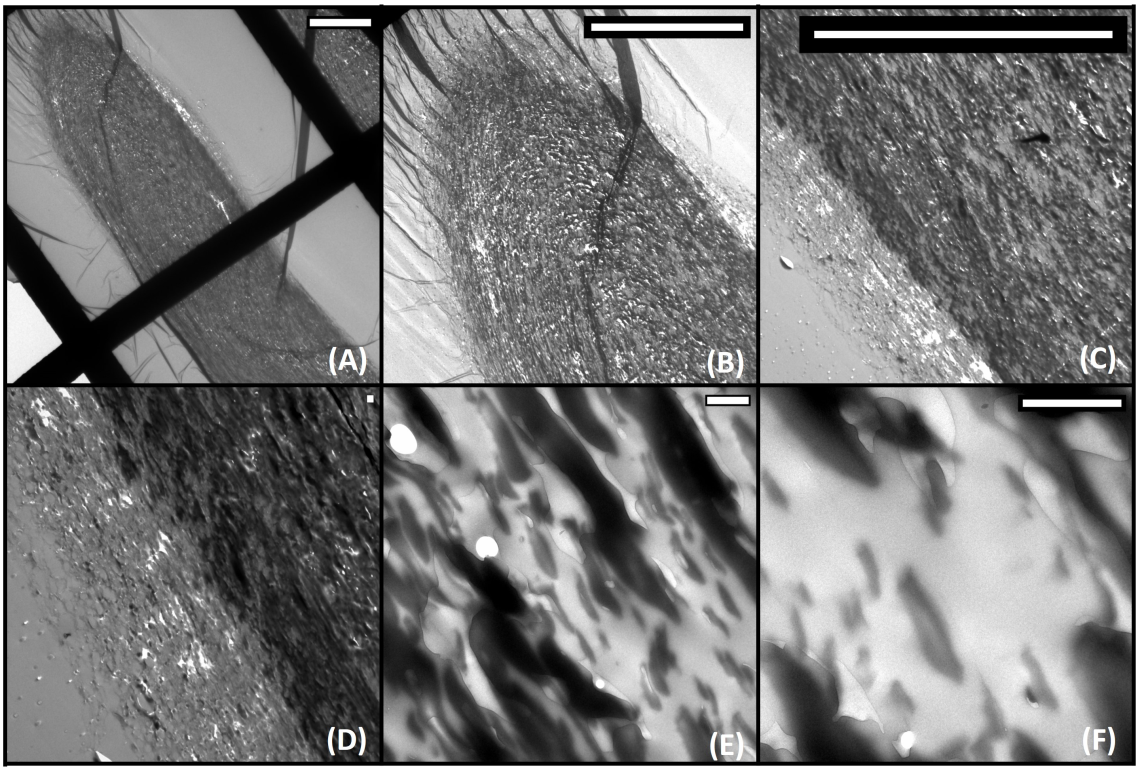

Figure 4.14: *TEM images showing fibers cross-section of PLA50/PCL50 blend printed by Bioscaffolder SYSENG at increasing magnification values; where PCL appears as high-contrast phases (crystalline, dark) and PLA as low-contrast phases (amorphous, bright); scale bar of 100 µm for image A, B, C and 1 µm for image D, E and F.*

For this reason, detailed PLM images of the cross-sections on pure PCL, PLA, and PLA50/PCL50 scaffolds were made at 20x with the same settings. In this way, it was possible to distinguish each domain in the PLM image of the PLA50/PCL50 blend, comparing the results with images of pure PCL and pure PLA. In detail, the PCL and PLA50/PCL50 blend provided a neat set of cross-sectional views of the fibers, while the PLA images did not show the same result (*Figure 4.15*). Then, PCL appeared as a high-contrast phase (crystalline, dark) while PLA was a low-contrast phase (semi-crystalline, bright).

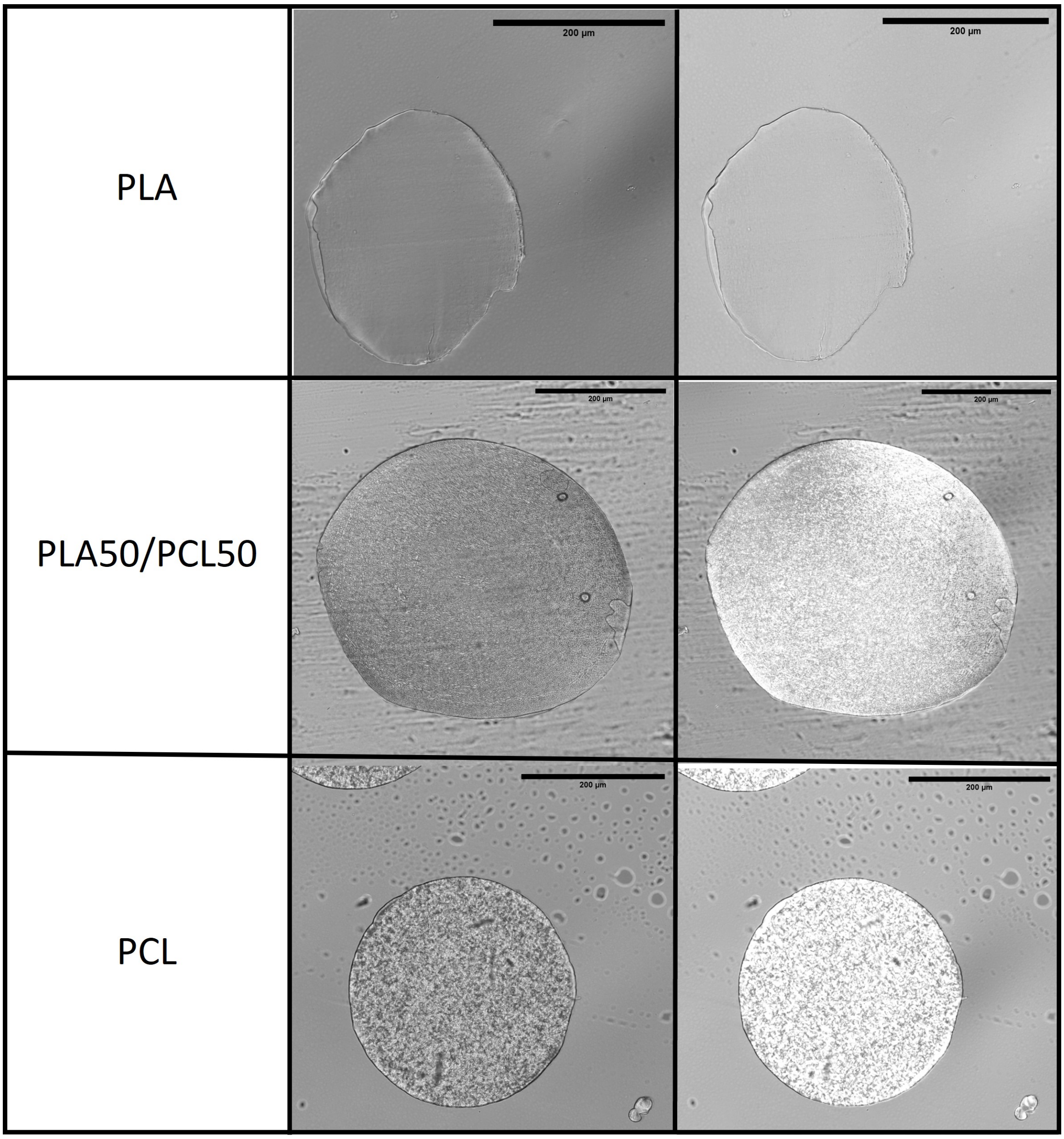

Figure 4.15: *PLM image showing brightfield of the same fiber cross-section with two different lightness. The fibers are made of pure PLA, PLA50/PCL50, and pure PCL, respectively.*

Anyway, SEM analysis did not show a single core-shell structure but showed a shell defined by a single component and a core composed of a mixture of the two materials. To further evaluate the formed structure, a selective dissolution test was conducted on PLA50/PCL50 scaffolds with a time of $2h$ to $12h$. In particular, AA was used to remove only the PCL content, obtaining the PLA-skeletons shown in *Figure 4.16*. These SEM images had indeed revealed the presence of a circular biphasic structure, as also underlined by the red circle-line in the 4h soak image.

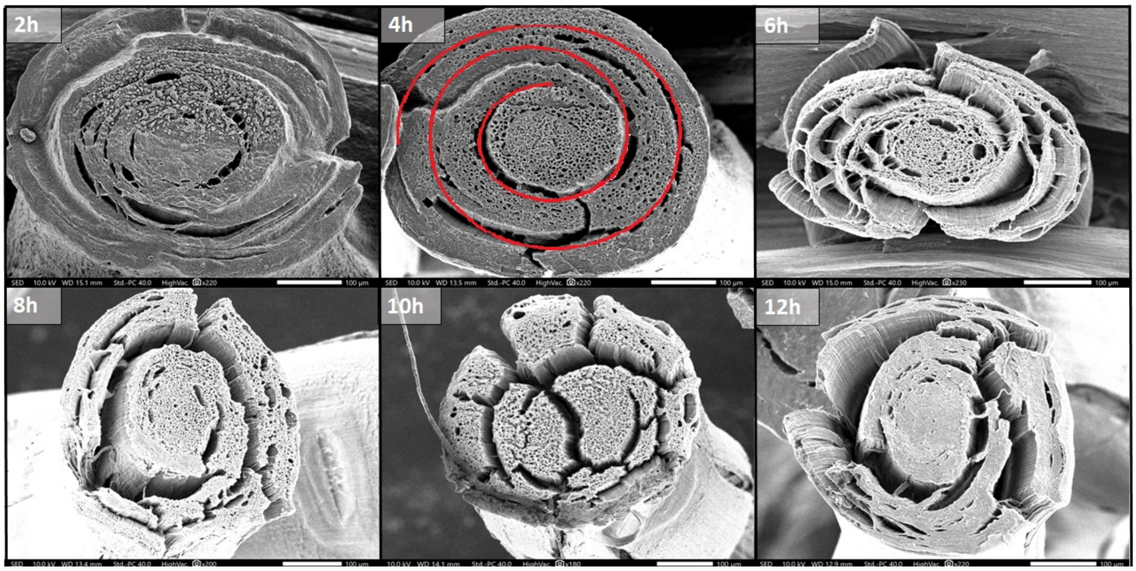

Figure 4.16: *SEM images of PLA50/PCL50 fibers cross-section, after soaked into Acetic Acid for 2, 4, 6, 8, 10, and 12 hours, respectively; scale bar of 100µm.*

Finally, SEM analysis on PLA/PCL blends was performed to evaluate the polymer ratio influencing the viscous encapsulation phenomenon. Fibers cross section showed that an increase in PCL content corresponds to an increase in the shell-thickness, as highlighted by the red arrow in *Figure 4.17*.

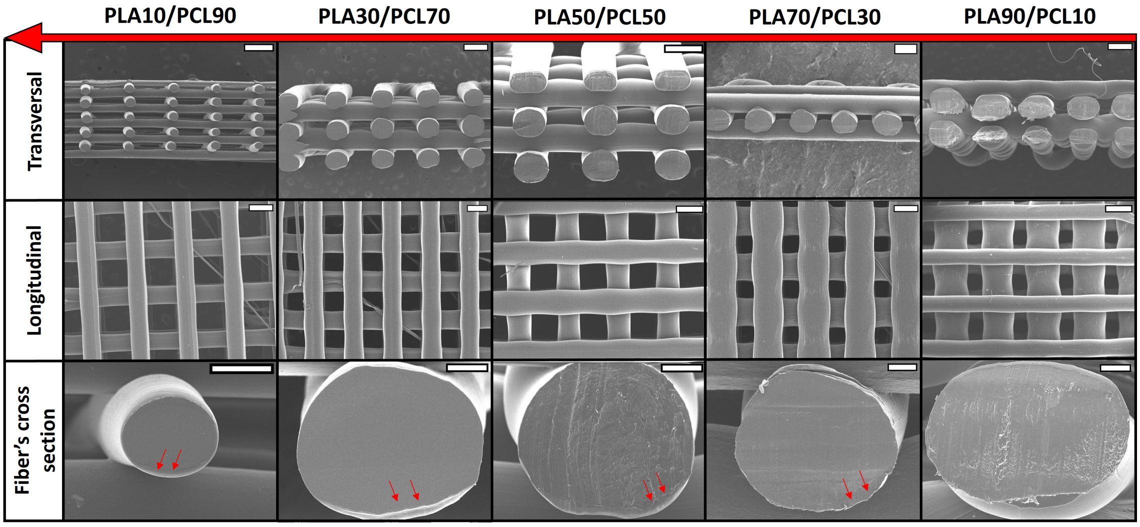

Figure 4.17: *SEM image of PLA/PCL blends to analyze the polymer ratio influences on the viscous encapsulation phenomenon. Scaffold structures in both longitudinal and transversal directions are shown, while red arrows highlight PCL-shell; scale bar of 500µm for images of longitudinal and transversal direction, and 100µm for fiber's cross-section images.*

So that, PLA10/PCL90 was used to further investigate the influence of the 3D printer process parameters. In detail, four values of extrusion speed (i.e., from 100 *mm/min* to 180 *mm/min*), three values of screw speed i.e.: 30, 35, and 40 *rpm*, and five values of pressure, i.e.: 4, 5, 6, 7, and 8 *bar* were analyzed, as shown in *Figure 4.19a, 4.19b* and *4.19c*, respectively. Similarly, *Figure 4.18* shows fibers cross-section analysis using four different Length/Diameter (L/D) capillary needles (i.e., G22, G28, G30, and G32), and process parameters reported in *Table 4.2*.

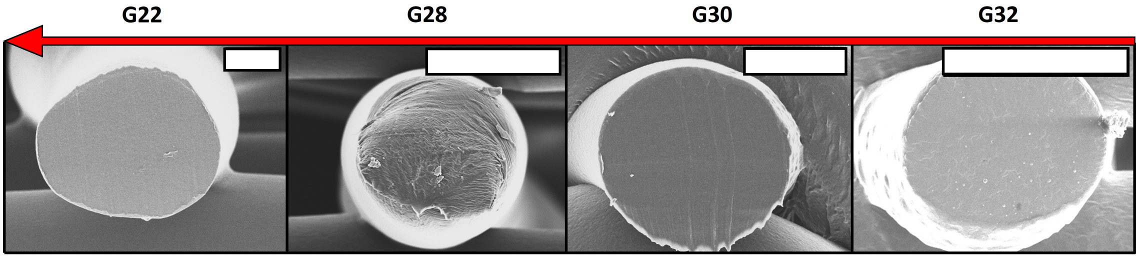

Figure 4.18: *SEM image showing fibers cross-section of PLA10/PCL90 scaffold, printed by Bioscaffolder SYSENG, using same process parameters and four different needles: G22, G28, G30, and G32. The red arrow indicates shell thickness increasing as well as the encapsulation phenomenon increasing; scale bar of 100µm.*

An increase in extrusion speed usually means that PCL had enough force to move in the radial direction, so shell-thickness becomes larger (*Figure 4.19a*). The same result was also obtained by changing screw speed and pressure (*Figure 4.19b* and *Figure 4.19c*, respectively). In any case, comparing the value of shell-thickness reported in the magnification of each picture in *Figures 4.17, 4.18, and 4.19*, process parameters showed to have a greater effect than the L/D ratio or PLA/PCL content.

Additionally, mechanical tests were performed, obtaining stress-strain curves of each PLA/PCL blend both in wet and dry conditions, as plotted in *Figure 4.21a* and *4.21b*, respectively. Hence, the compression modulus of each blend was reported for both wet and dry conditions (*Figure 4.21*).

PLA/PCL blends did not show a trend as a function of each component, as it was necessary to consider the use of a mixture of immiscible polymers and the influence of the core-shell structure on the final mechanical properties of the scaffolds. Comparing mechanical properties against the PLA (or PCL) content, it was possible to note that there was a significant difference in compression modulus both in dry ($F = 35.81$, $p < 0.001$) and wet condition ($F = 8.441$, $p = 0.00229$). Vice versa, comparing the results of the same blend between wet and dry conditions, only the PLA90/PCL10 showed a significant difference in the compression modulus of ($p < 0.05$): from 54.63±8.4MPa in dry condition (similar to 62 MPa of pure PLA[49]) to 10.77±0.17MPa in wet condition. In contrast, the other blends showed no significant differences in the compression modulus between wet and dry conditions ($p > 0.05$).

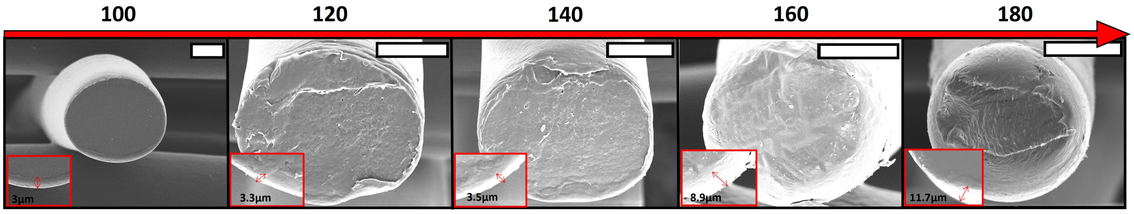

(a) Extrusion Speed

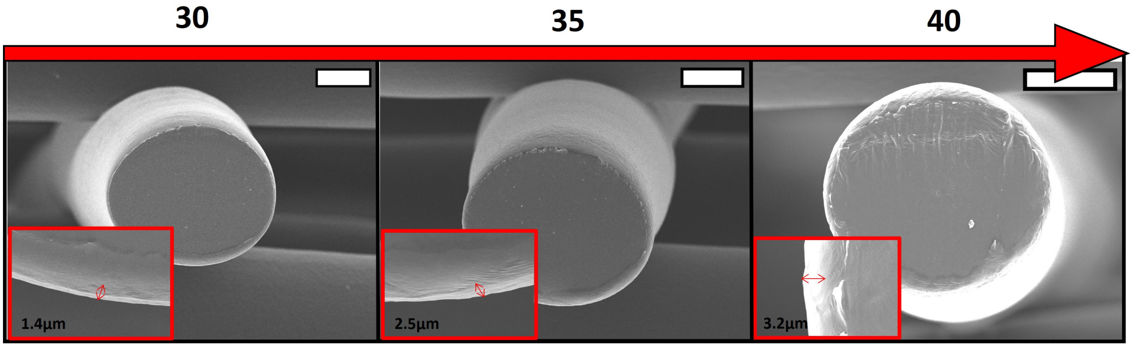

(b) Screw Speed

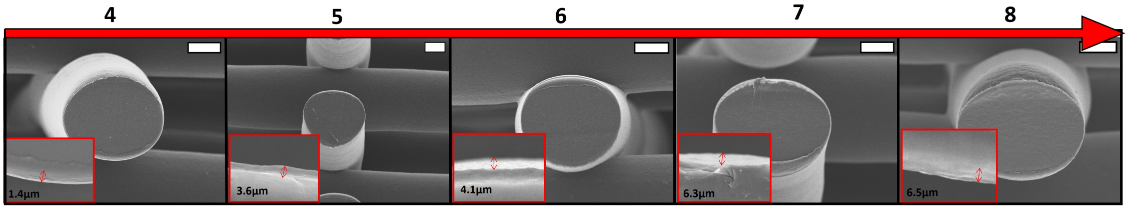

(c) Pressure

Figure 4.19: *SEM images of PLA10/PCL90 fibers cross-section, using:* ***(a)*** *five values of extrusion speed, i.e.: 100, 120, 140, 160, and 180 mm/min,* ***(b)*** *three values of Screw Speed i.e.: 30, 35 and 40 rpm, and* ***(c)*** *five values of Pressure, i.e.: 4, 5, 6, 7, and 8 bar; scale bar of 50µm.*

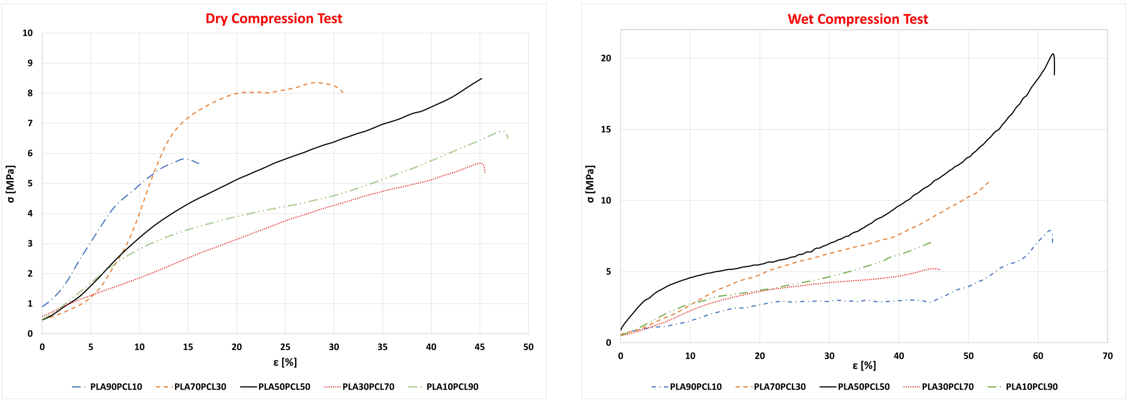

(a) (b)

Figure 4.20: *Stress-strain curves of each blend in both dry* ***(a)*** *and wet* ***(b)*** *conditions, considering the scaffold cylinder's apparent surface for stress values.*

Even though PCL and PLA are both hydrophobic, PCL is more hydrophobic than PLA. For this reason, it should be possible that the PLA-core absorbed the saline solution used for wet conditions, and significantly reduced its mechanical properties. As the PLA content decreased, it had less effect on the blends' mechanical response; so that, the PLA10/PCL90 modulus did not differ significantly between wet and dry conditions (from 23.15±1.5 MPa to 24.11 ±2.7 MPa). In addition, increasing the PCL content also means the shell was thicker (as shown in *Figure 4.17*), creating a structure that insulated and separated the PLA-core from the saline solution. The PCL-shell was not sufficient to protect the PLA core in PLA90/PCL10, while it was large enough in PLA10/PCL90. Likewise, compression modulus decreased as PCL content increased in dry conditions (*Figure 4.21a*), except for PLA10/PCL90, which did not follow this trend. Thus, PLA was significantly more elastic relative to the stiffer PCL, so the PLA50/PCL50 blend had an intermediate modulus value (23.41 ± 3.16 MPa) in dry conditions. On the other side, as PCL content increased the compression modulus also increased in wet conditions (from 10.77±0.17 MPa of PLA90/PCL10 to 33.017±9.4 MPa of PLA50/PCL50), until PLA30/PCL70, which had the lower value (17.15±3.02 MPa). It can be assumed that the core-shell structure was perfectly balanced in the PLA50/PCL50 blend, so it had maximum modulus in wet conditions because it can spread load and saline solution into the entire structure; its modulus is signification different from other blends, specifically to PLA70/PCL30 and PLA90/PCL10. These results were also confirmed by the crystalline percentage in DSC analysis (see *Table 4.4*), showing the lower value of crystallinity for PLA90/PCL10, while PLA50/PCL50 had the higher one. From a mechanical point of view, It is known that, during compression tests, crystalline regions oppose resistance to pressure by increasing tension, while amorphous regions can flow under pressure, increasing deformation. Therefore, in wet compression tests, when the PLA content increased the material could support a lower load and became more brittle, too; in fact, the PLA90/PCL10 samples crumbled at 60% strain (*Figure 4.21b*).

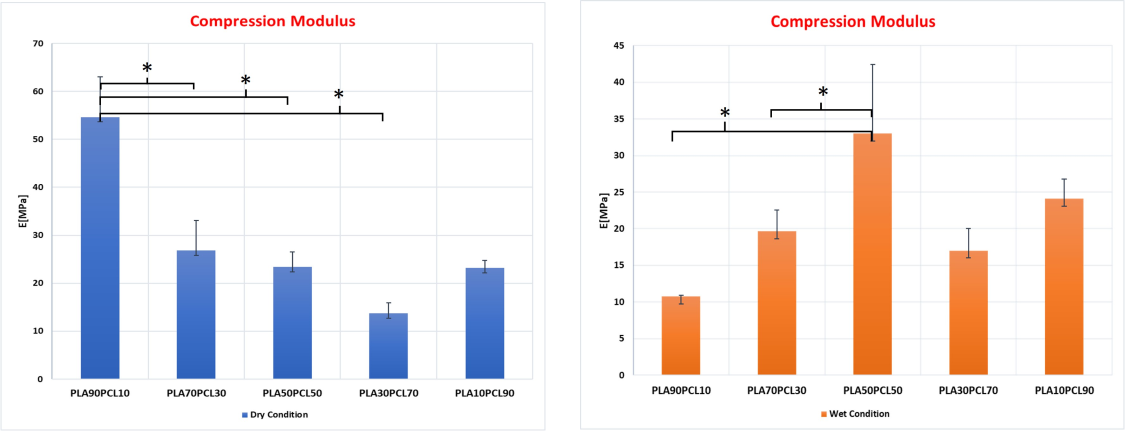

(a) **(b)**

Figure 4.21: *Compression Modulus of PLA/PCL blends in both dry **(a)** and wet **(b)** conditions, considering the scaffold cylinder's apparent surface for stress values.*

In the concept of mechanical properties, FE analysis on six structures was also performed on nTop. Stress and strain results were calculated using the average of nodal values to produce accurate results, according to the software algorithm. The value of Total Displacement, Longitudinal Strain (i.e. along z-axes), and Von Mises Stress of each structure are shown respectively in *Figure 4.22*, *4.23* and *4.24*. The results in terms of max displacement, and the corresponding max strain, for each structure were also summarized into *Table 4.5*.

Firstly, the FE analysis was validated by comparing the maximum strain value obtained in the compression tests for PLA50/PCL50 (about 45%), with the total displacement obtained for *S:00-90°*, see *Table 4.5*. The value obtained in the latter case is 2.4mm to which a strain of about 40% corresponds, so the result of the FE analysis can be considered acceptable.

Table 4.5: *Estimation of porosity on scaffold structures using Eq.*(4.3).

Structure	**Fiber Thickness** [mm]	**V$_T$** [mm^3]	**V$_m$** [mm^3]	**P** [%]	**Max Displacement** [mm]	ε_{max} [%]	**Pore size** [mm]
S:00-90°	0.4	246.99	90.55	63.34	2.44	40.67	0.36 to 0.56
S:00-45°	0.4	250.85	103.98	58.55	1.94	32.33	0.25 to 0.63
G:00-90°	0.2	216	87.80	59.35	1.60	26.67	0.29
G:00-45°	0.2	216	86.54	59.93	1.79	29.00	0.30
V_cost	0.3	216	102.52	52.54	1.76	29.33	0.3 to 0.73
V_ramp	0.3	216	119.23	44.80	1.06	17.67	0.3 to 0.75

According to *Table 4.5*, the *S:00-90°* structure demonstrated the higher value of displacement and porosity (2.44mm and 63.34%), whereas the *V_ramp* had the lower one, (1.06mm and 44.80%). This means that despite the small difference in porosity and fiber thickness, there is a significant difference in displacement and therefore maximum strain. Vice versa, *G:00-45°* and *V_cost* showed similar values although the structures are very different, while *G:00-90°* and *S:00-45°* demonstrated intermediate values among the designs. However, the major difference between the structures can be seen through the color map in both *Figure 4.23* and *4.24*. The S-structures show several concentrated zones of maximum stress and strain, particularly at the contact points between two consecutive layers, i.e. at the load transmission zones; vice versa, the non-contact zones show the minimum stress and strain values. Anyway, *S:00-45°* showed lower values of stress and strain compared to *S:00-90°*, and a wider range of pore sizes, but without significant differences. In both cases, S-structures can be considered anisotropic structures because stress and strain are distributed along the normal direction of the structure.

As shown in *Figure 4.24*, the Gyroid structures seemed to distribute the stress homogeneously along the planes as an isotropic material; the highest stress following only the anchoring fibers with the support boxes. They can be considered both isotropic structures, but comparing the results, the *G:00-90°* exhibited lower values of stress, strain, displacement, and porosity, compared to *G:00-45°* reflecting a higher strength of the structure while maintaining the same porosity, pore size and fiber thickness.

Meanwhile, the Voronoi designs exhibited the highest stress value only at the anchorage points between two or more fibers in the structures, as isotropic structures too. Here it's possible to understand the difference in material properties according to the distribution of pores. Indeed, *V_ ramp* shows lower and more uniform stress and strain values than *V_ cost* in both *Figure 4.23* and *4.24*. Despite both Voronoi structures having the same fiber thickness, the gradient porosity in *V_ ramp* resulted in a lower porosity than *V_ cost* and consequently lower displacement and strain (see *Table 4.5*). Moreover, Voronoi lattice also guaranteed a gradient in pore size from the center to the outside in both structures, with similar values.

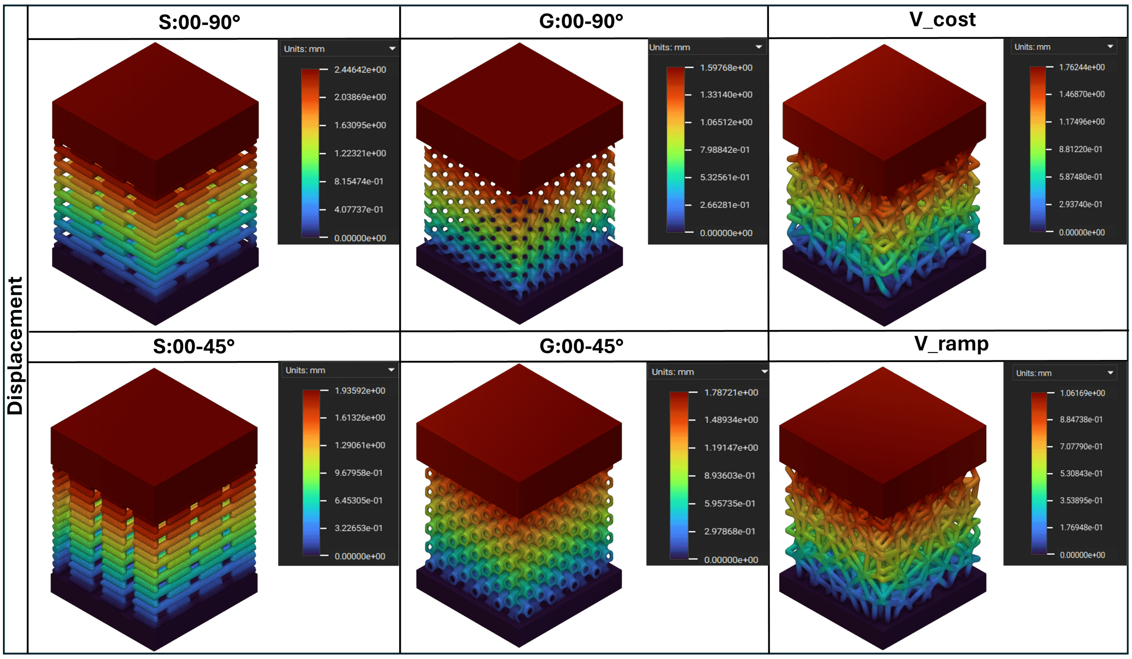

Figure 4.22: *Static Analysis results for a simulation of a compressive test using Ntopology software on S-structure, Gyroid-structure, and Voronoi-structure. The color map of each structure corresponds to the right in terms of Total Displacement [mm].*

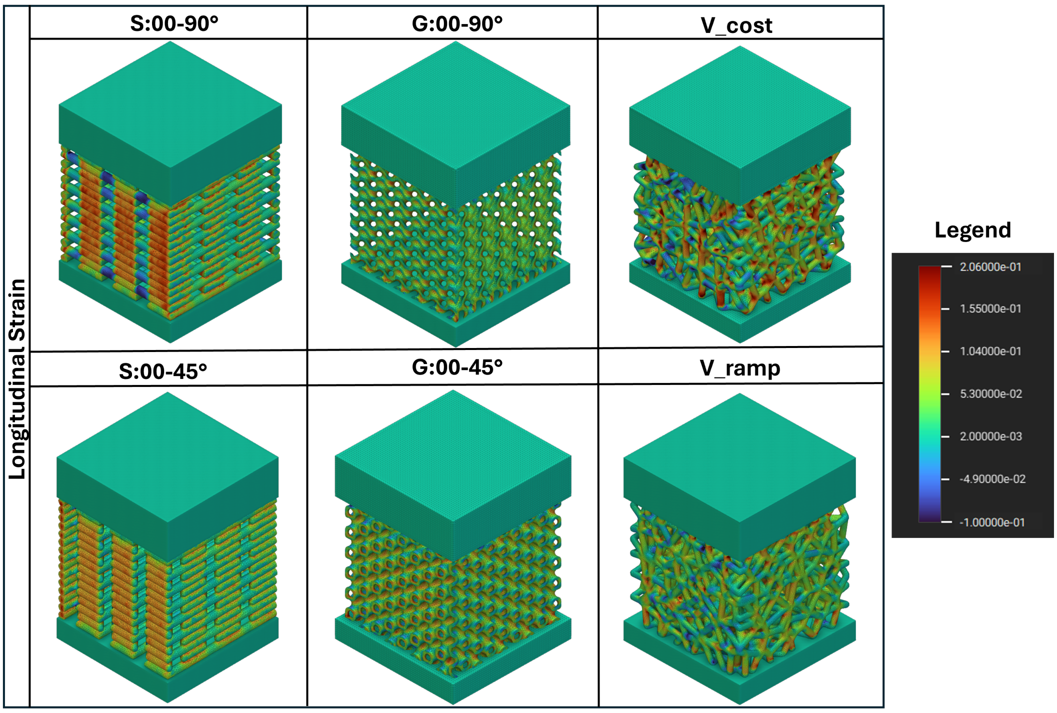

Figure 4.23: *Static Analysis results for a simulation of a compressive test using nTop software on S-structure, Gyroid-structure, and Voronoi-structure. The color map of each structure corresponds to the right in terms of Longitudinal Strain [adimensional].*

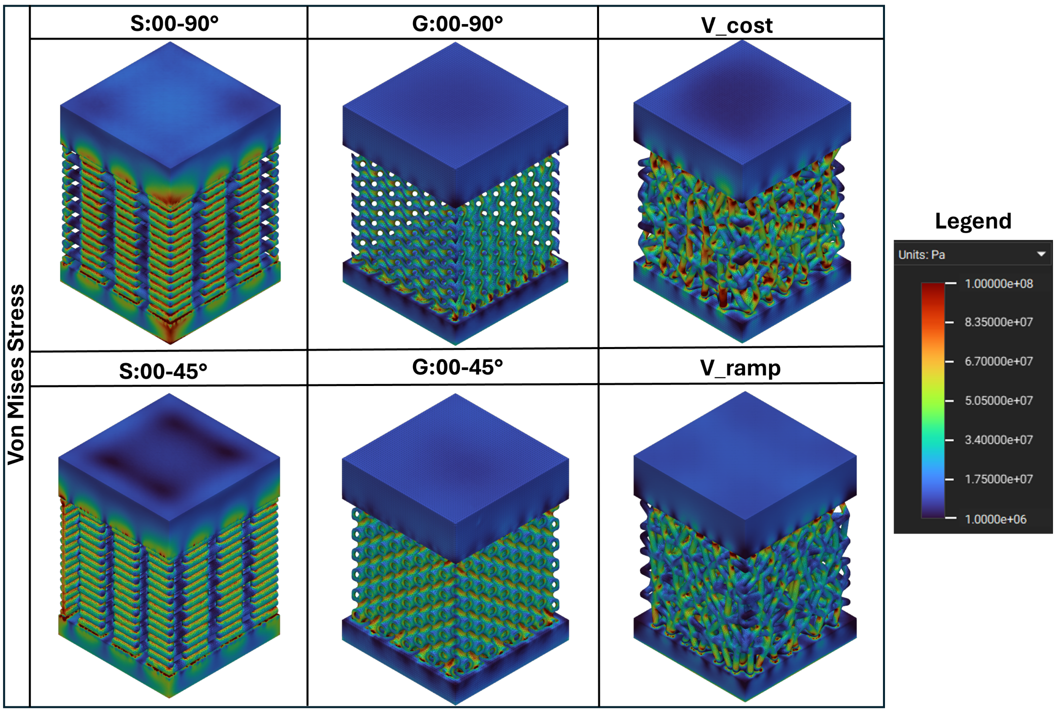

Figure 4.24: *Static Analysis results for a simulation of a compressive test using nTop software on S-structure, Gyroid-structure, and Voronoi-structure. The color map of each structure corresponds to the right in terms of Von Mises Stress [Pa].*

4.2.2 Properties of SC/PCL and SGC/PCL Scaffolds

A new blend of starch, Glycerol, CA, and PCL was investigated in this research. Firstly, SC and SGC blends, obtained through the polymeric emulsion showed in *Figure 4.3* and *4.4*, were chemically analyzed by XRD and FTIR. In detail, *Figure 4.25* shows XRD spectra of SC, and SGC blends, comparing with pure Starch and CA. Particularly, Starch spectra showed a peak of maximum intensity at 16° and other peaks at about 15°, 19° and 22°, typical for Amylose V-type [50]. CA spectra also contained its characteristic peaks, at 14°, 17°, 19°, 24°, 26°, and 29°. While Glycerol adding in SGC showed two main peaks at 2θ about 14° and 21°. Meanwhile, CA peaks are not found in SC and SGC blends, which indicates that no crystalline CA is formed during blending synthesis. This aspect was also confirmed by FTIR analysis (*Figure 4.26*), where SC spectra reported the same characteristic peaks of Starch, but not of CA. On the other hand, FTIR analysis of SC reported the characteristic peaks related to Starch, while these peaks were shifted to lower values of wave-number in SGC spectra, as shown in *Figure 4.26*).

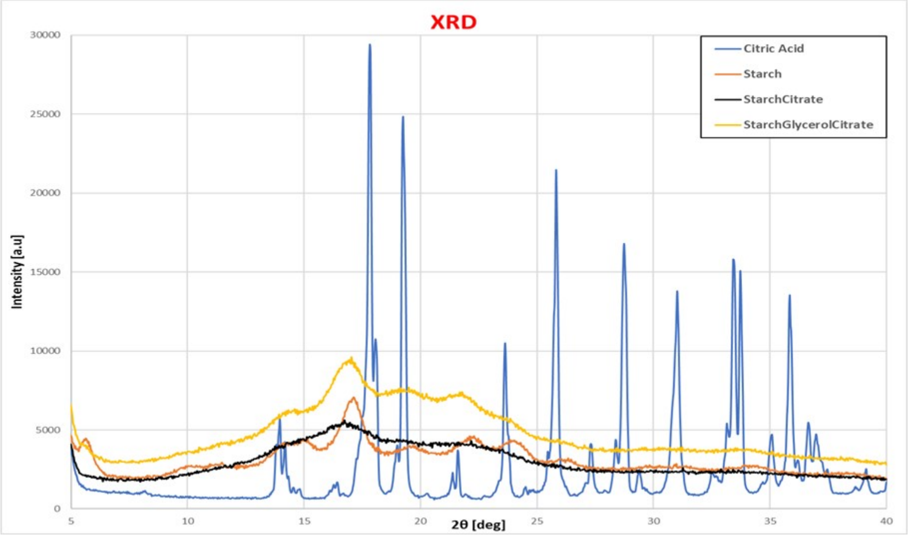

Figure 4.25: *X-Ray Diffraction spectra of Starch, Citric Acid, SC, and SGC, reporting angles (2θ degrees) and intensity (a.u) of crystalline peaks.*

Thereafter, SC and SGC were blended to PCL in the ratio of 10:90, 30:70 and 50:50 and then chemically analyzed. However, the 50:50 blends were very sticky and unwieldy, especially in the case of the SGC, therefore they were excluded from the following analyses and applications.

The remaining SC/PCL, and SGC/PCL blends were analyzed by FTIR analysis, compared to the pure PCL in *Figure 4.27.* The absorption peaks at 2944.32 and 2864.73 cm^{-1} were usually assigned to the C–H hydroxyl groups' asymmetric stretching and the C–H hydroxyl groups' symmetric stretching, respectively. Similarly, the absorption peaks at 1238.34 and 1167.24 cm^{-1} were respectively assigned to C–O–C asymmetric stretching and C–O–C– symmetric stretching. In addition, the C=O stretching vibrations of the ester carbonyl were justified by the absorption peak at 1720.65 cm^{-1}. Consequently, the FTIR spectra of SC10/PCL90 SC30/PCL70

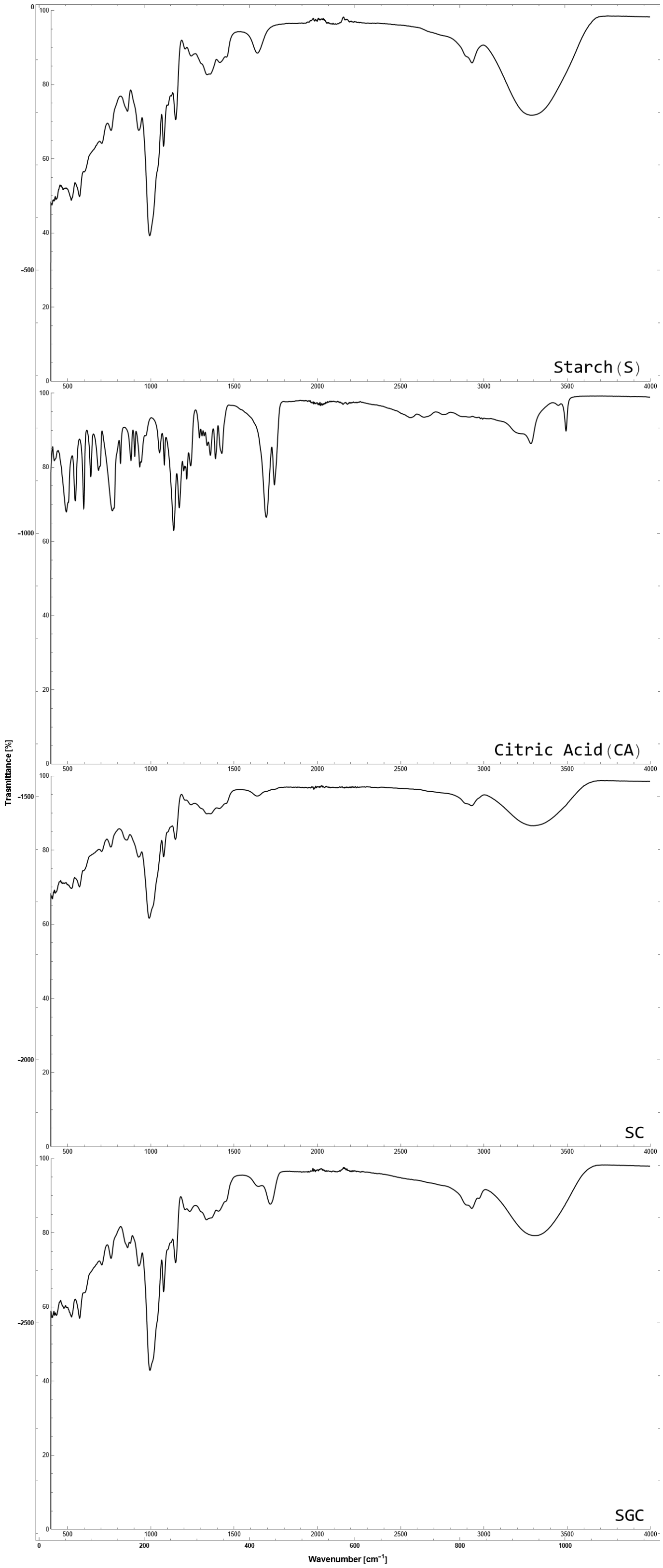

Figure 4.26: *Fourier Transformed Infrared spectroscopy of Starch(S), Citric Acid (CA), Starch/Citric Acid (SC), and Starch/Glycerol/Citric Acid (SGC).*

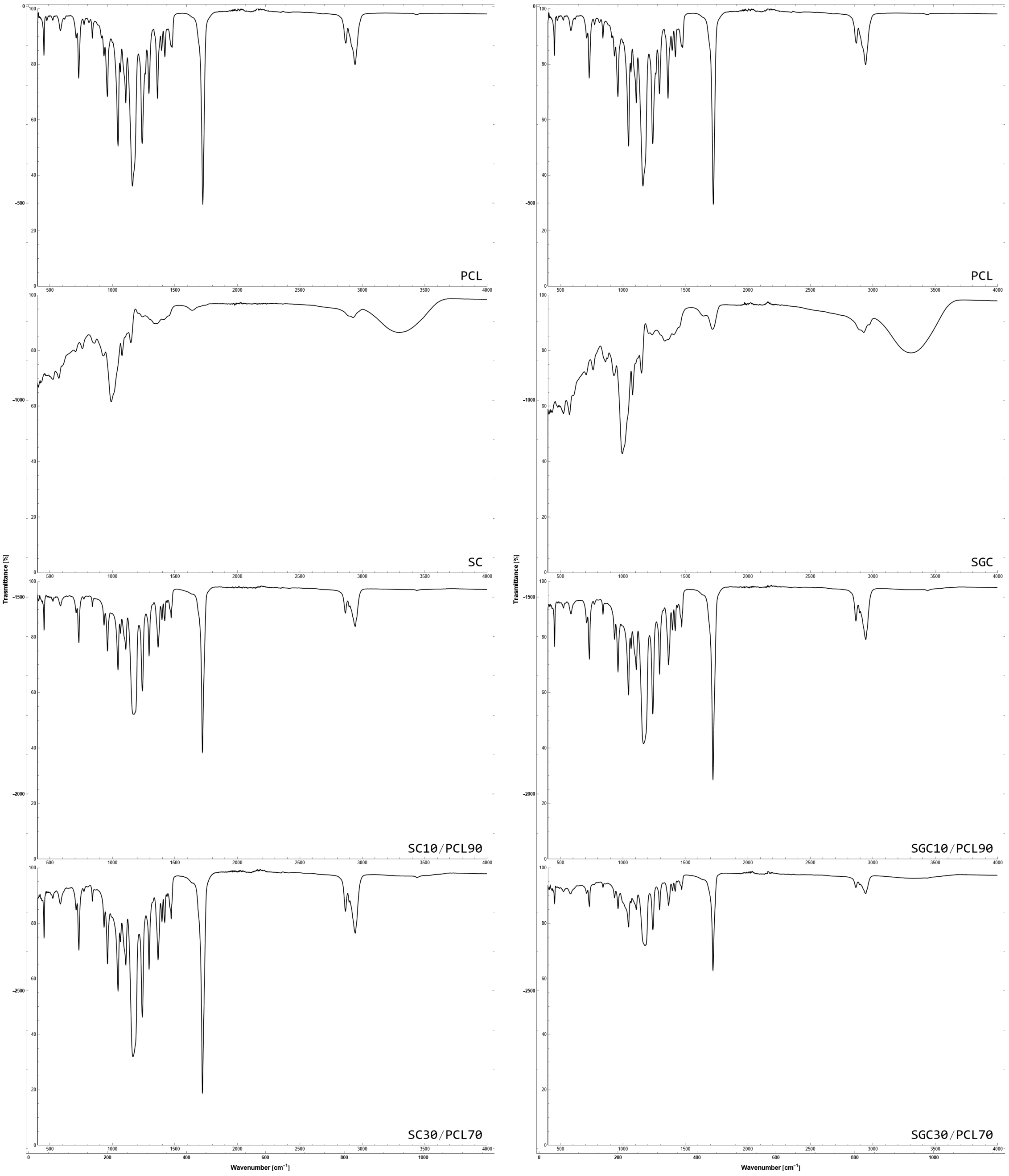

(a) **(b)**

Figure 4.27: *Fourier Transformed Infrared spectroscopy of pure PCL, SC and all blends in **(a)** and pure PCL, SGC and all blends in **(b)**.*

(*Figure 4.27a*), and SGC10/PCL90 and SGC30/PCL70 (*Figure 4.27b*) showed almost similar characteristic peaks of pure PCL. Meanwhile, all the characteristic peaks representing SC and SGC were not distinctive due to the overlapping of very intense bands of PCL. However, this overlapping was less pronounced as the PCL content was lower, i.e. for SGC30/PCL70 and SC30/PCL70. Overall, there were no significant differences between the characteristics peak of SC10/PCL90 and

SGC10/PCL90. This may be due to the low amount of Starch and Glycerol added in the prepared bio-composites thus the characteristics peaks of PCL were more dominant. The only exception was related to SGC30/PCL70 where the absorption peaks assigned to the C–H hydroxyl groups and C–O–C were still present but with less evidence (*Figure 4.27b*).
After chemically investigating the synthesized blends, a thermal investigation was also performed in order to effectively process these blends using an AM technique, i.e. a TGA analysis and a DSC analysis have been carried out. TGA analysis on SC/CPL and SGC/PCL blends exhibited two mass losses: the initial step at around $290°C$ corresponded to water loss and the possible volatilization of the plasticizer, while the second step, observed between $360°C - 415°C$, was associated with the starch decomposition (see *Figure 4.29*). Moreover, comparing blends with and without glycerol, SGC blends exhibited a degradation temperature of $5 - 10°C$ higher than SC blends.
Meanwhile, characteristic temperatures were evaluated by DSC analyses (as shown in *Figure 4.28*), while the crystallinity of each blend was calculated using *Eq.*(4.4), as summarized in *Table 4.6*. All blends showed only a T_g due to their amorphous structure, as pure PCL. However, no significant difference in T_g and crystallinity values was noted by comparing the DSC results. The only exception was related to SGC30/PCL70 crystallinity, which was higher than others, while SC30/PCL70 showed a higher value of Tg but a lower value of ΔH_m.

Table 4.6: *Results of Differential Scanning Calorimetry analysis on SC/PCL and SGC/PCL blends in different ratios using equation* (4.4) *to calculate the degree of crystallinity.*

Sample	^{a} Φ_{PCL}	^{b} ΔH_m [J/g]	^{c} X_c [%]	^{d} T_g [$°C$]
PCL	100	44.75	32.08	54.35
SC10/PCL90	90	42.28	38.45	55.90
SGC10/PCL90	90	41.47	33.03	53.39
SC30/PCL70	70	34.74	35.57	56.72
SGC30/PCL70	70	45.07	46.15	53.74

[a] Φ_{PCL} *weight fraction of PCL*
[b] ΔH_m *fusion enthalpy of PCL*
[c] X_c *degree of crystallinity of PCL*
[d] T_g *glass transition temperature of PCL fraction*

Moving to analyses of superficial-physical character, contact angle measurements on films of each blend were collected in *Figure 4.30*. For pure PCL, the water droplet has a value of 75.2°, due to the hydrophobic nature of the material. When PCL is blended with SC, the contact angle became lower, and this trend is more pronounced for the higher amount of SC in the blends. In contrast, the presence of Glycerol, i.e. in SGC/PCL blends, increased the value of the contact angle ($81.93°C$ for SGC30/PCL70).

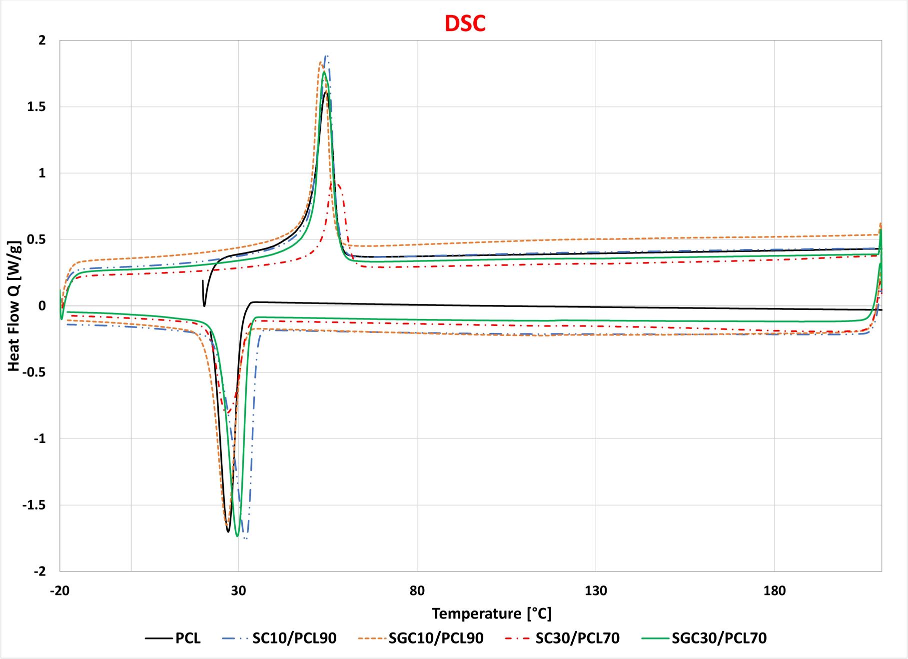

Figure 4.28: *Heat Flow curves obtained by DSC analysis on SC/PCL and SGC/PCL blends during II heating cooling cycle from* $-20°C$ *until* $210°C$*.*

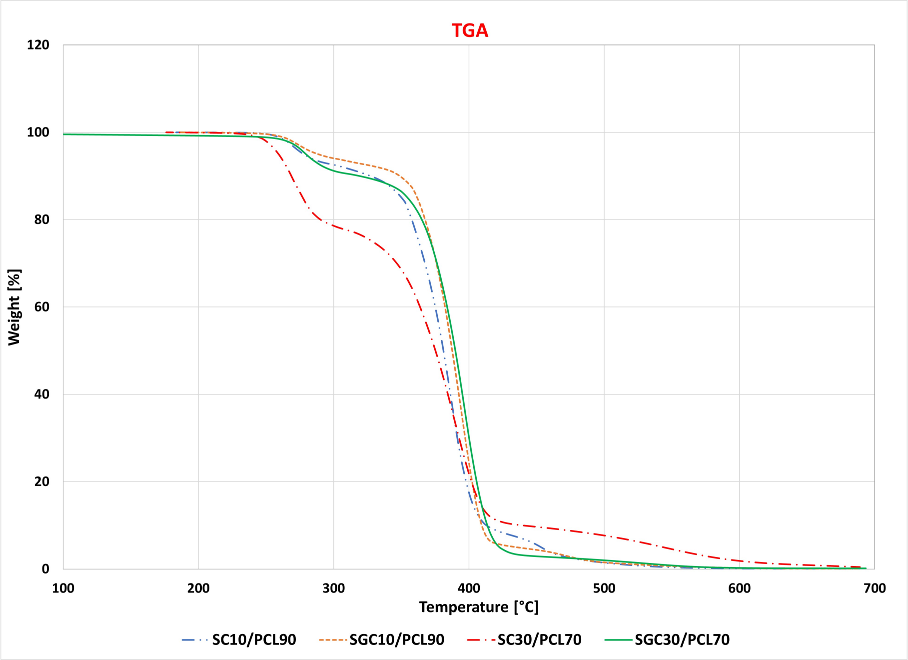

Figure 4.29: *Thermogravimetric curves of SC/PCL and SGC/PCL blends.*

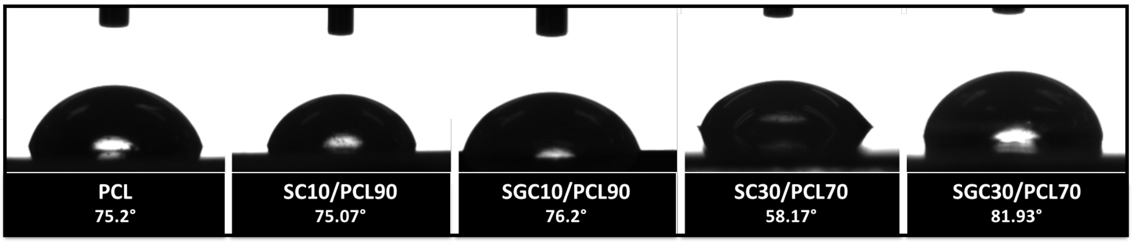

Figure 4.30: *Contact angle measurements on SC/PCL, SGC/PCL, and neat PCL film obtained by hot pressing.*

After that, cylindrical scaffolds (*Figure 4.5*) of SC/PCL and SGC/PCL blend were printed optimizing process parameters for each blend (as reported in *Table 4.3*). These scaffold were adopted for Bioevaluation tests. In detail, the EDS analysis on SC/PCL and SGC/PCL scaffolds after 7, 14, and 21 days revealed the presence of some electrolytes like Calcium (Ca), Potassium (K), Magnesium (Mg), and Phosphorus (P), but also of Chlorine (Cl) and Sodium (Na), comparing to day 0 where no significative elements were found, as shown in *Figure 4.31.*

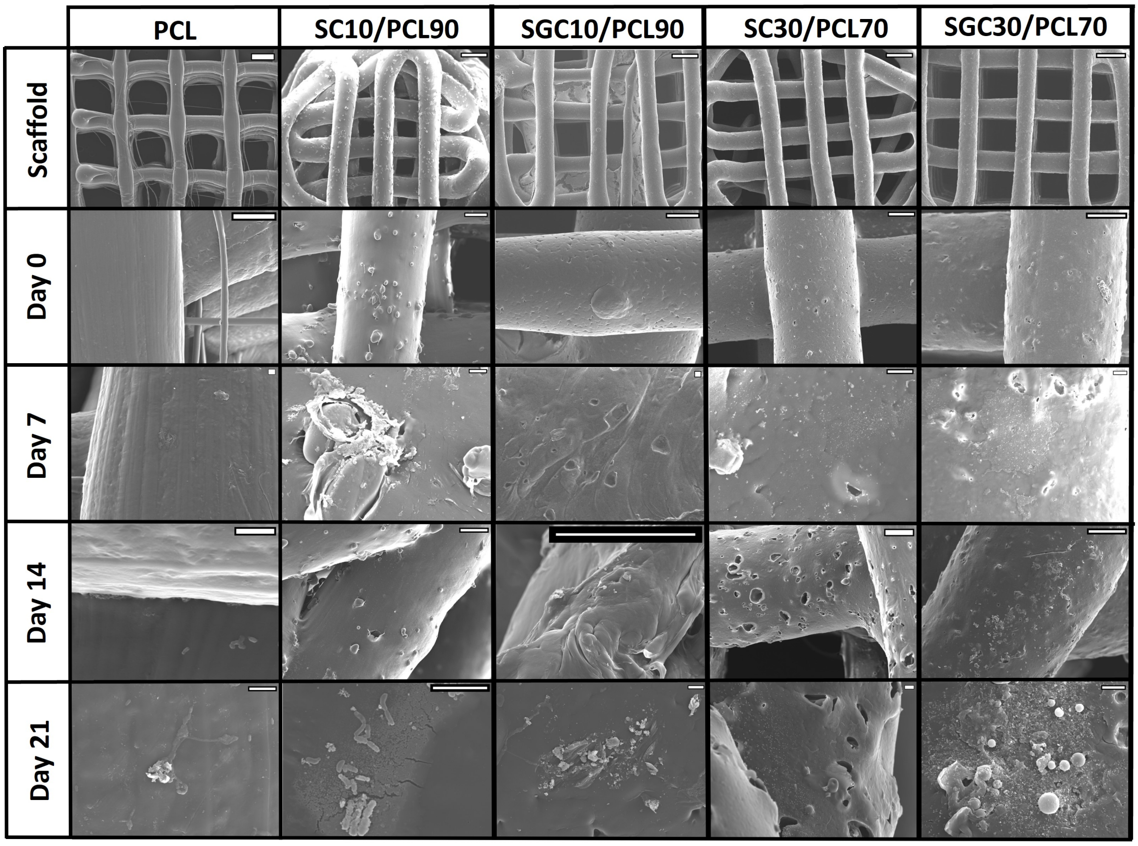

Figure 4.31: *Scanning electron microscopy analysis on SC/PCL, SGC/PCL, and PCL scaffolds after soaking for 0, 7, 14, and 21 days in simulated body fluid solution; scale bar of 500 μm for scaffold, 100 μm for day 0 and day 14, and 10 μm for day 7 and day 21.*

The results, summarized in *Table 4.7*, showed that all blends had a greater amount of electrolytes compared to pure PCL, already after 7 days. Meanwhile, comparing SGC and SC, SGC blends showed a more significant increase than SC blends after 14 and 21 days.

Table 4.7: *Energy dispersive spectroscopy results on SC/PCL, SGC/PCL, and PCL scaffolds after 0, 7, 14, and 21 days in simulated body fluid solution (SBF) soaking.*

Sample	PCL	SC10/PCL90	SGC10/PCL90	SC30/PCL70	SGC30/PCL70
Day 0	-	-	-	-	-
Day 7	Ca, Cl, Na, P	Ca, Cl, Na, P	Ca, Cl, K, Na, P	Cl, Na	Ca
Day 14	N	Ca, P	Al, Cl, N, Na, P, Ti	P	Ca, Cl, K, Mg, N, Na, P, S
Day 21	P, Si	P, Ca, Na	N, P	P, K, Ca	Ca, K, Mg, Na, P

The design of scaffolds must take into account the mechanical properties of bone tissue, such as compressive and tensile strength, hardness and elasticity. These properties may vary depending on the location and age of the bone, and may be influenced by various factors, including diet, exercise and health conditions. So, mechanical tests were also performed, obtaining stress-strain curves of each SC/PCL and SGC/PCL blend in both wet and dry conditions, as plotted in *Figure 4.32*, respectively. Hence, the compression modulus of each blend was reported for both wet and dry conditions in *Figure 4.33*.

Mechanical tests in wet and dry conditions have shown that the presence of glycerol reduced the mechanical properties of mixtures. SGC/PCL blends showed lower mechanical properties than SC/PCL with the same PCL content, in fact, SGC30/PCL70 had the lower tensile strength and deformability values compared to other blends in both wet and dry mechanical tests. On the other hand, the presence of SC increased the mechanical properties of PCL, as SC10/PCL90 showed higher tensile strength and compression modulus values than PLA/PCL blends (*Figure 4.21*). Since PCL content decreased, the material was more hydrophilic and therefore absorbed SBF, and decreased mechanical properties. However, the increase of SC or SGC content reduced the compression modulus (*Figure 4.33*). In detail, SC30/PLC70 showed higher tensile strength and deformability values, but lower compression modulus in dry conditions (8.98±2.39 MPa), as shown in *Figures 4.32a* and *4.33a*. Meanwhile, SC10/PCL90 had higher tensile strength, deformability (*Figure 4.32b*), and compression modulus in wet conditions (30.01±4.64 MPa, *Figure 4.33b*); there was a significant difference in compression modulus in both wet and dry conditions compared to other blends (p-value<0.05).

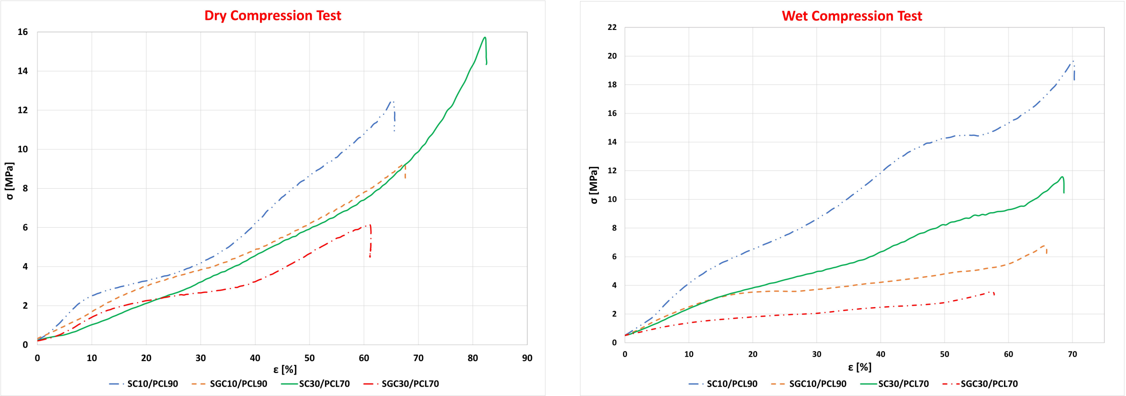

(a) **(b)**

Figure 4.32: *Stress-strain curves of each blend in both dry **(a)** and wet **(b)** conditions, considering the scaffold cylinder's apparent surface for stress values.*

Anyway, all the blends had a rubber-like behavior in both wet and dry conditions (see *Figure 4.32*). SC10/PCL90 and SGC10/PCL90 increased deformability and strength values from dry to wet conditions, while SC30/PCL70 and SGC30/PCL70 showed a reduction (*Figure 4.32*). Meanwhile, comparing compression modulus, all blends increased compression modulus from dry to wet conditions, but the only significant difference was related to SC30/PCL70 (from 8.98±2.39MPa in dry condition to

18.64±3.01MPa in wet condition, p-value<0.05). The only exception to this trend was the SGC30/PCL70 blend, which reduced its compression modulus from dry to wet condition by a non-significant factor (p-value>0.05).

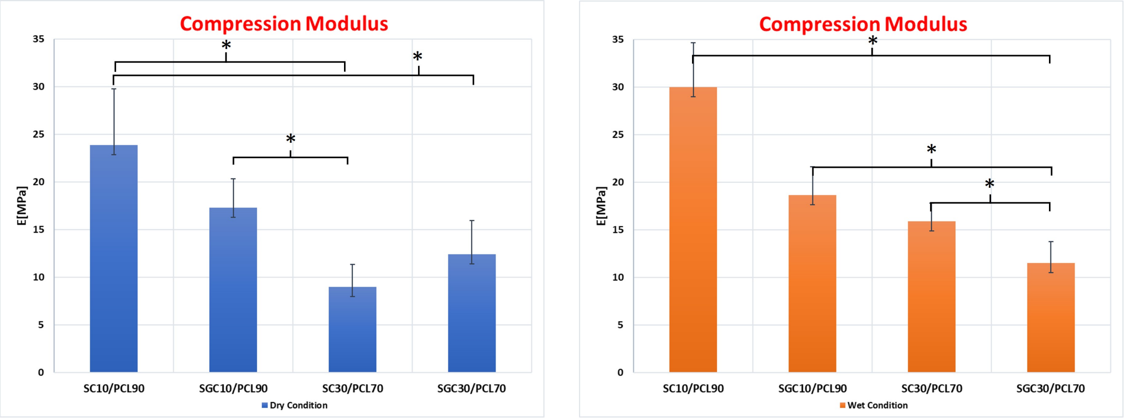

(a) **(b)**

Figure 4.33: *Compression Modulus of SC/PCL and SGC/PCL blends in both dry* ***(a)*** *and wet* ***(b)*** *conditions, considering the scaffold cylinder's apparent surface for stress values; *p-value<0.05.*

4.3 Conclusion

The focus of this research project was the design and development of a 3D scaffold for bone regeneration. According to the literature review in *Chapter 1*, polymeric blends were selected as materials, while a 3D printer as AM technique. These were the two most important steps as they influenced all the following choices in the design process such as geometry, properties and applicability of the scaffolds.

Firstly, PLA/PCL blends in different ratios have been used as standard polymeric materials due to their excellent mechanical properties, versatility, processability and low cost. Here the thermal, mechanical, and rheological properties of these blends, as well as those of the scaffolds, have been extensively analyzed. After this the internal structure of these scaffolds was focused on, particularly how the iteration between PLA and PCL can affect the structure, and subsequently the properties of the scaffolds. It has been demonstrated how it is possible to produce a biphasic circular structure with modifiable shell thickness without the use of a core-shell extruder. This structure was easily created by exploiting the phenomenon of viscous encapsulation in the 3D printing process. In detail, it has been shown how to control and modulate scaffold properties by simply changing some process parameters such as screw speed, extruder speed, needle-size, and pressure. The resulting scaffolds could find application in several biomedical areas where a structure with tunable mechanical and physicochemical properties is required. These applications include prosthetic implants, scaffolds for regenerative medicine, anti-adhesive surfaces, and controlled-release devices, where complex or expensive techniques are usually involved.

Hence, the dissolution test also provided an idea of how the internal structure will evolve when one phase degrades faster than the other, creating a porous structure. Meanwhile, the encapsulation phenomenon, according to blend crystallinity, plays an important role in the mechanical properties of the blends. Both properties are very important in the development of any kind of device, especially in the medical field as they affect, for example, stress distribution, cell adhesion and proliferation, degradation times, and even drug release time. This study shows how porosity and structure can be controlled by processing parameters as they act on the interdiffusion of components. Furthermore, if the objective is to improve the interdiffusion between two immiscible polymers, it is also possible to move the phenomenon in the opposite direction, thus decreasing the phase separation and obtaining a continuous structure rather than a composite structure.

Here, PLA and PCL, two of the most frequently and easily used polymers were used and investigated in this research work. However, the adopted method, i.e., modification of process parameters to control the phenomenon of viscous encapsulation, can be applied to all blends of immiscible polymers, shedding light on a little-studied facet of polymer blend behavior in additive manufacturing.

After that, a promising new material was developed and further investigated during thesis development. Firstly, unlike what has been done until now, a new synthesis process was implemented in order to blend Starch, Citric Acid, and Glycerol obtaining a kind of "pasta" that can be used for a 3D printing technique. In detail, the blends were prepared using a combination of two different polymer emulsion reactions: first, the mixtures of SC and SGC were made, and then they were blended with PCL in different ratios, i.e. 10/90, 30/70 and 50/50. However, 50/50 blends were difficult to process and print, so they were excluded from further investigation in this research work. In contrast, 10/90 and 30/70 showed good workability and properties.

Even though blends of Starch and PCL or Starch and Citric Acid were already used in electrospinning and salt-leaching, a 3D printed technique was adopted in this research, showing good and easy printability of the materials. Nevertheless, the thermal, physio-chemical, and mechanical characteristics of each blend were investigated in this research. It has been established that there was a significant improvement in the properties of PCL-based blends due to the presence of Starch and Citric Acid. In contrast, the presence of glycerol seemed to increase bioactivity but, at the same time, reduced mechanical properties and hydrophilic. In fact, SGC mixtures showed lower mechanical properties than SC mixtures with the same PCL content. Another interesting fact was related to the hydrophobic of the blends, showing a non-significant decrease when the SC percentage was 10%, but an impressive reduction when the SC content was 30%.

Ultimately, the association with SC should be an interesting, low-cost, and environmentally friendly material way to overcome the most important weaknesses of PCL, such as high hydrophobic and low elasticity. SC/PCL could be used in all applications where PCL is widely used, such as a biomedical field or packaging application, as its valid and competitive substitute, also involving a 3D printing technique that is the cheapest and easiest to use. However, further studies are needed before this new blend can be used for commercial applications, especially in the biomedical field, although it is known that increased hydrophilic is a key factor in cell adhesion, and consequently in regenerative medicine for bone scaffold realization.

Finally, moving from materials to scaffold structure, FE analyses on nTop were conducted on six different types of structures, namely *S:00-90°*, *S:00-45°*, *G:00-90°*, *G:00-45°*, *V_ cost*, and *V_ ramp*, using materials properties of PLA50/PCL50. This analysis demonstrated that, even if the fiber's thickness is almost the same among the designs, the distribution and shape of fibers in the scaffold, strongly influence the material's properties and behavior. Among these structures, both Voronoi and Gyroid structures showed a better distribution of stress and strain along the structures as isotropic materials, while the S-structures showed an anisotropic behavior. In addition, due to the low displacement value, although Poisson's ratio is positive, *G:00-90°* and *V_ ramp* show very similar behavior to auxetic materials, i.e. those materials that have a negative value of Poisson's ratio and contract laterally when subjected to compression. Anyway, analysis of the study demonstrated that the Voronoi lattice structure with gradient porosity yielded the lowest displacement values (i.e. 1.06 mm) and homogeneous distribution of stress and strain among all the designs. Furthermore, the Voronoi has a gradient of pores size, in opposite to the Gyroid lattice, which has a constant pore size distribute along the structure. However, it is known from the literature that a pore gradient enhances and promotes scaffold osseointegration properties. Then, this should be a consistent improvement in scaffold properties also adopting the same materials.

As previously explained, both material and structure selection play a fundamental role in biomedical engineering. In particular, in the context of regenerative medicine, it is important to use a scaffold that can support external loads and encourage cell growth for the regeneration of the surrounding tissue. So, the results also indicate that the Voronoi structure with porous gradient has the potential to be implemented into a scaffold for bone regeneration, whereby the mechanical integrity is still preserved. This result will not only provide orthopedic surgeons with justification for their design selection but could also provide new insights for future biomechanical studies.

Bibliography

[1] Chen, W., Chu, J., Wu, G., Zhang, Y. & Yang, M. Rheology control of HDPE/PP binary system forming a multilayer structure: Effects of MWD and shear rate. *Polymer Testing* 73, 60–71 **2019**.

[2] Huagui Zhang, Khalid Lamnawar, A. M. Fundamental Understanding and Modeling of Diffuse Interphase Properties and its Role in Interfacial Flow Stability of Multilayer Polymers. *Polymer Engineering & Science* 55, 771–791 **2015**.

[3] Takase, M., Kihara, S. I. & Funatsu, K. Three-dimensional viscoelastic numerical analysis of the encapsulation phenomena in coextrusion. *Rheologica Acta* 37, 624–634 **1998**.

[4] Holmes, L. T., Fávero, J. L. & Osswald, T. A. Modeling viscoelastic secondary flows in three-dimensional noncircular ducts. *Polymer Engineering and Science* vol. 52 1715–1723 **2012**.

[5] Yue, P., Zhou, C., Dooley, J. & Feng, J. J. Elastic encapsulation in bicomponent stratified flow of viscoelastic fluids. *Journal of Rheology* (N. Y. N. Y). 52, 1027–1042 **2008**.

[6] Zweben, C. COMPOSITE MATERIALS. **2015**.

[7] Qiu, J., Ahn, J., Qin, D., Thomopoulos, S. & Xia, Y. Biomimetic Scaffolds with a Mineral Gradient and Funnel-Shaped Channels for Spatially Controllable Osteogenesis. *Advanced Healthcare Materials* 11, 1–8 **2022**.

[8] Shan, S. et al. Multistable Architected Materials for Trapping Elastic Strain Energy. *Advanced Materials* 27, 4296–4301 **2015**.

[9] Rafiee, M., Granier, F. & Therriault, D. Advances in Coaxial Additive Manufacturing and Applications. *Advanced Materials Technologies*. 6, 1–25 **2021**.

[10] Lamnawar, K., Huagui Zhang & Maazouz, A. Coextrusion of Multilayer Structures ,*Encyclopedia of Polymer Science and Technology***2013**.

[11] Zhang, C. et al. Melt crystallization behavior and crystalline morphology of Polylactide/Poly(ϵ-caprolactone) blends compatibilized by lactide-caprolactone copolymer. *Polymers (Basel)*. 10, **2018**.

[12] Oliveira, C. S., Leeuwenburgh, S. & Mano, J. F. New insights into the biomimetic design and biomedical applications of bioengineered bone microenvironments.*APL Bioengineering* 5,**2021**.

[13] Castañeda-Rodríguez, S. et al. Recent advances in modified poly (lactic acid) as tissue engineering materials. *Journal of Biological Engineering* 17, 1–20 **2023**.

[14] Polo-Corrales, L., Latorre-Esteves, M. & Ramirez-Vick, J. E. Scaffold design for bone regeneration. *Journal of Nanoscience and Nanotechnology* 14, 15–56 **2014**.

[15] Martin, O. & Avérous, L. Poly(lactic acid): Plasticization and properties of biodegradable multiphase systems. *Polymer (Guildf).* 42, 6209–6219 **2001**.

[16] Williams, J. M. et al. Bone tissue engineering using polycaprolactone scaffolds fabricated via selective laser sintering.*Biomaterials* 26, 4817–4827 **2005**.

[17] Zhou, Y. et al. Polymerized Ionic Liquid for the Regulation of Phase Structure of PLA/PCL Blends. *Macromolecular Research* 30, 631–637 **2022**.

[18] Hassanajili, S., Karami-Pour, A., Oryan, A. & Talaei-Khozani, T. Preparation and characterization of PLA/PCL/HA composite scaffolds using indirect 3D printing for bone tissue engineering.*Materials Science and Engineering: C* 104, 109960 **2019**.

[19] Lim, J. I. Fabrication of 3D Self-Assembled Porous Microbead-Type Poly(l-Lactide-co-ϵ-Caprolactone) Scaffolds for Tissue Engineering. *3D Printing and Additive Manufacturing* 6, 204–209 **2019**.

[20] Salerno, A., Guarino, V., Oliviero, O., Ambrosio, L. & Domingo, C. Bio-safe processing of polylactic-co-caprolactone and polylactic acid blends to fabricate fibrous porous scaffolds for in vitro mesenchymal stem cells adhesion and proliferation.*Materials Science and Engineering: C* 63, 512–521 **2016**..

[21] Omar, E., Cary, V. & Gall, K. Structure-property relationships in 3D-printed poly (L -lactide- co - ϵ -caprolactone) degradable polymer. *Journal of the Mechanical Behavior of Biomedical Materials* 121, **2021**.

[22] Tan, Y. J. et al. Characterization, mechanical behavior and in vitro evaluation of a melt-drawn scaffold for esophageal tissue engineering. *Journal of the Mechanical Behavior of Biomedical Materials* 57, 246–259 **2016**.

[23] Sanchez Diaz, R. et al. Highly Elastic Scaffolds Produced by Melt Electrowriting of Poly(L-lactide-co-ϵ-caprolactone). *Advanced Materials Technologies* 7, 1–10 **2022**.

[24] Camarero-espinosa, S. & Moroni, L. Janus 3D printed dynamic scaffolds for nanovibration-driven bone regeneration. *Nature Communications* 1–12 doi:10.1038/s41467-021-21325-x.

[25] Cwieka K, Wysocki B, Skibinski J, Chmielewska A, Swieszkowski W. Numerical design of open-porous titanium scaffolds for Powder Bed Fusion using Laser Beam (PBF-LB). *Journal of the Mechanical Behavior of Biomedical Materials.* doi: 10.1016/j.jmbbm.2023.106359. **2024**.

[26] Schoen, Alan H. Infinite periodic minimal surfaces without self-intersections (Technical report). NASA Technical Note. NASA TN D-5541. **1970**.

[27] Caiazzo, F., Alfieri, V., Guillen, D.G. et al. Metal functionally graded gyroids: additive manufacturing, mechanical properties, and simulation. *The International Journal of Advanced Manufacturing Technology* 123, 2501–2518. https://doi.org/10.1007/s00170-022-10334-9 **2022**.

[28] Alknery, Z.; Sktani, Z.D.I.; Arab, A. Effect of Cell Geometry on the Mechanical Properties of 3D Voronoi Tessellation. *Journal of Functional Biomaterials* 13, 302. https://doi.org/10.3390/jfb13040302 **2022**.

[29] K. Rother, P. W. Hildebrand, A. Goede, B. Gruening, R. Preissner, Voronoia: analyzing packing in protein structures, *Nucleic Acids Research*, Volume 37, Pages D393–D395, https://doi.org/10.1093/nar/gkn769, **2009**.

[30] Yu, M., Du, Y., Han, Y. & Lei, B. Biomimetic Elastomeric Bioactive Siloxane-Based Hybrid Nanofibrous Scaffolds with miRNA Activation: A Joint Physico-Chemical-Biological Strategy for Promoting Bone Regeneration. *Advanced Functional Materials* 30, 1–12 **2020**.

[31] Salihu, R. et al. Citric acid: A green cross-linker of biomaterials for biomedical applications.*European Polymer Journal* 146, 110271 **2021**.

[32] Potter, E. &. The Important Role of Osteoblasts and Citrate Production in Bone Formation: "Osteoblast Citration" as a New Concept for an Old Relationship. *Bone* 23, 1–7 **2008**.

[33] Wang, M. et al. Photoluminescent and biodegradable polycitrate-polyethylene glycol-polyethyleneimine polymers as highly biocompatible and efficient vectors for bioimaging-guided siRNA and miRNA delivery. *Acta Biomaterialia* vol. 54, 69–80; **2017**.

[34] Yuzhang Du, Yumeng Xue, Peter X. Ma, Xiaofeng Chen, and B. L. Biodegradable Elastomeric and Intrinsically Photoluminescent Poly Silicon-Citrates. doi:10.1002/adhm.201500643.

[35] Du, Y. et al. Development of a Multifunctional Platform Based on Strong, Intrinsically Photoluminescent and Antimicrobial Silica-Poly(citrates)-Based Hybrid Biodegradable Elastomers for Bone Regeneration. *Advanced Functional Materials* vol. 25, 5016–5029 ;**2015**.

[36] Averous, L., Moro, L., Dole, P. & Fringant, C. Properties of thermoplastic blends: Starch-polycaprolactone. *Polymer (Guildf)*. 41, 4157–4167; **2000**.

[37] Sun, Y. et al. Preparation and properties of thermoplastic poly(caprolactone) composites containing high amount of esterified starch without plasticizer. *Carbohydrate Polymers* vol. 139, 28–34 ;**2016**.

[38] Nourmohammadi, J., Shahriarpanah, S., Asadzadehzanjani, N., Khaleghpanah, S. & Heidari, S. Biomimetic apatite layer formation on a novel citrate starch scaffold suitable for bone tissue engineering applications. Starch/Staerke 68, 1275–1281 ;**2016**.

[39] Saliu, O. D. et al. Barrier property enhancement of starch citrate bioplastic film by an ammonium-thiourea complex modification.*Journal of Saudi Chemical Society* vol. 23, 141–149, **2019**.

[40] Gunawardene, O. H. P. et al. Compatibilization of starch/synthetic biodegradable polymer blends for packaging applications: A review. *Journal of Composites Science* vol. 5, 1–33; **2021**.

[41] Sarder, R. et al. Copolymers of starch, a sustainable template for biomedical applications: A review. *Carbohydrate Polymers* vol. 278, 118973;**2022**.

[42] Ortega-Toro, R., Muñoz, A., Talens, P. & Chiralt, A. Improvement of properties of glycerol plasticized starch films by blending with a low ratio of polycaprolactone and/or polyethylene glycol.*Food Hydrocolloids* vol. 56, 9–19;**2016**.

[43] He, X. et al. A combined extrusion, retrogradation, and cross-linking strategy for preparing starch-based straws with desirable mechanical properties. *International Journal of Biological Macromolecules* vol. 227, 1089–1097 ;**2023**.

[44] Averous, L. & Boquillon, N. Biocomposites based on plasticized starch: Thermal and mechanical behaviours. *Carbohydrate Polymers* vol. 56, 111–122; **2004**.

[45] Vacková, T. et al. Impact of particle morphology on structure, crystallization kinetics, and properties of PCL composites with TiO2-based particles. *Polymer Bulletin* vol. 74, 445–464, **2017**.

[46] He, Y. et al. A 3D-Printed PLCL Scaffold Coated with Collagen Type I and Its Biocompatibility. *BioMed Research International* , **2018**.

[47] Kawamoto T, K. K. Preparation of Thin Frozen Sections from Nonfixed and Undecalcified Hard Tissues Using Kawamoto's Film Method. *Methods in Molecular Biology* vol. 2230, 259–281, **2021**.

[48] Molavi, F. K., Ghasemi, I., Messori, M. & Esfandeh, M. Design and Characterization of Novel Potentially Biodegradable Triple-Shape Memory Polymers Based on Immiscible Poly(l-lactide)/Poly(ϵ-caprolactone) Blends. *Journal of Polymers and the Environment* vol. 27, 632–642, **2019**.

[49] O'Mahony, C. et al. Determination of thermal and thermomechanical properties of biodegradable PLA blends: for additive manufacturing process. *Journal of Thermal Analysis and Calorimetry* vol. 142, 715–722 ,**2020**.

[50] Jing, F. et al. Development and characterization of corn starch films by blending with more hydrophobic compounds. *Applied Catalysis B: Environmental* vol. 206, 9–15 ;**2017**.

[51] L. Jeantet, Arnaud Regazzi, A. Taguet, Monica Francesca Pucci, A. S. Caro-Bretelle, et al.. Biopolymer blends for mechanical property gradient 3D printed parts.*Express Polymer Letters*, **2021**.

Chapter. 5

General Discussion, Conclusion and Future Perspectives

Bone regeneration is a rapidly evolving field of research that aims to develop new strategies to repair and regenerate bone tissue damaged or lost as a result of trauma or disease. In this field, the use of scaffolds has developed the most interest as they provide a three-dimensional structure for the growth of new bone tissue. The design of a scaffold for bone regeneration is a complex process that requires a thorough understanding of the biology and mechanics of bone tissue. Some key steps in the process of scaffold implementation are:

1. *Material Selection:* scaffolds are often made from biocompatible and biodegradable materials, such as natural or synthetic polymers, ceramics, or bioactive compounds.
2. *Decellularisation:* The antigenicity of heterologous bone tissue is eliminated by decellularisation techniques.
3. *3D Design:* bone tissue regeneration requires the development of a 3D porous biological scaffold model aimed at improving the attachment of new cells and allowing adequate oxygenation and capillary blood supply to transport nutrients and expel toxic substances.
4. *Physical, Thermal, Chemical, and Mechanical Characterization:* the scaffolds need to be further analyzed before in vivo or in vitro testing to assess the adequate properties for body implantation.
5. *Biological Loading:* the scaffolds can be loaded with biologically active molecules, such as growth factors, which could further enhance cell attachment and growth.
6. *In Vitro and In Vivo Testing:* before clinical use, scaffolds must be tested both in vitro and in vivo to assess their mechanical, biochemical, and biological properties.

It is important to note that scaffold design for bone regeneration is an active field of research and the techniques and materials used may vary according to specific clinical needs.

In this research work, a new biomechanics model was first elaborated to describe the mechanical behavior of porous biological tissues. This model made it possible to describe the phenomenon of fluid diffusion in porous media. In detail, the effects of material hereditariness were considered through the use of fractional differential calculus. The constitutive equation was extended to the three axes of fractional order material hereditariness to include the effect of the fluid pressure field, too. The main result of this study is the effect of overpressure caused by the beta-order variability of the constitutive equation. It has been shown that the overpressure in the tissue due to the loading condition is strongly dependent on the order of the fractional derivative of Caputo: the higher the order of β, the faster the pressure decreases. This can be a key aspect in the prediction of tissue damage that can be favored by a slow release of overpressure in the presence of repetitive loading. Indeed the phenomenon of swelling and consolidation occurs when $\beta \geq 0.5$ in the confined compression test, and for $\beta \geq 0.25$ in the fully drained test for constant pressure applied. Meanwhile, in variable pressure, this phenomenon never happened in the confined compression test. In addition, as $\beta \neq 0$, it has been shown that the overpressure reaches negative values and then returns to positive values when the value of non-dimensional time increases for constant load. In contrast, when $\beta = 1$, it behaves like a solid when the applied pressure is weak and imperceptible, so the external load did not affect pressure for variable load. In any case, the variable pressure did not affect the material response it behaved as if the applied pressure was constant. This effect is interesting since no literature evidence of an oscillating pressure field has been uncovered by the use of classical mathematical modeling to represent the material hereditariness. However, an experimental campaign is needed to report data on bone hereditariness behavior and pressure decay in confined and unconfined compression tests.

After that, we proceed with the selection of the material, using polymeric materials such as PLA, PCL, but also natural compounds such as Starch, CA, and Glycerol. For PLA/PCL blends, an interesting core-shell structure has been obtained through the use of a simple 3D printing technique. Moreover, the viscous encapsulation phenomenon, i.e. phase separation, has been further investigated here, showing how to control and modulate scaffold properties by changing process parameters such as pressure, screw speed, extrusion speed, and needle size, but also acting on polymers ratio. The resulting scaffolds could find application in several biomedical areas where a structure with tunable mechanical and physicochemical properties is required. These applications include prosthetic implants, scaffolds for regenerative medicine, anti-adhesive surfaces, and controlled-release devices, where complex or expensive techniques are usually involved. In contrast to these techniques, this research exploited a common and widely used 3D printing technique, demonstrating how it is possible to control and modulate the properties of scaffolds by simply changing some process parameters.

Hence, the dissolution test also provided an idea of how the internal structure will evolve when one phase degrades faster than the other, creating a porous structure. Meanwhile, the encapsulation phenomenon, according to blend crystallinity, plays an important role in the mechanical properties of the blends. Both properties are fondumental in the development of any device, especially in the medical field as they affect, for example, stress distribution, cell adhesion and proliferation, degradation times, and even drug release times. This study shows how porosity and structure can be controlled by process parameters as they act on the interdiffusion of components. Furthermore, suppose the objective is to improve the interdiffusion between two immiscible polymers. It is also possible to move the phenomenon in the opposite direction, thus decreasing the phase separation and obtaining a continuous structure rather than a composite structure.

In the context of the scaffold structure, both Gyroid and Voronoi structures showed an improvement in stress and strain distribution within the structure compared to classical designs, such as S-structures. But among these, particular attention should be paid to the *V_ramp*, which, thanks to the porosity gradient in the lattice, allowed a significant increase in porosity (almost 43% lighter) while maintaining the same mechanical performance. Moreover, the Voronoi has a gradient of pores size along the structure that enhances and promotes scaffold osseointegration properties. Consequently, incorporating a Voronoi structure in scaffold design could allow their long-term stability and minimize the risk of complications. However, there will always be room for improvement in further study to validate the results and data.

In addition, PLA and PCL, two of the most frequently and easily used polymers were used and investigated in this research work. However, the adopted method, i.e., modification of process parameters to control the phenomenon of viscous encapsulation, can be applied to all blends of immiscible polymers, shedding light on a little-studied facet of polymer blend behavior in additive manufacturing.

After that, a new biocompatible, biodegradable, and eco-friendly blend has been synthesized using Starch, CA, and Glycerol. Here, the possibility of creating a new blend using a simple protocol has been proven, as well as the possibility of using this blend in a very easy-to-use, inexpensive, and versatile AM technique, i.e. the 3D printer. In detail, SC and SGC blends were first made, chemically characterized, and then blended to PCL in different ratios. All blends, and scaffolds, were further analyzed by thermal, chemical, mechanical, and physical analysis. In detail, there was a significant improvement in both mechanical properties and hydrophilicity of PCL-based blends due to the presence of Starch and Citric Acid. In contrast, the presence of Glycerol seemed to increase bioactivity but, at the same time, reduced mechanical properties and hydrophilicity. Hydrophilicity plays a crucial role in TE, as enhances cell attachment and tissue integration, or modulates drug vehiculation and release. Therefore, the blend choice can be adapted to the desired properties and, consequently, to the final application of the materials.

In conclusion, the development of a scaffold for bone regeneration represents a significant step in the field of regenerative medicine. These scaffolds, designed to mimic the natural environment of bone tissue, can facilitate the growth and maturation of bone cells, thus promoting healing and regeneration. However, many challenges remain to be addressed, including the in vivo or in vitro tests that are required for future clinical applications. Of course, It is also possible to increase biocompatibility by adding biologically active molecules, modifying the 3D structure, or adopting other strategies. So, despite these challenges, progress in this field is promising and could lead to new therapies for bone diseases in the future. Then, complementary research would be appropriate as future applications to attest to the validity of the scaffolds proposed and developed in this research project.

Appendix. A

Fractional Calculus

This chapter contains definitions and properties from such topics of Analysis as functional spaces, special functions, and integral transforms useful for Fractional Calculus. *Fractional calculus* is a branch of mathematics that extends the traditional concepts of derivation and integration to non-integer orders, thus enabling the existence of differential operators and integrals of fractional order. In fractional calculus, the term "*powers*" refers to the iterative application of a linear operator to a function, that is, repeatedly composing with itself. More generally, one can look at the question of defining a linear operator for every real number in such a way that, when it takes an integer value, it coincides with the usual-fold differentiation if positive, and with the *-th* power of integration when negative. This field has found applications in a wide range of disciplines, including physics, engineering, finance, and the life sciences[1].
The idea of extending the operations of derivation and integration to fractional orders dates back to Leibniz, who in 1695 wrote in a letter to L'Hospital: *"The notion of a fractional order of derivation seems paradoxical, but we are guided by analogies"*[2]. Over the years, several mathematicians have contributed to the development of fractional calculus, including Liouville, Riemann, Grünwald, Letnikov and Caputo. Despite its long history, fractional calculus is still an active field of research, with many open questions concerning its physical interpretation and practical applications.
Some basic definitions and properties of fractional calculus, as well as special functions and transformed adopted in this research, are explained below; for further details please refer to the bibliography.

A.1 Special Functions and Transformed

In this section we present definitions of generalized functions and multidimensional Laplace transforms:

- *Euler's Gamma Function* $\Gamma(z)$ is defined by the so-called Euler integral of the second kind:
$$\Gamma(z) = \int_0^\infty t^{z-1} e^{-t} dt \quad (\Re(z) > 0) \tag{A.1}$$
where $t^{z-1} = e^{(z-1)\log(t)}$. This integral is convergent for all complex $z \in \mathbb{C}$ $(\Re(z) > 0)$ [3].It generalizes the concept of factorial $k!$ by extending the calculation to non-integer and/or complex values of k.

- $E^k_{\beta,k(\beta+1)}$ is the three parameters *Mittag-Leffler function*, defined as [4]

$$E^k_{\alpha,\beta}(z) = \frac{d^k}{dz^k} E_{\alpha,\beta}(z) \tag{A.2}$$

where $E_{\alpha,\beta}(z)$ is the two-parameters Mittag-Leffler function defined as [5, 6]:

$$E_{\alpha,\beta}(z) = \sum_{k=0}^{\infty} \frac{z^k}{\Gamma(\beta + \alpha k)} \tag{A.3}$$

with $\alpha, \beta, z \in \mathbb{C}$ and $\Re(\alpha) > 0, \Re(\beta) > 0$. When $|\beta = 1$, it is abbreviated as $E_{\alpha,1}(z) = E_\alpha(z)$, while for $\alpha = 0$, the series above equals the *Taylor expansion* of the geometric series and consequently:

$$E_{0,\beta}(z) = \frac{1}{\Gamma(\beta)} \frac{1}{1 - z} \tag{A.4}$$

In the case α and β are real and positive, the series converges for all values of the argument z, so the Mittag-Leffler function is an entire function. These functions are commonly used to find the solution to initial value problems of a class of fractional PDEs.

- *Hypergeometric function* is a special function represented by the hypergeometric series, that includes many other special functions as specific or limiting cases. It is a solution of a second-order linear ordinary differential equation (ODE). The hypergeometric function is defined for $|z| < 1$ by the power series:

$${}_pF_q \left[\begin{matrix} a_1 & a_2 & \dots & a_p \\ b_1 & b_2 & \dots & b_q \end{matrix} ; z \right] = \sum_{k=0}^{\infty} \frac{(a_1)_k (a_2)_k \dots (a_p)_k}{(b_1)_k (b_2)_k \dots (b_q)_k} \frac{z^k}{k!} \tag{A.5}$$

where $|z| < 1$; $a, b \in \mathbb{C}$ and $(a)_k$ is the *Pochhammer symbol* or rising factorial, defined for complex $z \in \mathbb{C}$ and non-negative integer $k \in \mathbb{N}_0$ by:

$$(a)_k = \frac{\Gamma(a + k)}{\Gamma(a)} = a(a + 1) \dots (a + k - 1) \ (k \in \mathbb{N}). \tag{A.6}$$

So that:

$$(a)_0 = 1 \text{ and } \Gamma(k + 1) = (1)_k = k! \ (k \in \mathbb{N}_0) \tag{A.7}$$

with (as usual) $0! = 1$.

- The *Fox-Wright Function* is useful for solving differential fractional equations. It is a generalisation of the Hypergeometric function ${}_pF_q(z)$:

$${}_p\Psi_q \left[\begin{matrix} (a_1, A_1) & (a_2, A_2) & \dots & (a_p, A_p) \\ (b_1, B_1) & (b_2, B_2) & \dots & (b_q, B_q) \end{matrix} ; z \right] = \sum_{n=0}^{\infty} \frac{\Gamma(a_1 + A_1 n) \cdots \Gamma(a_p + A_p n)}{\Gamma(b_1 + B_1 n) \cdots \Gamma(b_q + B_q n)} \frac{z^n}{n!} \tag{A.8}$$

- The *Wright Function* is the special case of the Fox–Wright function ${}_0\Psi_1$. It is useful for solving fractional differential equations. It is also closely related to the two-parameter Mittag-Leffler function and has the following expression[7]:

$$W_{\alpha,\beta}(z) = \sum_{k=0}^{\infty} \frac{z^k}{k!\,\Gamma(\alpha k + \beta)} \tag{A.9}$$

  For $\alpha = 0$ and $\beta = 1$ it reduces to:

$$W_{0,1}(z) = \sum_{k=0}^{\infty} \frac{z^k}{k!\,\Gamma(1)} = e^z \tag{A.10}$$

- The *Laplace Transform* is an integral transform that makes it possible to move from the study of a real variable (temporal in the cases considered) to the study of a complex variable. The Laplace transform $\mathcal{L}$ of a function $f(t)$ of a real variable $t \in \Re^+ = (0, +\infty)$ is defined by

$$\mathcal{L}[f(t)](s) = \hat{f}(s) = \int_0^{\infty} f(t) e^{-st} dt \tag{A.11}$$

  From the transformed function $\hat{f}(s)$ it is possible to obtain the original function $f(t)$ using the *Anti-Laplace* or *Inverse Laplace Transform*:

$$f(t) = \mathcal{L}^{-1}[\hat{f}(s)](t) = \frac{1}{2\pi j} \int_{c-j\infty}^{c+j\infty} e^{st} \hat{f}(s) ds \tag{A.12}$$

  The direct and inverse Laplace transforms are inverse to each other for "sufficiently good" functions $\hat{f}(s)$ and $f(t)$ [3]:

$$\mathcal{L}^{-1}\mathcal{L}[f(t)] = f(t) \text{ and } \mathcal{L}\mathcal{L}^{-1}[\hat{f}(s)] = \hat{f}(s) \tag{A.13}$$

A.2 Fractional Operator

Considering the classical derivation and integration operators, we observe that the derivation orders, i.e. the n-indices of the operators, are natural numbers ($n \in \mathbb{N}$). In detail, the fractional operator extends the order of derivation and/or integration to non-integer numbers $\beta \in \Re$, while for $\beta = n$ the classical derivative or integral is recollected.

- The *Riemann-Liouville left-sided Integral* is defined by:

$$\left({}_aI_t^{\beta} f\right)(t) = \frac{1}{\Gamma(\beta)} \int_a^t f(\tau) (t - \tau)^{\beta - 1} d\tau \tag{A.14}$$

  with $n - 1 < \beta < n$ and $\Re(\beta) > 0$. It is the integral left-sided because $t > a$, meanwhile for $t < a$ the integral right-sided is obtained:

$$\left({}_tI_a^{\beta} f\right)(t) = \frac{1}{\Gamma(\beta)} \int_t^a f(\tau) (t - \tau)^{\beta - 1} d\tau \tag{A.15}$$

To obtain the Riemann-Liouville Fractional Derivative, it suffices to consider that the derivative of order n can be considered as the derivative of order $n+m$ of the m^{th} primitive of the function, then the *Riemann-Liouville left-sided Fractional Derivative* is:

$$\left({}_aD_t^\beta f\right)(t) = \frac{d^n}{dt^n}\left({}_aI_t^{1-\beta} f\right)(t) = \frac{1}{\Gamma(n-\beta)}\left(\frac{d}{dt}\right)^n \int_a^t \frac{f(\tau)}{(t-\tau)^{\beta-n+1}} d\tau \tag{A.16}$$

with $n-1<\beta<n$ and $\Re(\beta)>0$[8, 9]. The Riemann-Liouville fractional derivative operator is the left-inverse to fractional integral, so the following property is valid:

$$\left({}_aD_t^\beta\, {}_aI_t^\beta f\right)(t) = f(t) \tag{A.17}$$

But it is not right-inverse, in fact:

$$\left({}_aI_t^\beta\, {}_aD_t^\beta f\right)(t) = f(t) - \sum_{k=1}^{m} \frac{t^{\beta-k}}{\Gamma(\beta-k+1)}\left({}_aD_t^{\beta-k} f\right)(t) \tag{A.18}$$

for $m \in \mathbb{Z}^+, m-1<\beta<m$.
Taking into account the properties of the Laplace Transform $\mathcal{L}$, setting the lower limit of the fractional derivative as $a=0$ and the order of derivation $\Re(\beta)>0$, the fractional derivative transform of Riemann- Liouville is:

$$\mathcal{L}\left[{}_aD_t^\beta f(t)\right] = s^\beta \hat{f}(s) - \sum_{r=0}^{n-1} s^r \left[{}_0D_t^{\beta-r-1} f(t)\right]_{t=0} \tag{A.19}$$

with $n-1<\beta<n$[10].

- *Caputo Fractional Derivative* is expressed as:

$$\left({}_0^CD_t^\beta f\right)(t) = \frac{1}{\Gamma(n-\beta)} \int_a^t \frac{f^{(n)}(\tau)}{(t-\tau)^{\beta-n+1}} d\tau \tag{A.20}$$

with $n-1<\beta<n$ and $\Re(\beta)>0$. Also for Caputo derivative is valid:

$$\left({}_a^CD_t^\beta\, {}_aI_t^\beta f\right)(t) = f(t) \tag{A.21}$$

and:

$$\left({}_aI_t^\beta\, {}_a^CD_t^\beta f\right)(t) = f(t) - \sum_{k=0}^{m-1} \frac{t^k}{\Gamma(k+1)} f^{(k)}(t) \tag{A.22}$$

with $m \in \mathbb{Z}^+, m-1<\beta<m$ [11, 12]. Between the Caputo and Reimann-Liouville fractional derivatives there is a formula that binds them:

$$\left({}_a^CD_t^\beta f\right)(t) = \left({}_aD_t^\beta f\right)(t) - \sum_{k=}^{m-1} \frac{t^{k-\beta}}{\Gamma(1+k-\beta)} f^{(k)}(t) \tag{A.23}$$

Bibliography

[1] Zhmakin, A. I. A Compact Introduction to Fractional Calculus. **2022**

[2] Mainardi, F. Fractional calculus: Theory and applications. *Mathematics* 6, **2018**.

[3] Srivastava H.M., Trujillo J.J., et al. , “Theory and Applications of Fractional Differential Equations", *North-Holland Mathematics Studies*, vol. 204, **2006**.

[4] Gorenflo, R., Kilbas, A. A., Mainardi, F. & Rogosin, S. Mittag-Leffler functions, related topics and applications: Second Edition.*Springer Monographs in Mathematics* , **2020**.

[5] Haubold H. J., Mathai A. M., Saxena R. K. "Mittag-leffler functions and their applications". *J. Appl. Math*, 1–51, **2011**.

[6] Gupta I. Sen Debnath, L. "Some properties of the Mittag-Leffler functions". *Integral Transforms and Special Function.* 18, 329–336, **2007**.

[7] Wright, E. M. The Asymptotic Expansion of the Generalized Hypergeometric Function. *Proceedings of the London Mathematical Society*, s2-46, 389–408 **1940**.

[8] A. Carpinteri, F. M. Fractals and Fractional Calculus in Continuum Mechanics. *Springer-Verlag Wien GmbH*, **1997**. doi:10.1007/978-3-7091-2664-6.

[9] Gorenflo, Rudolf, F. M. FRACTIONAL CALCULUS : Integral and Differential Equations of Fractional Order Rudolf. *Journal of Chemical Information and Modeling*, vol. 01, **2013**.

[10] Di Paola M, Pinnola FP. "Calcolo frazionario & viscoelasticità". Published online **2011**.

[11] Podlubny, I. Fractional Differential Equations. **1999**.

[12] Pinsky Mark A., “Partial Differential Equations and Boundary-Value Problems with Applications:Third Edition",*Pure and Applied Undergraduate Texts*, Vol. 15; 526, **1998**.